The Dissertation Committee for Patrick Thomas Wittick
certifies that this is the approved version of the following dissertation:

Hybrid Discrete-Element Gravity Models for Small Celestial Bodies

Committee:

Ryan P. Russell, Supervisor

Srinivas Bettadpur

Moriba Jah

Brandon Jones

Gregory Lantoine

Hybrid Discrete-Element Gravity Models for Small Celestial Bodies

by

Patrick Thomas Wittick

DISSERTATION

Presented to the Faculty of the Graduate School of
The University of Texas at Austin
in Partial Fulfillment
of the Requirements
for the Degree of

DOCTOR OF PHILOSOPHY

THE UNIVERSITY OF TEXAS AT AUSTIN
August 2020

For my wife Amelia, my parents Thomas and Jacqueline, and my sister Jennifer.

Also dedicated to my grandfather, Dr. James J. Wittick, whose attainment of a PhD under far more stressful circumstances has served as a constant inspiration.

Acknowledgments

First, I would like to thank the members of my committee for their support, feedback, and instruction at various points in my graduate career. Special thanks go to my advisor, Dr. Ryan Russell, for convincing me to choose the University of Texas and for his constant support and advice over the past five years. His flexibility and engagement were crucial in maintaining a work arrangement that fit with my personal life and allowed me to obtain my degree at the University of Texas. I also wish to thank Kenny Getzandanner at NASA Goddard Space Flight Center (GSFC) for serving as my research collaborator and internship supervisor. His roles on the Flight Dynamics teams for both OSIRIS-REx and CAESAR helped to inform and improve this work.

This work was funded by NASA through a NASA Space Technology Research Fellowship (NSTRF). The NSTRF program office has my thanks, as the fellowship provided not only generous funding, but also the opportunity to spend several valuable internships at both Goddard Space Flight Center and the Jet Propulsion Laboratory (JPL). Special thanks go to my internship supervisors, Kenny Getzandanner (GSFC) and Dr. Gregory Lantoine (JPL) for their advice and sponsorship. Many others, including Dr. Yu Takahashi (JPL) and Dr. Erwan Mazarico (GSFC), provided input and support for this work, and they also deserve my gratitude.

I would also like to thank the UT Graduate School and the Department of Aerospace Engineering and Engineering Mechanics for their financial support during my first year of graduate school and over several following years.

Hybrid Discrete-Element Gravity Models for Small Celestial Bodies

by

Patrick Thomas Wittick, Ph.D.
The University of Texas at Austin, 2020

Supervisor: Ryan P. Russell

The status of small celestial bodies as time capsules from the early age of the solar system has made them targets of increasing numbers of scientific exploration missions, while their value as ubiquitous sources of precious metals and volatiles has drawn the attention of extraterrestrial mining interests. In-situ spacecraft operations have been and are likely to continue being conducted in the dynamically complex near-surface environment at these bodies. The near-surface gravity field presents a particular modeling challenge for small bodies, as the gravity field is generally irregular and not well-modeled by two-body dynamics or common analytical perturbation methods. Hence, mission design efforts typically take an efficiency penalty to achieve near-field accuracy, or an accuracy penalty in the name of rapid design.

A number of gravity field modeling techniques have been developed and applied at small bodies. Their drawbacks vary from field degradation near the surface to divergence in large portions of the relevant spatial domain to long computation times ill-suited to rapid trajectory design. This work aims to blend the desirable characteristics of several conventional small body gravity modeling approaches while mitigating their drawbacks in order to generate fast, accurate, and globally valid gravity field representations. Resulting gravity models are constructed in a modified discrete-element framework and take advantage of the best-available gravity field information at each mission stage.

First, discrete-element gravity models with a hybrid force evaluation are developed for use prior to the collection of in-situ observations. A flexible shape model packing algorithm generates a layered array of polydisperse, spherical discrete elements shaped by the primitive body morphology. The elements are assigned either point-mass or low-degree and -order spherical harmonics gravity signatures, the superposition of which yields a fast, global net gravitational force model. The hybrid models are dubbed Multi-Layer Mascon and Exterior Spherical Harmonics, or MultiMESH gravity models. A sequence of linear filters fits the modeled surface potential to that of a homogeneous polyhedron (generally considered the most accurate gravity field model absent in-situ observations). For optimal packing configurations, MultiMESH models are shown to provide order-of-magnitude computational speedups compared to homogeneous polyhedra of equivalent accuracy in an identical exterior region of validity. Efficiency gains are demonstrated for the small bodies 433 Eros, 216 Kleopatra, 25143 Itokawa, and Comet 67P/Churyumov-Gerasimenko.

Once in-situ observations are available, information about the primitive body gravity field is typically expressed in the form of a spherical harmonic expansion. The second major contribution of this work is the development of fast mascon proxy models for low-altitude gravity representations that are statistically consistent with reference spherical harmonic gravity fields. Solution methods involve the division of mascon models into regions of constant density and the estimation of the densities of those regions by matching the global Stokes coefficients of the heterogeneous mascon distribution to the Stokes coefficients of the reference field. The algorithm is demonstrated to recover heterogeneous mascon models with high accuracy given an accurate mascon configuration. Several mascon proxy solutions are built for Comet 67P/C-G using a spherical harmonics gravity solution from orbit determination as truth. The models are statistically consistent with the reference field and offer speed advantages over similar approaches that utilize regional subdivisions of polyhedra.

Table of Contents

List of Tables

List of Figures

Chapter 1

Introduction

1.1 Motivation and Problem Definition

Small celestial bodies like asteroids, comets, and other minor planets are the most numerous denizens of our stellar neighborhood and represent a deep well of both scientific discovery and engineering challenges. Increasingly, as in the case of Hayabusa[1], OSIRIS-REx[18], and Rosetta[29], spacecraft are required to conduct science operations in the vicinity of small body surfaces via surface landers or touch-and-go sample collections. Such in-situ science provides enormous benefit to the scientific community, yet it also places multi-million or -billion dollar spacecraft in the most dangerous and dynamically challenging locations in the small body environment. In order to mitigate the inherent risk of these operations, mission planners need both the best possible information about the near-surface dynamical environment *and* the ability to rapidly consider, plan, and re-plan trajectory options in the face of unforeseen conditions.

Knowledge of the small body gravity field evolves over the course of its exploration. Initial gravity field models are reliant on remotely-collected information such as radar images, light curves, and albedo measurements.

Such measurements permit the estimation of a shape model and bulk density value, which form the basis for the homogeneous polyhedral gravity field [79]. In the absence of in-situ mission data, the polyhedral field is frequently employed in studies of the primitive body near-surface dynamical environment [42, 64, 63]. Because the polyhedral gravity field is representative of the best-available shape and mass information, and it provides continous, smooth, and exact field evaluations at all points above the body surface, it is frequently considered the most accurate gravity field model prior to spacecraft orbital insertion. However, as will be discussed later in this chapter and in Chapter 2, the polyhedral representation can be computationally inefficient and therefore ill-suited to rapid mission design. Additionally, polyhedral evaluation times only grow as the shape model is refined on approach.

To facilitate more extensive explorations of the small body orbital environment, simplified (i.e. faster) gravity field models are sometimes employed [35, 21, 36]. Such models tend to sacrifice fidelity in the name of efficiency, however. As a spacecraft explores a small body, it tends to proceed through science orbits of progressively lower altitude, estimating spherical harmonic gravity coefficients of progressively higher degree and order using radiometric data, optical measurements, or other data. For small bodies, estimated spherical harmonic fields tend to truncate at relatively low degree and order[40], making them efficient to evaluate. However, due to series divergence in the spherical harmonic representation, these models are ill-suited for near-surface use.

This research aims to address several drawbacks of commonly used small body gravity modeling approaches over the various stages of the science mission lifecycle. Namely, this work: 1) develops small body gravity representations for use in the pre-arrival phase that accelerate the field computation relative to the polyhedral model, yet retain much of the polyhedral field's accuracy and physical domain validity, and; 2) introduces a method to estimate fast mascon proxy models from a reference spherical harmonics gravity field representation, thereby providing statistically consistent gravity models for all points exterior to the body in the post-arrival phase. Both objectives are achieved by modifying conventional discrete-element mass modeling approaches with the intention of accelerating the mission design process at all phases of small body exploration.

1.2 Literature Review

First, a review of the relevant research in small body gravity and mass distribution modeling and estimation is given. Common gravity field representations including polyhedron-based, discrete-element, series approximation, and nodal interpolation models are discussed. Literature considering the problem of gravity inversion, or the estimation of mass distributions from gravity information, is also reviewed.

1.2.1 Modeling Small Body Gravity Fields

A variety of gravity field modeling techniques have been applied at small celestial bodies after being developed for local or global gravity representations at planetary bodies. The small masses and irregular shapes typical of asteroids and comets often necessitate some modification of the planetary techniques; otherwise the domain of convergence may be limited. The most common gravity modeling techniques for small bodies are reviewed in this subsection, along with their relative advantages and limitations.

1.2.1.1 Polyhedron-Based Methods

The calculation of the gravitational potential of faceted bodies has been a subject of study in the geophysical literature for decades. Faceted bodies are of interest because they can represent real mass distributions with heightened complexity and realism relative to point masses, yet remain tractable due to the linearity of their boundaries. Closed-form expressions for simplified shapes such as rectangular prisms [43], rectangular parallelpipeds [4], and polygonal prisms with inclined faces [66] have been presented over the years. The gravitational field of more complex polyhedral shapes has also been well-studied [5, 45, 76, 55, 80].

When modeling the gravity field of an irregularly-shaped small body, the polyhedral method of Werner and Scheeres [79] provides a particularly convenient and robust solution. Under a constant density assumption, the potential evaluation can be converted from a volume integral to a surface integral over the facets and edges of a finite-element (FEM) polyhedral shape model. The result is an exact solution for the potential of a homogeneous, non-intersecting polyhedron. However, this method can be computationally inefficient due to the need to perform repeated evaluations of expensive functions like arctangents and logarithms over the whole body surface.

Modifications to the Werner-Scheeres polyhedral model have been proposed in the intervening years for the purposes of accelerating field computations. McMahon [38] proposes a multi-resolution composite polyhedral solution to reduce computation times while retaining the accuracy of higher-resolution global models. Pearl and Hitt [53] present a quadrature-based approximation of the base polyhedron in order to accelerate the field computation, demonstrating accurate potential evaluations down to the surface and accurate acceleration evaluations at altitudes greater than the mesh resolution.

The Werner-Scheeres polyhedral model has also been adapted for internal density distribution estimation. Scheeres, et al. [62] represent density heterogeneities by dividing polyhedral shape models into simplicies and by further dividing the simplicies radially. Takahashi and Scheeres [69] advanced this approach by adopting a morphology-driven polyhedral discretization scheme and a more general block-division algorithm. While the gravity field calculation for these approaches requires no convexity in the body shape, the regional division schemes rely to some extent on the division of simplices emanating from the origin and terminating at the shape model facets. For nonconvex shapes, these simplices may overlap or include space external to the body, and one suspects the division scheme may need to be adapted for such cases.

1.2.1.2 Representation by Series Expansion

Like polyhedral shape models, spherical harmonics [30] are useful in the representation of both the topography and the gravity field of a small body; in fact, the gravitational spherical harmonics may be directly derived from the topographic harmonics [3] for an homogeneous body. A similar calculation may be performed to find the spherical harmonic coefficients for a constant density polyhedron [78]. Recent work has attempted to quantify the uncertainty in inertia parameters and spherical harmonic coefficients for small bodies represented by a polyhedral shape model of uncertain size and shape [7, 47, 8]. The zeroth, first, and second degree harmonic coefficients are conveniently related to the mass and inertia properties of the body represented, enabling the translation of coefficients into information on the mass distribution[61]. However, the classical application of this method suffers from two major weaknesses in the context of small celestial bodies: 1) the potential field diverges inside the Brillouin sphere (i. e. the circumscribing radius) of the body, and 2) the series representation of the potential may require an excessive number of terms for highly non-spherical bodies.

Recently, work by Takahashi and Scheeres [68] and Casotto and Casotto [12] has sought to address the former problem by introducing and advancing *interior* spherical harmonics fields. These fields, in contrast to *exterior* spherical harmonics fields, are located outside a shape model and have a region of convergence that lies completely within the interior field's reference sphere. These interior harmonics expansions are quite useful when estimating a localized field near the body surface, but, in practice, many of these expansions must be generated to represent the field over the entire body surface simultaneously. Series expansions in spherical Bessel functions have also been investigated for near-surface gravity field representations [23, 70]. Interior Bessel gravity representations form a solution of Poisson's equation in the form of Helmholz's equation and directly complement the solution space of the (conventional) exterior spherical harmonics representation. Another approach uses ellipsoidal harmonics, which have a region of convergence that lies exterior to a reference ellipsoid [57]. Since the shapes of many small bodies are more closely approximated by ellipsoids than spheres, ellipsoidal harmonics offers convergence advantages over spherical harmonics expansions in the small body domain.

The forward mapping of the spherical harmonic gravity field from a given polyhedral density model has already been discussed; however, the mapping is not one-to-one. Some work (already mentioned above) has explored the use of spherical harmonic coefficients as measurements in a batch least squares fit to estimate heterogeneous polyhedral density maps [62, 69]. While each of these works obtains unique solutions for particular density maps, it is not possible in general to recover a particular density distribution (meaning both values and their spatial mapping) from a particular gravity field. The ill-conditioning of this problem features prominently in the current work, and will be discussed in more detail shortly.

1.2.1.3 Discrete-Mass Models

Mascon models have heritage as a means of representing localized gravitational anomalies. In the 1970s, mascon models gained popularity as an alternative to spherical harmonics when estimating the gravity fields of the Earth and the Moon, especially when attempting gravity field inversion with sparse satellite orbit determination data [31, 32, 39, 41, 34]. Typically mascons were applied as a single surface layer overlaying an oblate spheroid and used to represent small deviations from that underlying model. This technique has continued more recently at Ganymede using Galileo flyby data [46]. At the Earth, surface mascon models have been utilized with the GRACE mission as a means of representing equivalent water height over the planet's surface at high resolution [77, 60]. Other work has demonstrated that, when measurements of a high-degree and -order spherical harmonics field are used as observations in a least-squares gravity field inversion problem, the Earth's gravity field may be efficiently represented in high fidelity by an oblate spheroid and a buried layer of mascons [58].

Mascon models are particularly suited to small bodies due to their ability to model irregular shapes and density distributions at arbitrary resolution [49]. While the mascon approach provides a good approximation of the far-field environment, the discretized mass distribution results in degraded potential evaluations near the mascon elements. The recent work by Tardivel

[72], where several different mascon packing schemes were evaluated for their accuracy, demonstrated the drawbacks inherent in a constant density mascon model for a small body. [50, 52, 51] have employed interior and surface meshes for use in an alternative mascon method, while [24] leveraged multiple interior spherical harmonics expansions to model density variations within an asteroid.

1.2.1.4 Interpolation-Based Models

Gravity field interpolation schemes offer a particularly fast means of obtaining field evaluations, but that speed often comes at the cost of long upfront calculations and large memory requirements. In addition to memory and speed, interpolation methods often trade smoothness, continuity, and exactness (i.e. the force model may not be a solution to Laplace's equation). Interpolation of the gravity field between nodes was pioneered by Junkins [28] and Engels and Junkins [16] using the Earth's spheroidal geometry as a basis for the node positioning. In the former work, the Earth's spherical harmonics field out to degree 23 was substituted with a finite-element approximation out to 1.2 earth radii. Significant computational efficiency gains were observed relative to the reference spherical harmonic model. More recently, interpolation schemes have been investigated in the small body environment [14]. In the small body case, the nodal geometry is determined through the use of octree data structures, permitting an adaptive structure that can drive errors to within user thresholds. Other interpolation-based models have been introduced in recent years, namely the cubed-sphere[26], MRQSphere[25], and

Fetch[2] models. The nodal geometry for these models is generally sphere-based, making them suitable primarily for accelerated field computations outside the circumscribing sphere of the primary.

Interpolation-based gravity models for small bodies are not explored in the current work for several reasons. Research for this dissertation is directed toward the development of fast gravity models that support rapid mission design efforts, including efficient trajectory optimization. Optimizers frequently utilize gradient-based solvers that benefit from a field representation that provides analytic partials of the potential, which is not the case for many interpolation-based schemes including that of Colombi, et al. [14]. Interpolation-based models also commonly have large memory requirements; although modern onboard computers have sufficient memory space, minimization of the model memory footprint is still desirable from a systems engineering perspective when considering deployment onboard a spacecraft. Finally, gravity models that tie the mass distribution to the gravity representation more closely represent the physical system at play and may be of broader interest in both the astrodynamics and geoscience communities.

1.2.2 Gravity Inversion

Gravity inversion is the process of estimating the magnitudes and/or locations of one or many density anomalies within a body using measurements of the body's gravity field. Therefore, the gravity inversion topic pairs frequently with mascon representations in geodetic literature (though other mass representations are valid problem targets). The process may be used to solve for mass distributions on a global scale (typical of space-based geodesy problems, see [77, 60]) or a more local scale (typical of natural resource exploration and studies of subsurface processes, see [10, 19, 9, 59]). It is important to note that the gravity inversion problem is known to be ill-conditioned due to poor observability, particularly when attempting to estimate the mass parameters of a dense mascon distribution [13, 6]. The ill conditioning is physical in theory, but for practical gravity inversion problems involving discrete-element arrays, the ill-conditioning instead stems from the inability to take measurements of the field in the interior of the body.

Since much of the mascon-focused work discussed above considers only two-dimensional mass distributions [31, 32, 39, 41, 34, 58], it is useful in the present work context to examine geophysical literature dealing with the estimation of three-dimensional distributions. Generally, researchers impose one or more constraints on the ill-posed inversion problem in order to obtain a solution. Frequently, mass anomalies are constrained spatially to exist within a confined subsurface region or a regular polyhedral shape [9]. Smoothness and continuity constraints may also be placed on a mass distribution to obtain a solution which is more likely to be physical [59, 10]. The final solution of the inversion problem may also be biased toward physical reality by initializing the estimation process with an *a priori* state based on existing geological models [10].

1.3 Dissertation Outline

This dissertation consists of three main chapters covering the main contributions of the research, with a preceding chapter containing supporting material. The supporting chapter (Chapter 2) reviews the main small body gravity modeling approaches referenced and leveraged in the primary chapters.

The methods of construction and evaluation of Multi-layer Mascon and Exterior Spherical Harmonics (MultiMESH) small body gravity models are detailed in Chapter 3. Modifications to shape model scaling and discrete element packing methods that underpin the models are discussed. A two-step batch least-squares filtering method is presented and considered against alternative approaches for the estimation of MultiMESH mass distributions. A set of test models is constructed for the well-studied asteroid 433 Eros. The model performance is quantified in a multidimensional space; models that offer ideal performance trade-offs are identified and discussed in more detail. An analysis of typical MultiMESH mass distributions is also given.

In Chapter 4, the MultiMESH small body gravity modeling approach is applied to several additional small bodies of interest: asteroids 216 Kleopatra and 25143 Itokawa, and Comet 67P/Churyumov-Gerasimenko. Further modifications to shape model scaling are made to support the construction of MultiMESH models for extremely nonconvex bodies. A systemic approach toward the identification of optimally-performing gravity models is taken: the discrete-element model design space is parametrized and a global search is conducted for each body of interest. The performance advantages of high-performing MultiMESH models identified in Chapter 3 for 433 Eros are confirmed to extend to other small bodies.

While Chapters 3 and 4 consider the polyhedral gravity model as a reference in developing MultiMESH models for the pre-arrival phase, Chapter 5 considers the post-arrival or repeat mission problem, in which knowledge of the body gravity field is represented by a spherical harmonic representation estimated during orbit determination. An alternate method of solution is presented, utilizing the gravity coefficients as measurements in a batch estimation instead of the potential. Several methods to divide mascon models into morphology-driven or grid-based regions of constant density are detailed to reduce the dimensionality of the estimation problem. A hard constraint on the total model mass and an optional *a priori* state are added to the solution method to improve realism in the estimated density distributions.

Finally, in Chapter 6, the main contributions and implications of this work are reviewed. Potential directions of future work are discussed. The appendices contain some further detail and supplemental detailed model performance data, as well as a list of conference proceedings and publications resulting from this work.

1.4 Summary of Contributions

This research revisits discrete-element mass models for small celestial bodies with the aim of creating fast, accurate proxy models for a variety of use cases. The included work makes several contributions to the field of gravity field modeling at small celestial bodies.

- A flexible discrete-element shape model packing algorithm is presented that is robust to nonconvexity in the body shape. Given a set of packing parameters, the algorithm can generate model configurations ranging from conventional uniform mascon arrays to multilayered, polydisperse discrete-element configurations in both volumetric and scaled shape model surface arrangements.

- A hybrid small body gravitational force model is introduced in which subsurface discrete elements are assigned point-mass and low-degree and -order spherical harmonic gravity signatures in the same models. The use of spherical harmonics for large element gravity contributions is memory-efficient and retains the global validity of the external net field representation. Several filtering techniques to match the hybrid field potential to the polyhedral potential are surveyed. Techniques include single nonlinear batch solvers, a interative sequence of linear solvers, optional inclusion of a priori solutions, and constraints on the model mass. A sequence of batch linear filters with an optional prior is shown to best minimize the potential residuals.

- MultiMESH models along the performance Pareto front are shown to offer computational speedups of up to an order of magnitude when compared with reduced-resolution polyhedral models of equivalent accuracy.

- A regional small body density distribution estimation algorithm is extended for mascon models using spherical harmonic coefficients as measurements. The algorithm recovers heterogeneous mascon models with high accuracy given a suitable model configuration.
- The application of a hard constraint on total model mass and a properly weighted homogeneous prior are shown to facilitate the estimation of regional mascon models with all positive density distributions. A test case for Comet 67P/C-G using the Rosetta OD gravity coefficients as measurements results in the estimation of regional mascon models that 1) are statistically consistent with the OD solution, and 2) have density distributions with all positive densities.

Supporting these contributions is a custom code package, written in Fortran 90, to build, solve, and evaluate the performance of MultiMESH and regional mascon models using polyhedral and spherical harmonics reference models. The code is modular and multifunctional. Given a polyhedral shape model, it packs the interior volume according to a large set of packing parameters that may be either user-set or automatically generated. Gravity signatures may then be assigned according to several different schemes. Estimation of the mass distribution may be performed either by potential-fitting or coefficient-fitting filters, and the model performance can then be evaluated in terms of acceleration accuracy, memory footprint, and execution time across a variety of surfaces and point distributions. Outer loops around these various functions may also be enabled to build a variety of models or search for optimal configurations. Several gravity models and a suitable Fortran 90 execution code are also made publicly available.

Chapter 2

Small Body Gravity Models

As discussed in Chapter 1, there are a variety of ways to model the gravity field of small celestial bodies. The need for gravity models to account for significant perturbations away from Keplerian orbits due to primitive body shape irregularity forces important tradeoffs between accuracy, efficiency, and mathematical exactness. This chapter provides an overview of the gravity modeling methods relevant to the research presented in this document. We are primarily concerned with models that result from the volume integral over the body of the potential of a differential mass element; hence, methods based on interpolation of the field between nodes are not discussed in this chapter. Focus will instead be placed on modeling approaches that, through various means, relate the primitive body mass distribution to the gravity field and are most commonly applied in astrodynamics and geophysical modeling applications. Specifically, point-mass models (singular and collective), spherical harmonics, and the polyhedral surface integral will be discussed.

2.1 Gravity Field of a Nonuniform Body

Before proceeding to the operative small body gravity models, we first define expressions for the gravity field of a general body of mass. The expressions account for finite dimensions, irregular shape, and potentially nonuniform density in the mass distribution, all of which are features of real small celestial bodies. Newton's Law of Universal Gravitation gives the force of attraction between two mass singularities M and m as

$$\mathbf{F} = \frac{GMm}{|\mathbf{r}_1 - \mathbf{r}_2|^2} \tag{2.1}$$

where $\mathbf{r}_1$ and $\mathbf{r}_2$ are the positions of M and m, respectively, and G is the universal gravitational constant. Applying Newton's second law, the acceleration of m due to the primary M can be calculated:

$$\mathbf{a} = \frac{GM}{|\mathbf{r}_1 - \mathbf{r}_2|^2} \tag{2.2}$$

This acceleration is the gradient of a scalar potential U. After simplifying by setting $r = |\mathbf{r}_1 - \mathbf{r}_2|$ and $\mu = GM$, we obtain for that potential

$$U = \frac{\mu}{r} \tag{2.3}$$

It can be shown that the potential is a solution to Laplace's equation,

$$\nabla^2 U = 0. \tag{2.4}$$

The potential can also be found for a differential mass element $dM = \rho\, dV$ using Eq. 2.3:

$$dU = G\frac{\rho\, dV}{r} \tag{2.5}$$

where ρ is the density of the mass element and dV is its differential volume in arbitrary coordinates. To evaluate the potential of an extended body with nonuniform density at a field point at position $\mathbf{r}$, integrate over the body:

$$U(\mathbf{r}) = G\iiint_{\mathcal{B}} \frac{\rho(\mathbf{R})}{|\mathbf{r} - \mathbf{R}|} dV \tag{2.6}$$

where $\mathbf{R}$ is the position of differential mass element $\rho(\mathbf{R})\, dV$.

If the mass distribution of the body is known, Eq. 2.6 may be used to find the gravitational potential at any point. Note also that, since the potential of a differential mass element is a solution to Laplace's equation, so too is the potential found by quadrature external to the mass distribution.

2.2 Discrete-Mass Models

The simplest model for a small body gravity field is the point-mass gravity field. At sufficiently large distances, the point-mass field (Eq. 2.3) closely approximates the true field. However, in the domain of interest to this work (namely the region within several mean radii of the small primitive body), additional fidelity is often required due to the generally irregular shape of small celestial bodies. Hence, collections of point-masses representing (at the low-fidelity end) the bulk axial mass distribution or (at the higher-fidelity end) the body extent and shape are often used to model the true potential.

As discussed in the previous chapter, the objective of discretized mass modeling is to represent a complex, continous mass distribution with simpler mass structures for which the gravity field may be computed more simply and in closed form. Work in the geophysical and astrodynamics communities has made use of a variety of such simplified mass structures, ranging from point-masses to polyhedra. This research makes use of constant-density spheres, for which it can be shown the gravity field external to the sphere is equivalent to the point-mass field for a singularity at the sphere's center. Constant-density spheres are chosen for their computational efficiency when evaluating the field and their facilitation of concepts like the packing fraction and regional density. From this point forward we will refer to constant-density spheres in general as "mascons".

The potential of a group of mascons can be conceived of equivalently as either a superposition of potentials in the form of Eq. 2.3 or as a discretized approximation of the full potential in Eq. 2.6. Following the latter form, the total mascon potential for N mascons is

$$U(\mathbf{r}) = G \sum_{i=1}^{N} \frac{\rho_i V_i}{|\mathbf{r} - \mathbf{R}_i|} \tag{2.7}$$

where ρ_i, V_i, and $\mathbf{R}_i$ are the density, volume, and center-of-mass position of the ith mascon, respectively. Generally, mascon models also require the sum of mascon masses to equal the body mass:

$$M = \sum_{i=1}^{N} \rho_i V_i \tag{2.8}$$

The potential in Eq. 2.7 can be evaluated at any point outside the mascons themselves. The equivalence of point-mass and constant-density sphere potentials is predicated upon the spherical symmetry of the constant-density sphere mass distribution; when evaluating the potential within a mascon, the symmetry argument no longer holds. Equation 2.7 also helps to explain the classically degraded field evaluations that occur close to the edges of a mascon distribution. When field points are located sufficiently far from the mascon distribution, the denominator in Eq. 2.7 is roughly of the same order of magnitude for the N terms of the summation, thereby approximating the effect of a continous body's gravitation. However, as the field point approaches one or several mascons, the denominators in the related terms of the summation are reduced relative to the denominators of other terms, and the contribution to the total potential due to the nearby mascons grows relative to faraway mascons. In this case the modeled field resembles that of one or a small number of mass singularities with a perturbation term, introducing error relative to what would be measured in the true field above a continous mass.

2.3 Spherical Harmonics

We have shown that the gravitational potential is a solution to Laplace's equation external to the body. Instead of evaluating the potential according to the quadrature in Eq. 2.6, we can alternatively construct a series solution to Laplace's equation to represent the field. The spherical harmonic gravity field model is such a solution; it consists of a series of orthogonal polynomials on the surface of a sphere, the coefficients of which may be calculated or estimated to suit the mass distribution in question.

The orthogonal polynomials themselves are constructed from a set of functions called the associated Legendre functions. These functions represent the latitudinal variations of the gravity field. Kaula [30] gives the associated Legendre functions for degree l and order m as a function of latitude ϕ:

$$P_{nm}(\sin\phi) = \cos\phi^{m} \sum_{t=0}^{k} T_{nmt} \sin\phi^{n-m-2t} \tag{2.9}$$

where $k = \mathrm{int}[(n-m)/2]$. The factor T_{nmt} is given as

$$T_{nmt} = \frac{(-1)^{t}(2n-2t)!}{2^{n} t!(n-t)!(n-m-2t)!}. \tag{2.10}$$

Recursive definitions of the associated Legendre functions exist; however, since these functions are not explicitly used in this research, we do not list the recursive formulae here.

2.3.1 Classical Formulation

The "classical" spherical harmonics formulation is that given in many foundational astrodynamics texts [30, 75, 71, 61]. The classical Legendre form of the spherical harmonic potential for a body with mass M is

$$U = \frac{GM}{r} \sum_{n=0}^{\infty} \sum_{m=0}^{n} \left(\frac{R_{\text{ref}}}{r}\right)^{n} P_{nm}(\sin\phi)[C_{nm}\cos m\lambda + S_{nm}\sin m\lambda] \tag{2.11}$$

where P_{nm} are the associated Legendre polynomials and the coefficients C_{nm} and $\S_{nm}$ are the Stokes coefficients. Equation 5.1 is expressed in spherical coordinates (r, ϕ, λ), representing the radial distance, latitude, and longitude of the field point, respectively. The reference radius R_{ref} may be chosen arbitrarily, but is typically chosen to equal the radius of the sphere that bounds the mass distribution. Note that the series diverges in the general case when $r \geq R_{\text{ref}}$. In practice this means that the spherical harmonic potential cannot be evaluated within the reference sphere. For irregularly-shaped small celestial bodies, this presents a challenge when gravity field evaluations are required near the body surface. A useful alternative form of the spherical harmonics potential separates the zeroth degree term from the summation:

$$U = \frac{GM}{r} + \frac{GM}{R_{\text{ref}}} \sum_{n=1}^{\infty} \sum_{m=0}^{n} \left(\frac{R_{\text{ref}}}{r}\right)^{n+1} P_{nm}(\sin\phi)[C_{nm}\cos m\lambda + S_{nm}\sin m\lambda] \tag{2.12}$$

For numerical conditioning purposes, a normalization is sometimes performed on the Stokes coefficients. The normalization yields coefficients on approximately the same order of magnitude for each degree of the harmonic series. These normalized forms are

$$\begin{aligned} \overline{C}_{n,m} &= \mathcal{N}_{n,m} C_{n,m} \\ \overline{S}_{n,m} &= \mathcal{N}_{n,m} S_{n,m} \end{aligned} \tag{2.13}$$

where $\mathcal{N}_{n,m}$ is a normalization factor given by

$$\mathcal{N}_{n,m} = \sqrt{\frac{(n+m)!}{(2-\delta_{0,m})(2n+1)(n-m)!}} \tag{2.14}$$

To maintain the expressions of the potential in Eq. 5.1 and 5.2, the associated Legendre functions must be normalized by multiplying by the inverse of $\mathcal{N}_{n,m}$.

2.3.2 Pines' Formulation

The classic Legendre form of spherical harmonics series suffers from singularities at the poles. Instead, the well-known, singularity-free Cartesian approach known as Pines' Method is employed here [54]. The components of the unit vector are given as:

$$\begin{aligned} r &= \sqrt{x^2 + y^2 + z^2} \\ s &= x/r \\ t &= y/r \\ u &= z/r = \sin\phi \end{aligned} \tag{2.15}$$

and the gravitational potential is:

$$U_P = \frac{\mu}{r}\left[1 + \sum_{n=0}^{\infty}\left(\frac{R}{r}\right)^n \sum_{m=0}^{n} A_{n,m}(u)\Big\{C_{n,m}\rho_m(s,t) + S_{n,m}\iota_m(s,t)\Big\}\right], \quad (2.16)$$

where μ is the gravitational parameter, r is the radial distance of the evaluation point relative to the center of mass of the attracting body, R is the radius of the reference sphere for the attracting body, $A_{n,m}$ is called the derived Legendre polynomial of degree n and order m, $\rho_m(s,t)$, and $\iota_m(s,t)$ are recursively defined, position-dependent quantities, and $C_{n,m}$ and $S_{n,m}$ are the Stokes coefficients of the attracting body. The derived Legendre functions can be defined in relationship to the Legendre functions by

$$A_{n,m}(u) = \frac{d^m}{du^m}P_n(u). \quad (2.17)$$

Note that the Legendre functions are simply the zeroth order associated Legendre functions ($P_n(u) = P_{n0}(u)$). Lundberg and Schutz [37] studied the stability of recursion relationships for $A_{n,m}$, and recommended the recursion

$$A_{n,m}(u) = \frac{1}{n-m}[(2n-1)uA_{n-1,m} - (n+m-1)A_{n-2,m}], \quad (2.18)$$

which we use in this work. The normalized form of this recursion (for use with normalized Stokes coefficients) may be found in Lundberg and Schutz[37]. Recursive forms for $\rho_m(s,t)$, and $\iota_m(s,t)$ are

$$
\begin{aligned}
\rho_0(s,t) &= 1 \\
\iota_0(s,t) &= 0 \\
\rho_m(s,t) &= \mathrm{Re}\{(s+t\sqrt{-1})^m\} = s\rho_{m-1}(s,t) - t\iota_{m-1}(s,t) \\
\iota_m(s,t) &= \mathrm{Im}\{(s+t\sqrt{-1})^m\} = s\iota_{m-1}(s,t) + t\rho_{m-1}(s,t)
\end{aligned}
\tag{2.19}
$$

2.4 Polyhedral Surface Integration

Werner and Scheeres [79] published a closed-form solution for the gravitational potential, attraction, gravity gradient, and Laplacian of a closed, constant-density polyhedron for the purposes of asteroid gravity modeling. Polyhedra have been used in the geophysical community to represent buried gravitational anomalies; Werner and Scheeres advanced that work by reducing the number of required trancendental function evaluations and expressing their solution in terms of physical vectors and distances. The method hinges on a conversion of the volume integral in Eq. 2.6 to a surface integral via the Gauss divergence theorem. The theorem holds for closed polyhedra (even nonconvex ones) and other simple shapes. An overview of the major results is given here.

Suppose a polyhedron of constant density ρ, with edges and triangular facets indexed by e and f, respectively. Each facet has an outward-oriented normal vector $\hat{\mathbf{n}}_f$, and each edge of that facet has an outward-oriented edge normal vector $\hat{\mathbf{n}}_e^f$ perpendicular to both the edge and $\hat{\mathbf{n}}_f$. For the facet f, we can define

$$\mathbf{F}_f = \hat{\mathbf{n}}_f \hat{\mathbf{n}}_f. \tag{2.20}$$

Let edge of length e_{ij} connect two vertices, P_i and P_j, with positions relative to an arbitrary field point $\mathbf{r}_i$ and $\mathbf{r}_j$, respectively. Edge ij necessarily borders two facets, denoted A and B. For this edge, we can define an "edge dyad"

$$\mathbf{E}_{ij} = \hat{\mathbf{n}}_A \hat{\mathbf{n}}_{ij}^A + \hat{\mathbf{n}}_B \hat{\mathbf{n}}_{ij}^B. \tag{2.21}$$

Let the distances from P_i and P_j be $r_i = |\mathbf{r}_i|$ and $r_j = |\mathbf{r}_j|$, respectively. We can then define the dimensionless quantity

$$L_e = \ln \frac{r_i + r_j + e_{ij}}{r_i + r_j - e_{ij}} \tag{2.22}$$

For a triangular face f containing the vertices P_i, P_j and P_k, we can calculate dimensionless factor ω_f associated to the face:

$$\omega_f = 2 \arctan \frac{\mathbf{r}_i \bullet \mathbf{r}_j \times \mathbf{r}_k}{r_i r_j r_k + r_i(\mathbf{r}_j \bullet \mathbf{r}_k) + r_j(\mathbf{r}_k \bullet \mathbf{r}_i) + r_k(\mathbf{r}_i \bullet \mathbf{r}_j)} \tag{2.23}$$

Using these quantities, the gravitational potential and acceleration, respectively, of a closed polyhedron with density ρ are:

$$\begin{aligned} U &= \frac{1}{2} G\rho \sum_{e \in \text{edges}} \mathbf{r}_e \bullet \mathbf{E}_e \bullet \mathbf{r}_e \cdot L_e - \frac{1}{2} G\rho \sum_{f \in \text{faces}} \mathbf{r}_f \bullet \mathbf{F}_f \bullet \mathbf{r}_f \cdot \omega_f \\ \nabla U &= -G\rho \sum_{e \in \text{edges}} \mathbf{E}_e \bullet \mathbf{r}_e \cdot L_e + G\rho \sum_{f \in \text{faces}} \mathbf{F}_f \bullet \mathbf{r}_f \cdot \omega_f \end{aligned} \tag{2.24}$$

The gravity gradient and Laplacian can also be easily calculated from the same quantities necessary for finding the potential and acceleration, but we leave it to the reader to find full expressions in Werner and Scheeres [79]. Note that these expressions do not require the polyhedron to be convex; it may even possess sharp overhangs, interior empty space, or holes.

Since polyhedral shape models for small celestial bodies can be reconstructed from remote observation, and estimates of bulk density can be obtained from observations of the body's interaction with other matter or assumptions about its composition, the polyhedral gravity model provides a convenient means of modeling small body gravity fields both prior to and during a space mission. The model provides a field representation everywhere above the surface and does not suffer from the singularity effects of the mascon approach. However, the nonlinear functions present in the model can cause the calculations to become computationally inefficient, especially as the number of facets and edges grows.

We also note that, while the approach in [79] applies to constant-density polyhedra, polyhedra can be discretized into constituent polyhedra, each with its own density. By summing the gravity contributions from each constituent polyhedron, the polyhedral model can be extended to heterogeneous bodies.

Indeed, further work from Scheeres [62] and Takahashi and Scheeres [69] has applied that extension to model asteroid density heterogeneities.

Chapter 3

MultiMESH Small Body Gravity Models

In this chapter[1], the development of mascon models is revisited at small bodies with the goal of providing efficient gravity evaluations over a global exterior domain. The resulting gravity modeling tool, based around the Multilayer Mascon and Exterior Spherical Harmonics (MultiMESH) approach, is designed to suit a broad range of small bodies of interest. It employs a flexible shape model packing method, guided by a small body's geometry, to represent the body with a set of discrete, spherical elements. These elements are then assigned either point-mass or spherical harmonic gravity signatures based on their size and location. Only constant-density spheres with point-mass gravity signatures are considered "mascons" in this work; the use of other discretized-mass models (i. e. spherical caps, flat disks, etc.) is possible, but they are not considered here to support faster model evaluations. In fact, arrays of point masses provide discrete approximations of finite surface or volume elements [41]. In this chapter, mass elements with spherical harmonics gravity signatures are referred to exclusively as "spherical harmonics elements" or "core

---

[1] Work from this chapter was published in a peer-reviewed journal as:
P. T. Wittick and R. P. Russell, "Mixed-Model Gravity Representations for Small Celestial Bodies Using Mascons and Spherical Harmonics," *Celestial Mechanics and Dynamical Astronomy*, 131 (7):1-29, 2019.

elements". The term "element" is used to refer to either type of spherical body. Once the packing geometry is fixed, a two-step linear least-squares estimator solves for the gravitational parameters and/or spherical harmonics coefficients of the elements using measurements of the body's true gravitational potential. Packing geometries that result in particularly ill-conditioned problems are initialized with a constant-density *a priori* state in order to reliably obtain solutions. Near-surface measurements of a constant-density polyhedral gravity model are treated as observations of the true gravity field of the body in question for all simulations in this work. However, because the constant-density assumption is likely not realistic, using the polyhedral field as truth is only a first step toward the eventual use of in-situ spacecraft observations of the true gravity field.

Note that, in this chapter, explicit treatment of primary body center-of-mass and inertia properties is excluded due to the constant-density polyhedral truth used in the gravity inversion and the currently static nature of the MultiMESH approach. Center-of-mass and inertia properties provide additional constraints to mass distributions that could be exploited in future works, particularly when observations regarding dynamics (e.g. wobble, precession, nutation, non-principal axis spin) are available.

3.1 Packing and Layering Techniques

In the context of small bodies, "packing" is the process of determining how the interior space of a body, represented by its polyhedral shape model, will be discretized. The MultiMESH packing procedure arranges point-mass and spherical harmonics elements within a small body shape model to represent the body's physical extent and total mass. All packed elements are assumed to be spheres, and the gravity signature of each element is determined only after the packed element geometry is fixed.

The shape model packing trade space is defined by three axes: the size and shape of the valid element placement domain, how the location of each element is determined within that domain, and the size or spacing of each element. The MultiMESH approach uses a combination of manual and automated means to control a particular model's location within this trade space.

Packing techniques used by [72] are adapted for the current work and combined with additional methods to control the valid spatial domain for element packing. The first technique requires a three-dimensional grid placed around and through a body shape model, the nodes of which are defined to be "in" or "out" of the shape model. The in/out status of each node is predetermined by calculating the signed solid angle subtended by a shape model about the node ([79]). Shape models subtend a solid angle of 4π about interior points and less than 4π about exterior points. Since a given node may be characterized as "in" or "out" relative to any given shape model, the in/out status of a grid of points may be recomputed for repeatedly reduced versions of a shape model to create useful and different valid packing domains in a scheme referred to herein as "layering".

Layering adds a useful degree of freedom to the design of MultiMESH models. Its primary benefit results from the added ability to restrict how closely discrete elements are packed to the surface. As discussed in Chapter 2, mascon models suffer from degraded surface potential evaluations due to the proximity of mass singularities. By restricting the location of mass elements beneath some depth via layering, the loss of surface field fidelity can be mitigated. [58] have previously optimized a spherically-symmetric mascon burial scheme for the Earth; a similar idea is extended to small celestial bodies via layering in this work.

Shape model reduction, or shape erosion, can be performed in a variety of manners. Here, focus is exclusively placed on vertex scaling, and polyhedral face-vertex associations do not change when the shape model is scaled. First, let the set of all original shape model vertex vectors be

$$\mathbf{V} = \{\mathbf{r}_1,\, \mathbf{r}_2,\, \ldots,\, \mathbf{r}_p,\, \ldots,\, \mathbf{r}_Z\} \tag{3.1}$$

where Z is the total number of vertices, $p \in [1, Z]$, and the origin is the center of mass of the constant density polyhedral model. To obtain the scaled shape model vertices, each original vertex vector is scaled by a factor α_p to obtain the new vector set

$$\mathbf{V}' = \{\alpha_1\mathbf{r}_1,\, \alpha_2\mathbf{r}_2,\, \ldots,\, \alpha_p\mathbf{r}_p,\, \ldots,\, \alpha_Z\mathbf{r}_Z\}. \tag{3.2}$$

Depending on how the scale factors are chosen, the scaled shape model can be more or less distorted from its original shape. When every scalar is equivalent, the result is a uniformly scaled shape model with no change in physical proportions. However, for elongated bodies, the distant vertices of uniformly scaled shape models shift by greater absolute distances than closer ones, resulting in the packing of discrete elements nearer the body surface in some regions than in others. Uneven burial depth results in nonuniform mitigation of the near-field singularity effect, which we seek to avoid.

In order to ensure uniform mitigation of the singularity-induced field degradation, a dynamic selection of α_p is introduced that enforces a constant shift distance for each vertex. This method of shape model scaling is referred to in this work as fixed radial depth (FRD) scaling. Note that both uniform and FRD scaling methods can generate scaled polyhedra that partially lie outside of the original shape model if a vertex position vector pierces the surface more than once. While both methods are suitable for demonstration at 433 Eros, Chapters 4 and 5 of this work consider scaling methods more suited to extremely nonconvex bodies. One method in this grain shifts the shape model vertices in the direction of the local gravity vector (or local plumb line including body rotation) by some fixed distance, while another erodes an interior 3D in/out grid by a constant number of grid elements in all directions.

Consider the shape model scaling depicted in Fig. 3.1, where the scaled vertices are indicated in prime notation ('). Define the radial distance relative to the mass center of shape model vertices p and q to be $r_p = |\mathbf{r}_p|$ and $r_q = |\mathbf{r}_q|$, respectively. To ensure the scaled shape model exists at a fixed radial depth

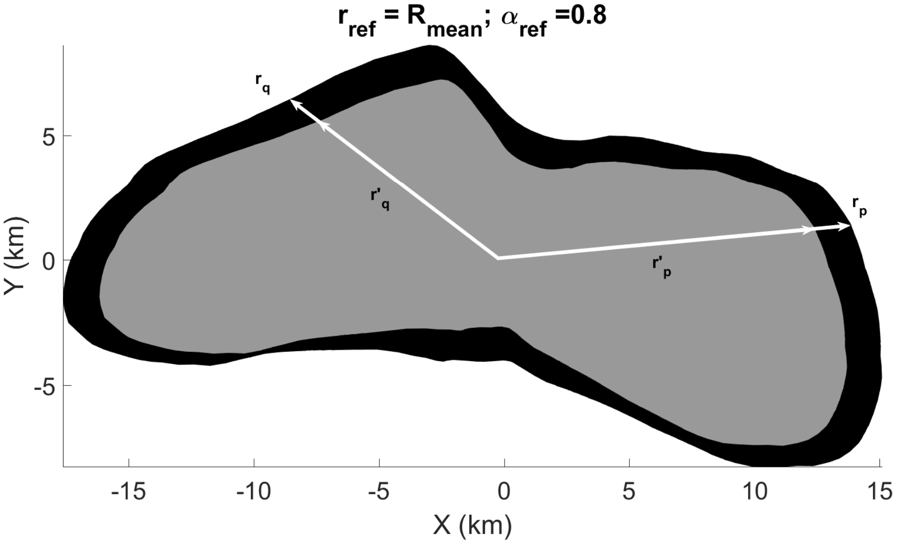

Figure 3.1: Cross-section of full- and FRD-scaled shape models for 433 Eros in the body-fixed XY plane

relative to its original version, the following must be true:

$$K = r_q - r'_q = r_p - r'_p \quad \forall\, p, q \tag{3.3}$$

where K is a constant and $p, q \in [1, Z]$. The standard length difference K may be set independently; however, in order to more minutely control the shape distortion induced by the scaling, it is useful to define two constituent tuning parameters instead. To this end, the standard length K is alternatively defined as the difference between some reference distance, r_{ref}, and its scaled counterpart, $r'_{\text{ref}} = \alpha_{\text{ref}} r_{\text{ref}}$.

$$K = r_{\text{ref}} - r'_{\text{ref}} = r_{\text{ref}} - \alpha_{\text{ref}} r_{\text{ref}} \tag{3.4}$$

Then, the reference distance (r_{ref}) and reference scale factor (α_{ref}) are chosen as tuning parameters since they uniquely define K. Choosing the appropriate reference distance for a set of models or a particular body influences how the fractional scale factor (α_{ref}) translates into physical distances. Also, using a reference scale factor analogous to the uniform scale factor in uniform scaling allows for a more natural description of FRD scaled models (i.e. "an 80% scale shape model").

Together with a vertex's radial distance, the tuning parameters must also uniquely determine the scale factor α_p for the pth vertex for all $p \in [1, Z]$. By equating Eq. (3.4) to the rightmost side of Eq. (3.3), then substituting scaled vertex expressions from Eq. (3.2), α_p is obtained as a function of the tuning parameters.

$$\alpha_p = 1 - \frac{r_{\text{ref}}}{r_p}(1 - \alpha_{\text{ref}}) \tag{3.5}$$

In order to maintain a closed polyhedron after scaling, each scaled vertex may be neither exterior to the original shape model nor reflected across or located at the origin ($0 < \alpha_p \leq 1,\ p \in [1, Z]$). Therefore, some constraints must be placed on the values of the tuning parameters. By enforcing the condition on α_p, bounds on α_{ref} are obtained:

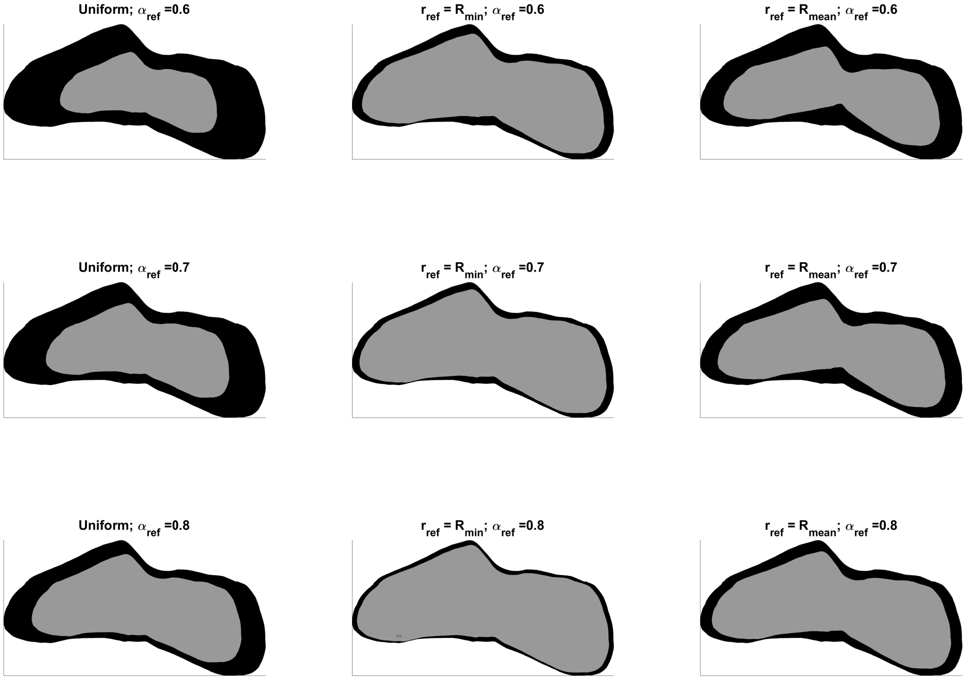

Figure 3.2: Cross-sections of full (black) and scaled (gray) shape models for 433 Eros, illustrating the effect of the scaling tuning parameters: α_{ref} and r_{ref}

$$1 - \frac{r_{\min}}{r_{\text{ref}}} < \alpha_{\text{ref}} \leq 1 \tag{3.6}$$

The choice of r_{ref} will, of course, affect the range of possible reference scale factors; this effect is particularly notable for bodies with large major-to-minor axis ratios. Figure 3.2 compares the effects of different scaling methods and choices of r_{ref} on the final shape of the scaled shape model for 433 Eros. Note the void regions introduced by uniform scaling in the lobes of the body as well as the more regular distribution of void space in the FRD scaled models.

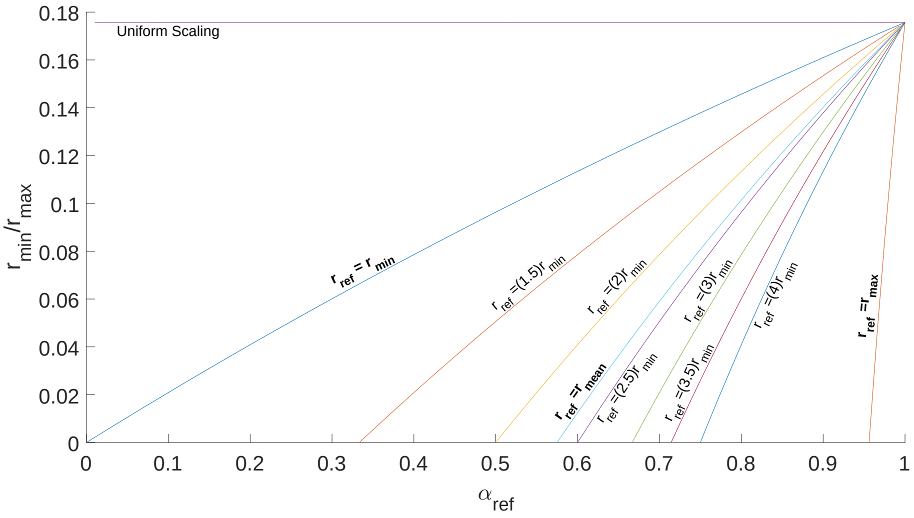

Figure 3.3: Contours of r_{ref} illustrate shape distortion as a function of α_{ref} for an FRD scaled shape model

Figure 3.3 contains contours for several choices of r_{ref}, showing the relationship between α_{ref} and shape distortion for each. Choosing $r_{\text{ref}} = r_{\text{min}}$ ensures that α_{ref} can take any value in $(0, 1]$, but, as the diagrams in Fig. 3.2 show, significant changes in α_{ref} have much less effect on the physical size of the scaled polyhedron than might be expected. Choosing instead $r_{\text{ref}} = r_{\text{mean}}$, where r_{mean} is the mean body radius, results in a more intuitive physical scaling, but has the effect of reducing the valid range of reference scale factors for elongated bodies. Note that a proper choice of r_{ref} results in mascon arrays that better represent elongated body shapes in regions distant from the volumetric center, while still allowing for the burial of mascons for the purpose of mitigating surface potential errors.

The concept of a packing layer flows naturally from the process of shape model scaling described above. Conceptually, a packing layer is a region of space contained entirely within the full-scale shape model that is bounded externally by either the full-scale shape model or a reduced-scale shape model and internally by either a reduced-scale shape model or the origin. Recomputation of the in/out status of the 3D grid defines the points belonging to a given layer. Multiple layers of elements may be packed by repeatedly scaling the shape model and performing this in/out recomputation. This process allows the placement of larger elements near the core and smaller ones closer to the surface to reduce memory and computation time without significant reduction of field fidelity near the body surface.

Three primary packing methods are used to place elements within valid spatial domains, resulting in three distinct packing structures. Refer to Table 3.1 for a summary description and Fig. 3.4 for a visual representation of these fundamental packing structures. The first structure consists of one or more large spherical elements placed in the largest allowable spaces of a full- or reduced-scale shape model. Initially, an element is placed at a user-defined starting location within the shape model, then shifted automatically by small distances to find a location at which its radius is maximized. The direction of each shift is defined to be opposite the direction of the closest shape model vertex. This shifting is performed repeatedly until some tolerance on the change in element radius is met. Tardivel [72] used this technique to place a single large element. Here, Tardivel's approach is modified to place multiple elements in the same fashion (see Fig. 3.4a). Elements packed in this manner

Table 3.1: Descriptions of Packing Structures

Structure Name	Description
Core	3D packing; typically few in number; large elements placed in the largest-allowable regions within a shape model; typically located close to the center of mass of a body; can be either mascons or SH, but typically SH
Infill	3D packing; typically many in number; small, uniformly spaced elements. These fill all available space within a layer; can be either mascons or SH, but typically mascons
Shell	2D packing; typically many in number. Point-mascon elements affixed to the surface of a scaled shape model

are dubbed "core" elements, regardless of their eventual gravity signatures (i. e. point-mass or spherical harmonics).

The second packing structure is more directly adapted from [72]. These elements are placed with their centers at the interior nodes of the three-dimensional in/out grid. Note that grid placement is used here for computational ease and does not result in a minimum volume arrangment. Elements may be spaced more closely or widely to achieve the desired model resolution, with the maximum resolution being that of the underlying grid. This packing method is naturally dependent on the repeated recomputation of the in/out grid for each layer of elements. Since elements packed in this manner fill all available grid space within a given layer, they are referred to as "infill" elements (see Fig. 3.4b).

The third packing structure depends solely on the scaling of shape models. Elements are simply assigned positions at defined points on the surface of a scaled shape model. Possible locations are vertices, facet centroids, or other points resulting from facet subdivisions (see Section 3 and Fig. 3.6

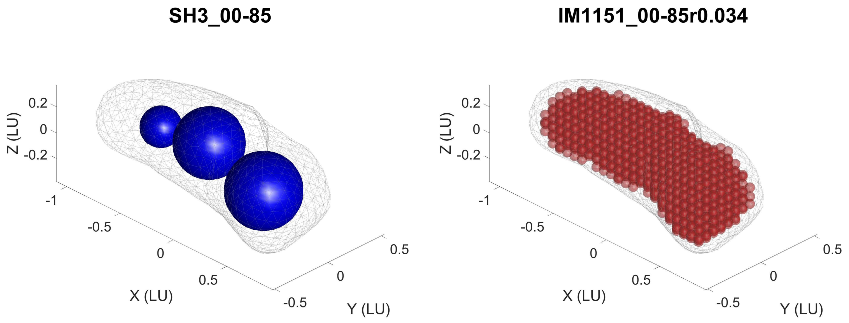

(a) Core

(b) Infill

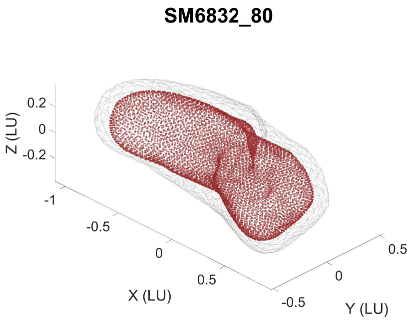

(c) Shell

Figure 3.4: Asteroid 433 Eros packed with the three basic packing structures in Table 3.1; refer to subsection 2.4 for information on model ID nomenclature

for details on splitting facets). Elements placed in this manner constitute "shell" structures due to their 2D arrangement and are always considered to have a point-mass gravity signature (see Fig. 3.4c). The shell elements are superimposed on the existing model without constraints on the presence or locations of any existing element types.

The three packing techniques and resulting element structures, in combination with layering, can be used to generate a variety of packed-element schemes. These schemes can contain any combination of one or more of the three packing structures at varying layer depths and element sizing/spacing. This flexibility allows for expanded degrees of freedom that can be explored for optimizing models in terms of speed and memory footprints.

3.1.1 Example Packing Procedure

A two-dimensional, qualitative packing procedure is outlined here to demonstrate how the three packing structures in Table 3.1 build on one another in a hybrid model. This subsection refers throughout to Fig. 3.5, and details a 2D analogue of a core-infill-shell packing arrangement for a fictional elongated and irregular body.

Prior to starting the packing procedure, several inputs are required: shape model vertices and facet-vertex associations; in/out grid for full-scale shape model; number of layers in the model; scale factors for each layer; start positions for any iteratively-placed elements; spacing for infill elements; placement method for any shell elements, and; which structures are to be packed in which layer or region.

Packing always begins with the innermost layer and moves outward toward the shape model surface. First, the shape model is scaled to form an external bound for the innermost layer (Fig. 3.5a) according to the FRD scaling method discussed in Section 2.1. Then, the in/out grid is recomputed to

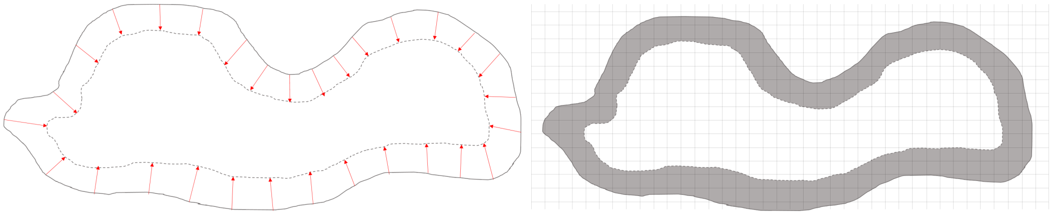

(a) Scale Shape Model for Core and Infill Packing

(b) Recompute In/Out Grid

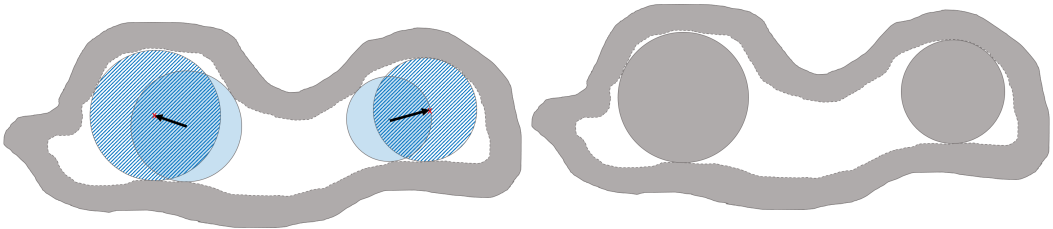

(c) Pack Core Elements

(d) Revise In/Out to Exclude Large Elements

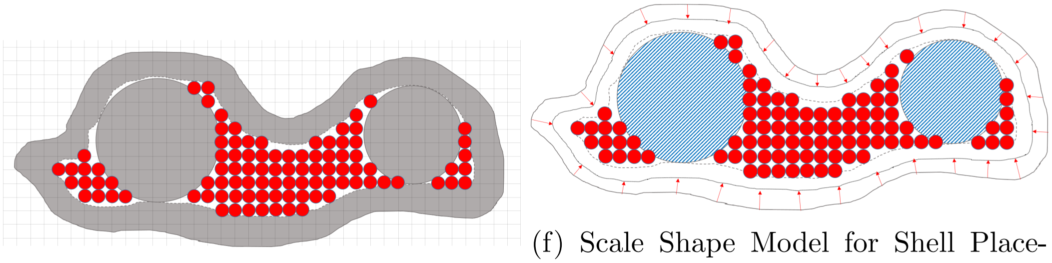

(e) Pack Infill Elements

(f) Scale Shape Model for Shell Placement

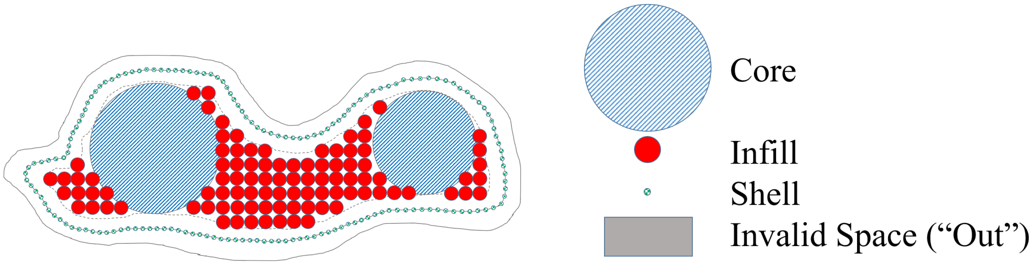

(g) Fix Shell Elements

Figure 3.5: Conceptual 2D illustration of a Core-Infill-Shell packing procedure; packing proceeds from subfigure (a) to subfigure (g)

determine which nodes lie within the innermost layer (Fig. 3.5b). The region determined to be exterior to the active layer is shaded in Fig. 3.5. Then, the requisite number of core elements are initialized in their specified starting locations, and a search is performed for each one for the largest allowable space (Fig. 3.5c). The elements' net motions from start to finish are indicated by black arrows. Next, the in/out grid is again recomputed to exclude any nodes falling within the newly placed core elements (Fig. 3.5d). Infill elements are then placed at all available nodes based on the specified spacing (equal to 1 grid unit for this case, see Fig. 3.5e). With the inner layer complete, the procedure moves to the construction of the outer shell. The original shape model is again downscaled to the desired shell depth (Fig. 3.5f). In this example the shell depth occupies a void region for ease of illustration, but any shell depth with a positive radius is valid. Finally, shell elements are affixed to the surface of the new scaled shape model (Fig. 3.5g). While this example makes use of all three packing structure types, it is emphasized that a given model may have any number, combination, or arrangement of core, infill and shell elements.

3.2 Force Model

Once the packing procedure is complete, the location and spacing of every element is known and fixed. The model incorporates both point-mass signatures and exterior spherical harmonics expansions into its force model. Here, expressions for the gravitational potential and acceleration due to spherical harmonics and point-mass sources are reviewed and placed in the context of

MultiMESH models. The final superposition of these two field representations to yield the total potential model is also presented.

The classic Legendre form of spherical harmonics series suffers from singularities at the poles. Instead, the singularity-free Pines' Method (see Chapter 2) is employed here [54]. Key quantities for the method are repeated here with specialized indexing for the multi-body case.

Suppose a model contains several discrete elements with spherical harmonic gravity signatures, indexed with i. The magnitude and components of the kth field point position vector relative to the center of the ith spherical harmonics element are given as:

$$\begin{aligned} r_{ik} &= \sqrt{x_{ik}^2 + y_{ik}^2 + z_{ik}^2} \\ s_{ik} &= x_{ik}/r_{ik} \\ t_{ik} &= y_{ik}/r_{ik} \\ u_{ik} &= z_{ik}/r_{ik} \end{aligned} \tag{3.7}$$

The gravitational potential at this point due to the element is written:

$$U_{P,ik} = \frac{\mu_i}{r_{ik}} \left[1 + \sum_{n=0}^{\infty} \left(\frac{R_i}{r_{ik}} \right)^n \sum_{m=0}^{n} A_{n,m}(u_{ik}) \left\{ C_{n,m}^i \rho_m(s_{ik}, t_{ik}) + S_{n,m}^i \iota_m(s_{ik}, t_{ik}) \right\} \right], \tag{3.8}$$

where μ is the gravitational parameter, r_{ik} is the radial distance of the kth evaluation point relative to the center of mass of the attracting body, R_i is the radius of the Brillouin sphere for the attracting body, $A_{n,m}$ is the derived Legendre function of degree n, $\rho_m(s_{ik}, t_{ik})$, and $\iota_m(s_{ik}, t_{ik})$ are recursively defined, position-dependent quantities, and $C^i_{n,m}$ and $S^i_{n,m}$ are the spherical harmonics coefficients of the ith attracting body. The integers n and m are limited to a maximum degree and order, respectively. The reader is referred to Chapter 2 of this work and specifically Eqs. 2.17, 2.18 and 2.19 for further information about how to obtain $A_{n,m}$, $\rho_m(s_{ik}, t_{ik})$ and $\iota_m(s_{ik}, t_{ik})$.

Now suppose that the gravity model also contains some number of discrete elements with point-mass gravity signatures (constant-density spheres/mascons), indexed with j. The point-mass gravitational potential $U_{MC,jk}$ due to the jth mascon at the kth evaluation point is

$$U_{MC,jk} = \frac{\mu_j}{r_{jk}}, \tag{3.9}$$

where μ_j is the gravitational parameter of the jth mascon and r_{jk} is the radial distance from the mascon centroid to the evaluation point. Now, to assemble: if a given body is represented by N mascons and M spherical harmonics elements, we have a force model for the field that is simply the sum of $N+M$ scalar potentials. The component potential fields may be superposed to yield the total gravitational potential $U_{\text{MESH},k}$ at the kth evaluation point:

$$U_{\text{MESH},k} = \sum_{i=1}^{M} U_{P,ik} + \sum_{j=1}^{N} U_{MC,jk}. \tag{3.10}$$

Since the terms in each summation in Eq. (3.10) may be computed independently, the opportunities for parallelization when performing potential evaluations are obvious. The total gravitational acceleration vector, $\ddot{\mathbf{R}}_k$, at the same point is expressed as the gradient of the potential:

$$\ddot{\mathbf{R}}_{\mathrm{MESH},k} = \sum_{i=1}^{M} \nabla U_{P,ik} + \sum_{j=1}^{N} \Big(-\frac{\mu_j}{r_{jk}^3}\mathbf{r_{jk}} \Big), \tag{3.11}$$

where the acceleration due to the ith spherical harmonics element is

$$\nabla U_{P,ik} = \ddot{\mathbf{r}}_{ik} = a_1\hat{\mathbf{i}} + a_2\hat{\mathbf{j}} + a_3\hat{\mathbf{k}} + a_4\frac{\mathbf{r}_{ik}}{r_{ik}} \tag{3.12}$$

with the coefficients defined by

$$\begin{aligned}
a_1 &= \sum_{n=0}^{\infty} \frac{R_i^n \mu_i}{r_{ik}^{n+2}} \sum_{m=0}^{n} A_{n,m}(u_{ik}) m E_{n,m} \\
a_2 &= \sum_{n=0}^{\infty} \frac{R_i^n \mu_i}{r_{ik}^{n+2}} \sum_{m=0}^{n} A_{n,m}(u_{ik}) m F_{n,m} \\
a_3 &= \sum_{n=0}^{\infty} \frac{R_i^n \mu_i}{r_{ik}^{n+2}} \sum_{m=0}^{n} A_{n,m+1}(u_{ik}) D_{n,m} \\
a_4 &= \sum_{n=0}^{\infty} \frac{R_i^n \mu_i}{r_{ik}^{n+2}} \sum_{m=0}^{n} [(n+1+m)A_{n,m}(u_{ik}) + u_{ik}A_{n,m+1}(u_{ik})] D_{n,m}
\end{aligned} \tag{3.13}$$

The reader is referred to Pines' original work for full definitions of the recursive quantities $E_{n,m}$, $F_{n,m}$, and $D_{n,m}$. For this work, a Fortran implementation of Pines' method is employed.

The assignment of spherical harmonics and point-mass gravity signatures is technically arbitrary for any particular packed element. However, the characteristics of mascons and spherical harmonics suggest rules of thumb for assignment schemes. Note, for instance, that the radius ratio (R_i/r_{ik}) in Eq. 3.8 determines the magnitude of the nonspherical gravity terms relative to the two-body term for spherical harmonic element i at field point k. In order to enhance the observability of element spherical harmonic coefficients in the upcoming estimation step, the radius ratio should be maximized for the set of fixed r_{ik} describing the truth measurement locations. Therefore, spherical harmonics signatures are assigned only to the largest discrete elements (i.e. choosing maximal R_i value(s)). As a result, larger elements are generally better candidates for spherical harmonics gravity signatures than smaller ones. Additionally, point-mass fields are quick to evaluate and are well-suited to a parallel implementation. Therefore, point-masses are better suited for infill and shell packing structures that contain many elements.

3.3 Estimation of Model Parameters

The simplest option when designing a mascon model is to assign a constant bulk density to each of the elements [72]. Recent work has shown that acceleration measurements collected from flybys at small bodies can be used to estimate both mascon- and spherical harmonics-based gravity model parameters [49, 68]. Additionally, [58] demonstrated that measurements of a high-degree and -order spherical harmonics field for the Earth may be used in a batch least squares estimation problem to determine the masses of a buried spherical array of mascons. A similar technique, outlined here, is extended to the small body problem for the MultiMESH approach.

For this application, estimates of the gravitational parameters (μ) of all elements present in the model as well as the coefficients ($C_{n,m}$ and $S_{n,m}$) of any spherical harmonics elements in the model are sought. To ensure numerical stability in the estimation procedure, normalized spherical harmonics coefficients are used (see Eqs. 2.13 and 2.14). The associated Legendre polynomials are normalized by the inverse of $\mathcal{N}_{n,m}$ in the Legendre form of the potential.

The measurement model is drawn from Eq. (3.10) since the estimation process fits the MultiMESH potential to the constant-density polyhedral potential. Note that spherical harmonic element gravitational parameters and harmonic coefficients are nonlinear in the observation-state partials; hence they cannot be simultaneously and independently estimated. Additionally, solutions obtained via a suitable nonlinear estimator can be biased by the requisite use of an *a priori* state estimate.

Hence, two additional estimation schemes are considered, both of which involve splitting the nonlinear problem into two linear problems to be solved in sequence and iterated over until convergence. The first setup separates the estimation of all element gravitational parameters from that of all spherical harmonics coefficients, while the second setup separates only the gravitational parameters belonging to spherical harmonics elements into a second state vector. Both linear problem setups have the effect of avoiding the nonlinearity in the system, but experiments with all three described estimator setups show that the second linear problem setup yields lower potential residuals than either of the other two estimators for all models tested. Mathematically, the chosen double-linear problem is set up as follows:

$$
\begin{gathered}
\mathbf{z}_1 = \mathbf{H}_1\mathbf{x}_1 + \epsilon, \\
\mathbf{z}_1 = [U_{\text{poly},1} - (\mathbf{H}_2\mathbf{x}_2)_1, \ldots, U_{\text{poly},k} - (\mathbf{H}_2\mathbf{x}_2)_k, \ldots, U_{\text{poly},l} - (\mathbf{H}_2\mathbf{x}_2)_l]^T, \\
\epsilon \sim \mathcal{N}(\mathbf{0}, \mathbf{R}) \\
\mathbf{x}_1 = [\mu_1, \ldots, \mu_j, \ldots, \mu_N, \overline{C}^1_{2,0}, \overline{S}^1_{2,1}, \ldots, \overline{C}^1_{n_1,m_1}, \overline{S}^1_{n_1,m_1}, \ldots, \\
\overline{C}^i_{2,0}, \overline{S}^i_{2,1}, \ldots, \overline{C}^i_{n_i,m_i}, \overline{S}^i_{n_i,m_i}, \ldots, \overline{C}^M_{2,0}, \overline{S}^M_{2,1}, \ldots, \overline{C}^M_{n_M,m_M}, \overline{S}^M_{n_M,m_M}]^T
\end{gathered}
\tag{3.14}
$$

$$
\begin{gathered}
\mathbf{z}_2 = \mathbf{H}_2\mathbf{x}_2 + \epsilon, \\
\mathbf{z}_2 = [U_{\text{poly},1} - (\mathbf{H}_1\mathbf{x}_1)_1, \ldots, U_{\text{poly},k} - (\mathbf{H}_1\mathbf{x}_1)_k, \ldots, U_{\text{poly},l} - (\mathbf{H}_1\mathbf{x}_1)_l]^T, \\
\epsilon \sim \mathcal{N}(\mathbf{0}, \mathbf{R}) \\
\mathbf{x}_2 = [\mu_{\text{SH},1}, \ldots, \mu_{\text{SH},i}, \ldots, \mu_{\text{SH},M}]^T.
\end{gathered}
\tag{3.15}
$$

Note that state vector $\mathbf{x}_1$ contains the whole set of N mascon gravitational parameters (indexed with $j \in [1, N]$) and all harmonic series coefficients for every element with a spherical harmonics gravity signature. State vector $\mathbf{x}_2$ contains all M spherical harmonics element gravitational parameters (indexed with $i \in [1, M]$). Observation vectors $\mathbf{z}_1$ and $\mathbf{z}_2$ contain measurements of the *partial* potential corresponding to the problem being solved. The partial potential is calculated for each problem at each iteration by subtracting the contributions ($(\mathbf{H}_1\mathbf{x}_1)_k$ or $(\mathbf{H}_2\mathbf{x}_2)_k$) of the states in the alternate state vector from the total gravitational potential $U_{\text{poly},k}$ at the kth observation location for all $k \in [1, l]$. These contributions change from iteration to iteration based on the current values in the state vectors. The components of the observation error vector ϵ are assumed to be zero-mean, independent and identically distributed with covariance matrix $\mathbf{R}$. The observation error covariance matrix can be viewed as a weighting matrix that helps improve the conditioning of the estimation problem, and has the added benefit of allowing some observations to be weighted more heavily than others.

Utilizing a linear problem setup avoids the need for an entire *a priori* state and covariance for most cases (see below). When needed for the initialization of the first filter, the point-mass partial potential contributions $(\mathbf{H}_2\mathbf{x}_2)_k$ of spherical harmonics elements in the model are pre-calculated assuming that each spherical harmonics element has an equivalent bulk density to that of the body.

For models with very badly conditioned $\mathbf{H}_1$ matrices, experiments suggest that enforcing a constant-density prior state and covariance result in lower acceleration errors and smaller residuals than the standard no-prior setup. Hence, a test is introduced prior to iterating over the two linear problems wherein the condition number of $\mathbf{H}_1$ is estimated. If $\texttt{cond}(\mathbf{H}_1) > 10^{11}$, then the constant-density prior is enforced at the first iteration, and the prior state and covariance are updated after each iteration with the new solutions for $\mathbf{x}_1$ and $\mathbf{x}_2$. For all estimator setups, the estimator is considered to be converged if the change in the performance index is less than 10^{-10} or if the number of iterations exceeds an arbitrary maximum iteration count. When required, the constant-density *a priori* state vectors contain the values:

$$\begin{aligned}
\mu_{0,i} &= G\rho_{body}V_i\left(\frac{V_{body}}{\sum_{i=1}^{N+M} V_i}\right) \\
\overline{C}_{n,m}^{0,i} &= 0 \quad \forall\, n,m \\
\overline{S}_{n,m}^{0,i} &= 0 \quad \forall\, n,m
\end{aligned} \tag{3.16}$$

where G is the universal gravitational constant, ρ_{body} is the constant density of the body, V_{body} is the total volume of the body's shape model, and V_i denotes the volume of the ith element. The element volume is calculated using either the reference radius of the associated spherical harmonics series or half the distance between mascons. The factor $(V_{body}/\sum_{i=1}^{N+M} V_i)$ in Eq. (3.16) compensates for the empty space in the shape model left over after packing to ensure that the sum total mass of the packed model elements is equivalent to the body mass. Variance values for each type of state in the state covariance matrix, $\mathbf{P_{xx}}$, are tuned for models using normalized length, gravitational potential, and mass units with normalized spherical harmonics coefficients. Note the estimation procedure does not preclude the use of other *a priori* state or covariance values.

In the case where the number of state unknowns exceeds the number of shape model facets, a simple triangular facet bisection method is used to obtain 4^β measurement points per facet, where β is the number of bisections

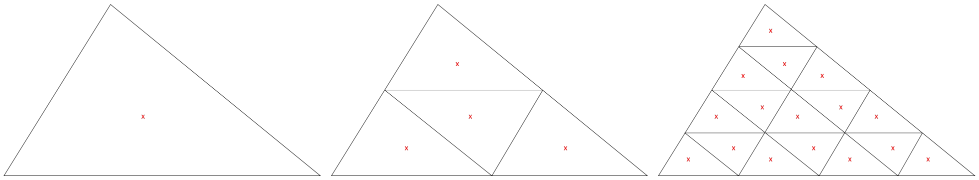

(a) $\beta = 0$ (b) $\beta = 1$ (c) $\beta = 2$

Figure 3.6: An example of triangular facet bisection for $\beta = 0, 1$, and 2; the "x" marks represent the centroid locations for this facet

performed. The bisection method works by subdividing each triangular facet into four similar triangles by connecting the midpoints of each side. The bisection can be performed recursively β times, and the projected centroids of the subdivided triangles are then taken as new measurement points. Figure 3.6 shows how splitting a single triangular facet affects the number and locations of measurements on that facet. When a polyhedron has quadrilateral facets instead of triangular ones, an analogous facet bisection method is used. Each edge of the quadrilateral facet is bisected by a single line segment that also bisects the opposite edge, generating four constituent quadrilaterals. The centroid of each consituent quadrilateral is taken as an additional measurement point, resulting in 5^β measurement points per facet, where β is again the number of recursive splits performed.

Note that several constraints are applied to the estimation problem in a similar way to those used in the referenced gravity inversion literature in Chapter 1. First, the spatial distribution of the mass elements is fixed via the packing algorithm prior to estimation, eliminating the need to estimate element positions. For badly conditioned packing geometries, the final mass distribution estimate is biased to be close to the constant density mascon model via the imposition of a constant density a priori state and use of a constant density polyhedral truth model. Since this work is primarily focused on generating models to perform fast and accurate field evaluations as opposed to estimating realistic density distributions, physically improbable mascon distributions (i.e. extreme mass discontinuities in neighboring mascons) resulting from the estimation process are not deemed problematic. Mass smoothness and continuity constraints are therefore not implemented at this stage. The success of the current work is judged by how closely the model configurations match the exterior gravity field of the polyhedron (which itself is an approximation of the true field), and how well they trade off memory and computational speed with traditional models when performing field evaluations.

3.4 Example at 433 Eros

3.4.1 Performance Metrics

The general performance of a MultiMESH-generated model is defined by its accuracy, evaluation speed, and model size. Computationally fast and accurate models obviously benefit both onboard and ground-based applications regardless of the characteristics of the local CPU. However, given how cheap memory is, model memory footprint is more useful as a tool to compare the computational efficiency of a given memory footprint across modeling approaches. In addition, explicitly considering memory as a performance characteristic aids in the identification of memory-efficient discrete-element frames that are better suited for estimating internal density distributions [49]. Memory footprint is also an important consideration for onboard implementations.

Root mean square (RMS) aggregates of pointwise relative and absolute acceleration errors are used as metrics for model accuracy. Relative errors provide a convenient means of comparing performance across models, while absolute errors provide insight into observability thresholds for potential orbiters using the models. Computational speed for a given model is measured directly using a consistent Fortran compiler and processor combination across all generated models and reported in milliseconds. The runtimes given are averages over 1015200 acceleration evaluations taken at all 10152 vertices of the truth shape model, projected outward using FRD scaling to 100 discrete altitudes. This same set of altitudes is split in two parts for ease of analysis; the first 50 RMS errors are averaged to give a "low altitude" RMS error, while the last 50 RMS errors are averaged to give a "high altitude" RMS error. The MultiMESH software implementation is compiled using the default 'release' settings with Intel®Fortran Compiler 17.0 and run on an Intel®Xeon®E5-1650 v3 CPU at 3.50GHz.

The minimum memory space in RAM required by a given model to provide runtime field evaluations is measured to determine model memory footprint. The minimum memory space is quantified by calculating the required equivalent number of floating point quantities for each model. Each mascon requires the storage of a position vector (3 components) and the gravitational parameter (μ), while each spherical harmonics element requires a position vector for its center, μ, reference radius r_a, and $n_{\max}^2 + 2n_{\max}$ coefficients, where $n_{\max}$ is the maximum degree and order of the spherical harmonics element. Additionally, the size of each uniform layer of mascons (infill or shell) is registered by a single radius value, adding a single floating point quantity per model layer. If we denote η as the total number of memory locations required by a given model containing N mascons, M spherical harmonics elements, and N_L layers, then

$$\eta = 4N + 5M + N_L + \sum_{i=1}^{M} (n_{\max,i}^2 + 2n_{\max,i}) \tag{3.17}$$

Polyhedral models require the storage of all vertex positions (3 floating point numbers per vertex) and an integer mapping matrix (3 integers per face) to relate the vertices to the model facets. The algorithm used in this work to perform field evaluations of polyhedral models also requires the precomputation of several large arrays, adding about 12 times the number of vertices plus 21 times the number of facets less two floating point quantities to the minimum memory size at runtime. Taking into account that integers uaually occupy half the memory of floating point numbers, the equivalent number of floating point quantities that must be stored for a polyhedral model is:

$$\eta_{poly} = 15N_v + \frac{45}{2}N_f - 2 \tag{3.18}$$

where N_v and N_f are the numbers of vertices and facets in the model, respectively. For closed polyhedra, the number of facets is always twice the number

Table 3.2: Relevant Parameters for 433 Eros
([11, 83]; [82])

Parameter	Value
Gravitational Parameter ($\mu = GM_{\text{eros}}$, km^3/s^2)	$(4.463 \pm 0.001) \times 10^{-4}$
Volume (km^3)	2503 ± 25
Bulk Density (kg/m^3)	2670 ± 300
Radius of Nearest Shape Model Vertex (km)	3.219
Mean Radius, r_{mean} (km)	7.311 ± 0.010
Radius of Farthest Shape Model Vertex (km)	17.667
Minimum Surface Normal Acceleration (m/s^2)	2.2×10^{-3}
Radius of the Circumscribing Sphere, R_a (km)	16.0
Reference Scaling Radius, $r_{\text{ref}} = R_{\text{mean}}$ (km)	7.311
Reference Scale Factor Bounds	$0.57 < \alpha_{\text{ref}} \leq 1$
Avg. Execution Time of Eros Truth Model (ms)	0.67

of vertices less four. Substituting this relationship into Eq. (3.18), we obtain:

$$\eta_{poly} = 12N_v + \frac{45}{2}(2N_v - 4) - 2 = 57N_v - 92 \tag{3.19}$$

For the polyhedral truth model (10152 facets, 5078 vertices), the requisite equivalent number of floating point memory locations is 289354. For a lower fidelity, 1708 facet, 856 vertex shape model, the number of required memory locations is 48700.

3.4.2 Identifying Pareto-Optimal Gravity Models at 433 Eros

Given the large set of design parameters in the packing procedure (shape model scale factors, element spacing, number of layers, how to combine core, infill, and shell elements, etc.), gravity signature assignment (how to mix spherical harmonics and mascons, degree and order of SH elements), and gravity inversion (weights/covariances, *a priori* state, choice of truth model, convergence tolerances, etc.), identifying high-performing models generated through the right combination of design choices poses quite a challenge.

One way to address this challenge is to generate a sufficiently large set of models and perform a Pareto sort. This general model set should contain models with varying combinations, sizes, and relative quantities of Core, Infill, and Shell element structures, along with a few different layering schemes using shape model scale factors drawn from throughout the valid range defined by Eq. (3.6). Once the performance of the models in the general set is evaluated, a Pareto sort is performed to identify those models which lie along the efficiency front of the set. Such Pareto optimal models offer valuable alternatives to end users that may have a range of design needs.

Eros was chosen for this example due to its elongated and irregular shape and the availability of data related to the body, obtained from the NEAR mission and Earth-based observation. Acceleration errors are measured against a truth gravitational field calculated from a 10152-facet constant-density polyhedral model of Eros [11]. Note here that the performance of solved MultiMESH models is measured against that of the same truth polyhedral model from which observations were drawn for the estimation procedure. If the models' performance were instead measured against another alternative (e.g. an exterior spherical harmonics field estimated during orbit determination) without changing the source of estimation observations, the information content of the MultiMESH models would not change, but different performance statistics would result. The average CPU time required to obtain field acceleration values for the truth model is provided alongside other relevant Eros parameters in Table 3.2. In terms of the radius of the body's circumscribing sphere (R_a, see Table 3.2), the "low altitude" region for RMS acceleration error calculation (see Section 4.1) is defined to extend from the surface (0 R_a) to 0.15625 R_a. The "high altitude" region is defined to extend from 0.15625 R_a to 0.3125 R_a. Much of the low altitude region falls within the circumscribing sphere, while the outer region contains a more even mixture of points both interior and exterior to the circumscribing sphere.

A large set of gravity models for Eros was generated by coarsely sampling values over broad intervals in the packing parameter space. The result is the model set in Table A.1, which contains 44 MultiMESH-generated models and two lower-resolution polyhedral alternatives. Refer to Appedix C for details on nomenclature for the model ID codes in Table A.1. The low altitude performance results for the model set are visualized in Fig. 3.7 with dual two-dimensional projections of the 3D performance metric space. Similar plots for the high altitude region are shown in Figs. 3.8. Performing a Pareto sort of the models in 3D (using memory size, execution time, and low-altitude error) identifies the nearly the same set of optimal models as performing the sort in four dimensions (by including high-altitude error with the other three metrics). The only exception is model 34, which only appears on the 4D-sorted list due to its less-than-optimal low-altitude error performance. Models that fall along the 4D Pareto front are denoted with bold model numbers in

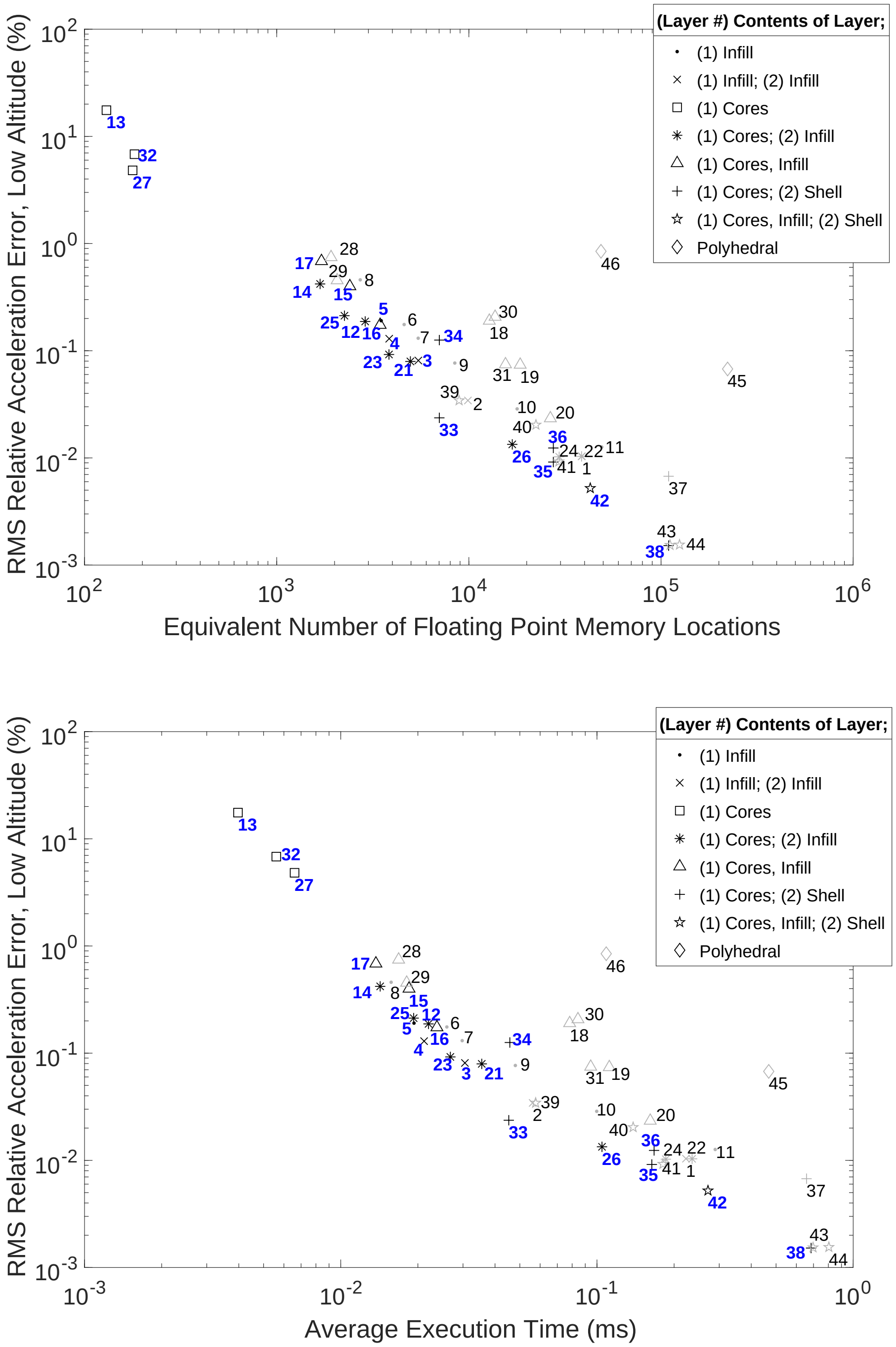

Figure 3.7: Low Altitude Relative Performance Data for the General Model Set in Table A.1

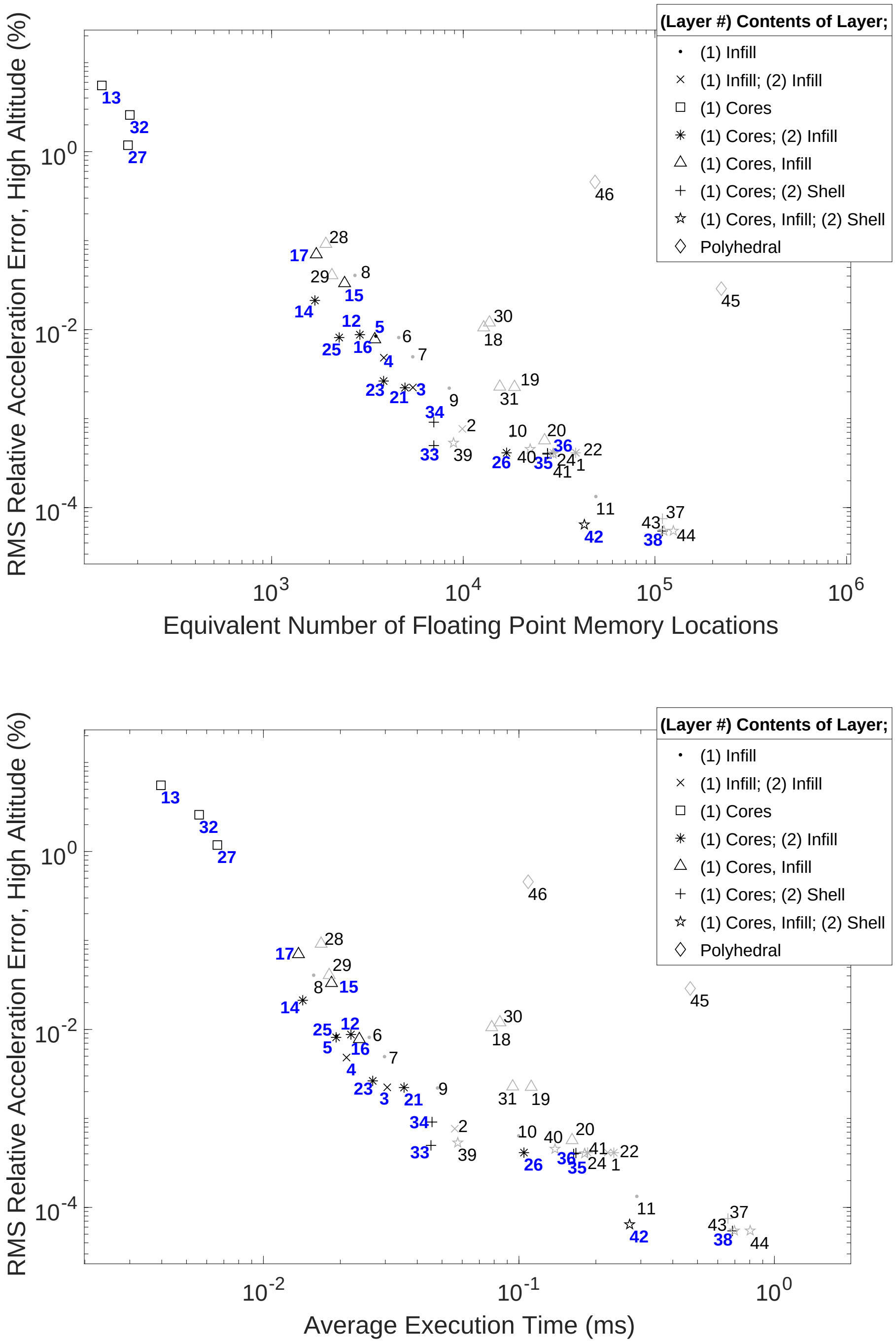

Figure 3.8: High Altitude Relative Performance Data for the General Model Set in Table A.1

column 1 of Table A.1 and are shaded black in Figs. 3.7 and 3.8. Although no constraint preserving the center of mass location has been introduced, its position error is approximately only 0.3% of Eros' circumscribing radius for the models generated here.

Each of the identified Pareto optimal models offers different performance characteristics to users, and are distributed along a range from lower- (model 13) to higher-resolution (model 44). Significantly, the two tested lower-resolution polyhedral models do not fall along the Pareto front of this model set. Every MultiMESH-generated model outperforms each polyhedral alternative along at least one dimension of the performance space, and several do so along every dimension of the performance space. For example, both models 28 and 3 achieve similar levels of accuracy as polyhedral models 46 and 45, respectively, yet they take up less memory by more than an order of magnitude and have average execution times more than ten times faster than their respective polyhedral alternatives.

Examining the entire model set, models 23, 33, and 42 stand out as all-around best performers. All three lie near elbows of the Pareto front that are present in all four performance plots in Figs. 3.7 and 3.8. Each produces a gravity field that has low-altitude relative RMS error levels less than 0.1%. All three also have similar model constructions: an inner core layer consisting of three spherical harmonics elements surrounded by an outer layer of infill or shell mascons (or a combination of both).

Compare the performance of these models to that of their siblings represented by triangles (△) in Figs. 3.7 and 3.8. These models also consist of core elements paired with infill mascons, but the infill mascons instead occupy the same layer as the core elements and fill the empty space around them. These models consistently perform worse than models like 23, 33, and 42.

Many models containing mascon shells (represented by the symbols + and ⋆ in Figs. 3.7 and 3.8) perform notably well. However, when comparing the RMS acceleration errors of the model pairs 33 and 34, 35 and 36, and 37 and 38 (which only differ in the burial depth of their mascon shells), there is a noticeable dependence of model accuracy on shell burial depth. In Chapter 3, the hybrid model design space is further explored to systematically optimize shell burial depths as well as other packing parameters to minimize field errors. Packing parameters like shell burial depth offer unique opportunities for model optimization since changes in their value do not impact the memory footprint or execution time of a particular model.

3.4.3 Model Mass Distributions

While the efficiency benefits of the MultiMESH approach are clear with respect to engineering applications (such as mission design, navigation, and onboard use), it is also useful to examine the typical internal density distributions of the generated models in the interest of future geophysical or planetary science applications. Knowledge of estimated density distributions resulting from the current cost function helps inform decisions about the future need for constraints on the extrema of the element masses or on the smoothness

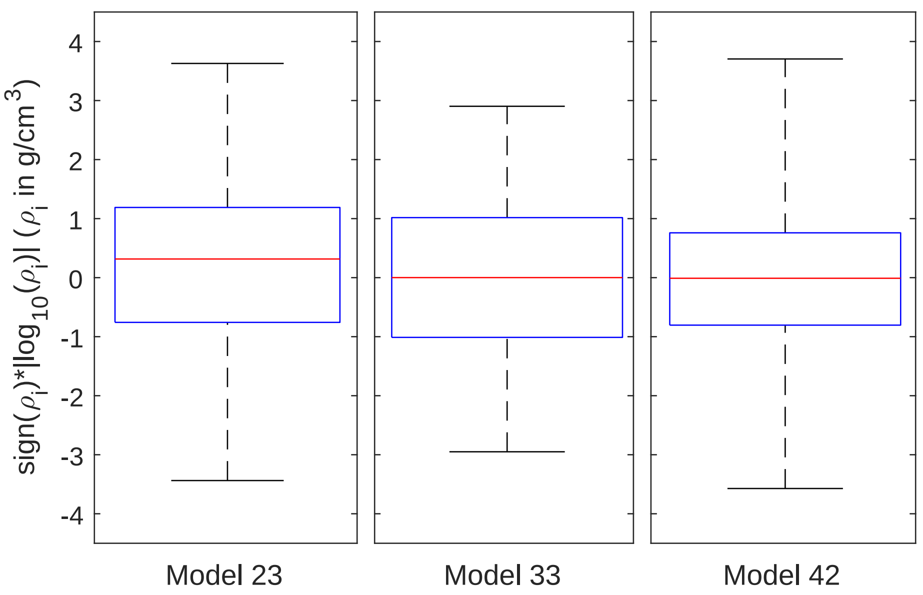

Figure 3.9: Box and whisker plots of the element densities (ρ_i) of models 23, 33, and 42. Whiskers extend to the minimum and maximum element densities in each model, and the median of each distribution is indicated by a horizontal red line.

of the density distribution from element-to-element. A full analysis of each model's element density distribution is beyond the scope of this work; a short presentation of the density distributions for high-performing models 23, 33, and 42 is given instead.

As discussed earlier in this chapter, the estimation procedure solves for element mass distributions such that gravitational potential residuals are minimized, resulting in distributions that can contain both very positive and very negative element densities. Box-and-whisker plots of the density distributions for models 23, 33, and 42 are shown in Fig. 3.9. The median value of the distributions is indicated by a horizontal red line, the boxes contain the density values between the 25th and 75th percentiles of the distributions, and the whiskers extend to the density extrema for each model. Despite the large variation in magnitude of density values in these distributions, note that the middle 50% of elements possess densities within about an order of magnitude of the body bulk density value (≈ 2.67 g/cm^3, see Table 3.2) for each of the three models (despite none of the three models shown requiring the use of a constant-density prior to mitigate an ill-conditioned $\mathbf{H}_1$ matrix).

While the estimation procedure outlined previously yields element gravitational parameters, examining instead the density distribution of the elements can provide additional insight for planetary scince purposes. Calculating the density of core and infill elements is relatively straightforward; core elements have a defined radius attributed to their associated spherical harmonics expansion, and infill elements are spaced at regular intervals, allowing the use of the half-spacing distance as a representative radius for each element. Shell elements, however, require a slightly more complex approach when calculating densities.

Since shell elements are defined by the locations of projected facet centroids, rather than by any physical size or regular spacing, an approximate, representative, and consistent radius for the shell elements must be calculated. That radius is arbitrarily defined here as the maximum distance to the fifth nearest shell element over all shell elements in the model. This choice has several benefits. First, using the distances to the five closest shell elements to each

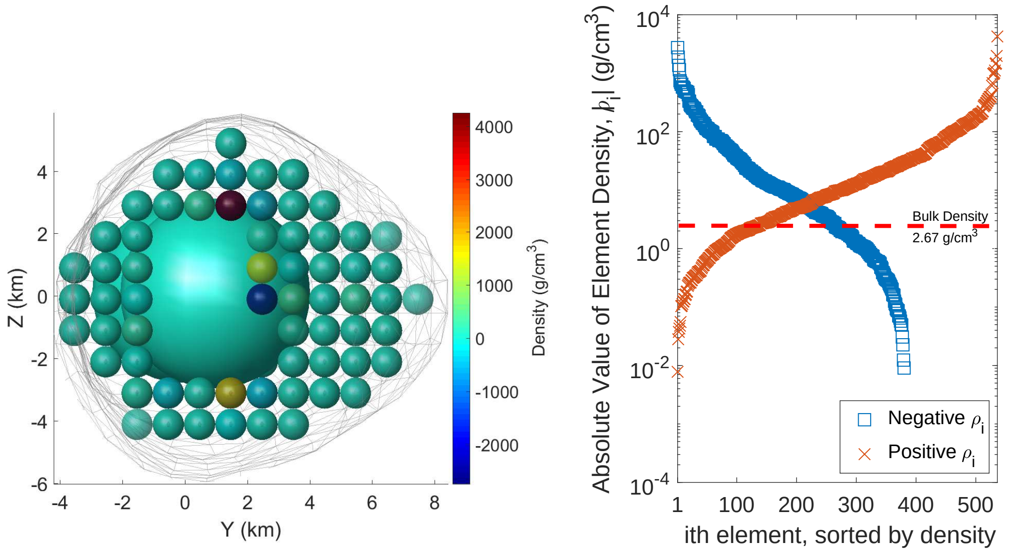

(a) X = 0.82 km, toward -X (b) Individual Element Densities

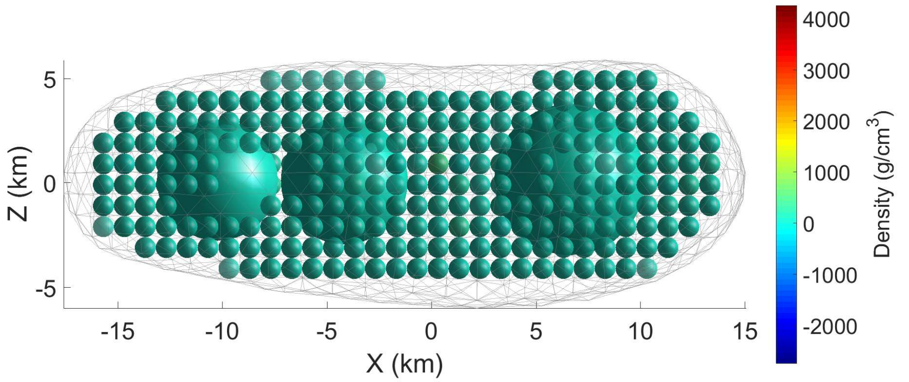

(c) toward -Y

Figure 3.10: Three visualizations of the density distribution of model 23

shell element ensures the consideration of elements located at the centroids of the three neighboring facets plus two more for robustness. The resulting radius, if used to plot the shell element array, is likely to create a near-solid shell of spherical masses, resulting in a relatively uniform distribution of the mass in the shell layer. Lastly, this choice of common radius results in shell element densities within one or two orders of magnitude of the body bulk density, and extreme outlier density values are avoided.

Consider the density distribution of model 23 as a typical example. In Fig. 3.10, several perspectives of the distribution are shown. Figure 3.10a shows a view toward the negative X axis from a plane section at $X = 0.82$ km. Figure 3.10b depicts the sorted values of element densities, split into positive and negative groups for easy depiction on a log scale. Figure 3.10c shows a broader view toward the negative Y axis of the entire mass element array, depicted within a full-scale Eros shape model. Mass elements in Figs. 3.10a and 3.10c are colored according to their individual densities using identical scales. Figures 3.10b and 3.10c demonstrate that the majority of elements have densities that fall within an order of magnitude of the bulk density of Eros. Both the positive- and negative-density curves in Fig. 3.10b have slopes of lower magnitude in this region, indicating large groups of elements with densities in the corresponding density range. However, there are many elements with more extreme densities. The sectioned view shown in Fig. 3.10a shows some of the elements with extreme density values. In a very typical arrangement, elements with very positive and very negative densities are located both near one another and generally close the central axis of the body. While such extreme mass discontinuities pose few problems for engineering applications (provided the external gravity field is sufficiently accurate), additional constraints on the estimation are likely necessary to obtain more realistic (i.e. smooth) density distributions across mass elements.

Finally, recall that the truth for our simulations is a constant density polyhedron, and our element placements are not distributed evenly with respect to volume. Therefore, the resulting distributions must, by definition, have a non-constant density profile. Future works that aim at realistic density reconstruction may constrain the packing with different layer bounds and element geometries to achieve that end.

3.5 Conclusion

In this chapter, discrete-element models have been revisited for the small body gravity problem with the intent to superpose conventional basis functions, optimize the placement of the elements, and maintain or increase the accuracy of the models. By introducing one or more spherical harmonics elements to the model and performing batch least squares estimation of the model parameters, the design trade space for mascon models is expanded. The MultiMESH small body gravity modeling tool is shown to generate and identify Pareto optimal gravity models that, at comparable resolutions, meet or exceed the performance of traditional mascon, spherical harmonics, and polyhedral models for the asteroid 433 Eros. Hybrid model constructions that fill interior space with spherical harmonics elements and surround them with layers of mascons are particularly efficient in terms of execution time and memory space while maintaining high field accuracy compared with the truth model. While less complex gravity models may provide performance benefits outside the circumscribing sphere, the best-performing MultiMESH models shown here offer demonstrated benefits over the conventional polyhedral approach, particularly in the region within the circumscribing sphere where exterior spherical harmonics series diverge. A single MultiMESH model also represents the global near-surface field simulaneously without the need for multiple interior spherical harmonics expansions or for interpolation over large sets of precomputed potential values.

Chapter 4

Hybrid Gravity Models for Small Bodies of Interest

The previous chapter introduced the construction and estimation methods necessary to build MultiMESH small body gravity models using homogeneous polyhedra as reference models. Many different model configurations are possible using the described methods, and it is anticipated that each small body considered may have a different optimal structure. It is hypothesized that an *a priori* search procedure may help identify custom optimal configurations for each body. In this chapter[1], the grid search technique is applied for three small bodies, and the resulting best-performing models are presented. The models and runtime codes are made available online.

This chapter is organized as follows: First, a shape model scaling method is introduced to enable the layered construction of MultiMESH models for nonconvex bodies. Then, the gravity model design space grid search and performance evaluation processes are discussed. Results of the global grid

---

[1] Work related to this chapter was presented as:
P. T. Wittick and R. P. Russell, "Hybrid Gravity Models for Kleopatra, Itokawa, and Comet 67P/C-G," Paper AAS 18-289, *AAS/AIAA Astrodynamics Specialist Conference*, Snowbird, UT, August 2018.

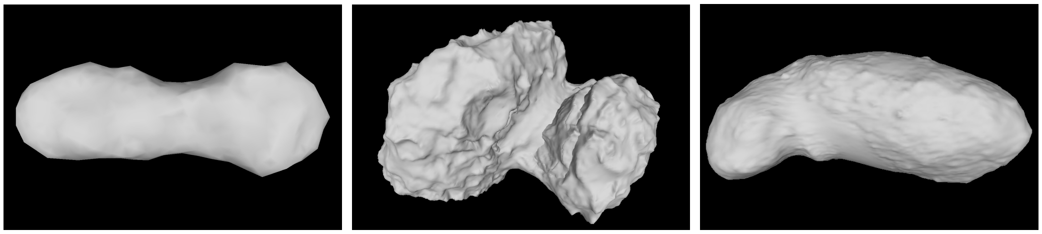

(a) 216 Kleopatra[65] (b) Comet 67P/C-G[73] (c) 25143 Itokawa[20]

Figure 4.1: Three previous, planned, or potential small body mission targets (not shown to equivalent scale).

search of the packing parameter space are given for the irregularly-shaped bodies 216 Kleopatra, 25143 Itokawa, and Comet 67P/Churyumov-Gerasimenko (Fig. 4.1). Several Pareto-optimal models are identified and examined for each body, and further analysis is presented for a demonstrative example at each body. The outcome of the work described here is a set of archivable, high-performance gravity models for several small bodies of interest.

4.1 Shape Model Scaling for Nonconvex Bodies

As discussed in Chapter 3, the MultiMESH approach divides the body's interior into regions that can be packed separately using preset methods according to user-set packing parameters. These regions are referred to as "layers". Layers are bounded externally by the body's full-scale or reduced-scale polyhedral shape model and internally by another sub-scale shape model or the origin (body center of mass). Scaled shape model boundaries are generated by shifting the vertices of the original shape model while maintaining facet-vertex relationships. Many scaling methods exist, including: uniform scaling, where vertex position vectors are scaled by a common factor; fixed radial depth (FRD) scaling, where each vertex is shifted by a common distance along its position vector, and; fixed local perpedicular depth (FLPD) scaling, where vertices are shifted along the local gravitation vector (ignoring rotation effects) by a common distance.

FLPD scaling is now introduced to provide a more robust solution for nonconvex bodies. While any scaling method that shifts vertices along local radial or normal vectors can easily induce shape self-intersection due to large- and small-scale nonconvexities, shifting along the local gravitation vectors results in a scaling determined largely by the bulk mass distribution. As a result, vertices are always shifted "inward" in a local sense. Resulting reduced-scale shape models yield mascon layers that are packed at a nearly constant depth throughout the shape model, regardless of large- or small-scale convexity. This chapter introduces and employs FLPD scaling. See Figure 4.2 for a demonstration of the effects of the three scaling methods on a shape model for 216 Kleopatra.

Note that no accounting is made here for the body's (potentially unknown or uncertain) rotation in inertial space; resulting forces in the body frame would alter the direction of local apparent gravity vectors and result in an entirely different polyhedral scaling. The constant shift distance l_i for each vertex on the polyhedron bounding the i^{th} layer is defined to be

$$l_i = (1 - \alpha_i) l_{\text{ref}} \tag{4.1}$$

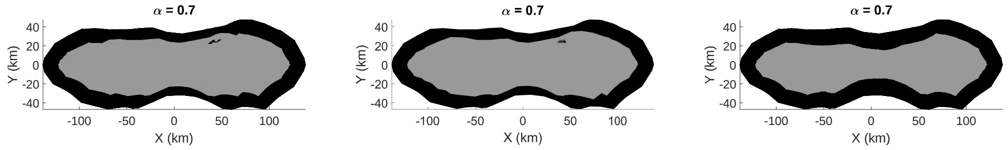

(a) Uniform (b) FRD (c) FLPD

Figure 4.2: Cross-sections at Z = 0 km of a 2292-facet shape model of 216 Kleopatra[65], scaled using (a) uniform, (b) fixed radial depth (FRD), and (c) fixed local perpendicular depth (FLPD) scaling methods. Note the overlap between original (black) and scaled (grey) shape models in (a) and (b), indicated by a black inclusion in the upper right lobe of the scaled shape model.

where α_i is the i^{th} entry of α and l_{ref} is a predefined maximum shift distance. The difference $(1-\alpha_i)$ is used instead of α_i to preserve the notion that larger scale factors should lead to larger shape models. Scaling a polyhedron must not result in self-intersection or reflection of vertices across the origin in order to avoid ambiguity when determining the interior/exterior status of a point in space. Hence the minimum half-chord distance is the maximum allowed shift distance for any vertex. A search is performed over all unique vertex pairs to set the maximum shift distance as follows:

$$l_{\text{ref}} = \frac{1}{2}\min|\mathbf{r}_j - \mathbf{r}_k| \;:\; -1 \leq \frac{\ddot{\mathbf{R}}_j \cdot \ddot{\mathbf{R}}_k}{|\ddot{\mathbf{R}}_j||\ddot{\mathbf{R}}_k|} < \delta << 0 \qquad \forall\, j \neq k;\; j,k \in [1, N_v] \tag{4.2}$$

where N_v is the total number of vertices.

Table 4.1: List of Model Packing Parameters

Symbol	Description	Size
N_L	Number of Layers	1
$\mathbf{M}_p$	Per Layer Packing Method: (A) infill mascons only; (B) core elements only; (C) core elements and infill mascons; (D) shell elements ; (E) empty layer	N_L
$\mathbf{N}_C$	Per Layer Number of Core Elements	N_L
α	Per Layer externally-bounding shape model scale factor	N_L
$\mathbf{d}$	Per Layer infill or shell element spacing distance	N_L
$n_{\max}$	Maximum degree (and order) of any spherical harmonics elements	N_L, $N_{C,\max}$
$\mathbf{r}_{0,C}$	Initial position of core elements	N_L, $N_{C,\max}$, 3

4.2 Design Space Grid Search

Given a polyhedral shape model and scaling method, the position, spacing, and element sizes of a particular MultiMESH model are uniquely determined by the set of packing parameters in Table 4.1. This useful mapping implies that the packing parameter set can be considered a searchable parameterization of the model design space. Varying one or more of these parameters leads to families of configurations for a given body. Ultimately, members of multiple families for a specific body can be evaluated for accuracy, speed, and memory to identify optimal configurations.

The design space for MultiMESH models is clearly broad – varying the value of the parameters in Table 4.1 could concievably result in thousands of unique models for a given body. At the same time the performance characteristics of each model - gravity field accuracy, speed, and size in memory - trade off against one another such that the most accurate models are unlikely to be the fastest and smallest, and vice versa. Hence identifying optimal model

Table 4.2: Model Performance Evaluation Parameters

Body	R_{ref} (km)	Mass (kg)	N_{MMmodels}	$N_{v,\mathrm{ref}}$	$N_{f,\mathrm{ref}}$	N_{meas}	$\overline{\tau}_{\mathrm{truth}}$ (ms)
216 Kleopatra[65, 15]	138 ± 20.7	$4.64 \pm 0.2 \times 10^{18}$	499	1148	2292	179220	1.6E-01
Comet 67P/C-G[73, 27]	2.17 ± 0.01	$1.00 \pm 0.03 \times 10^{13}$	436	25350	49152	647820	3.53
25143 Itokawa[17]	0.2675 ± 0.0005	$3.51 \pm 0.105 \times 10^{10}$	454	25350	49152	647820	3.49

configurations is, in essence, a multi-objective optimization problem with inner loops consisting of the packing and field fitting procedures. Due to the complexity of these inner loops, the design and application of an outer optimization loop is beyond the scope of this work. Instead, a grid search over the packing parameter space is implemented, and models are Pareto-sorted according to their performance characteristics. Practical design criteria are used to limit the dimensionality of the search space and to bound the search such that it remains tractable on a timescale of CPU days.

MultiMESH models' performance is evaluated over twenty surfaces, ten consisting of outwardly-projected shape models, and ten consisting of spherical shells between $1R_{\mathrm{ref}}$ and $2R_{\mathrm{ref}}$. The projected shape model surfaces take advantage of each body's geometry to fill the region within the circumscribing sphere with evaluation points. The altitudes to which the shape models are projected are logarithmically spaced. Individual evaluation points on those surfaces are located at each shape model facet centroid. Evaluation points on the spherical shells correspond to an $n = 15130$ numerical solution to Thomson's problem[74], which seeks a minimum-potential (i.e. equally spaced) configuration of charged particles on the surface of a sphere, thereby avoiding oversampling at the poles common to an angular grid. The spherical shell evaluation surfaces are spaced linearly, and are designed to sample the space in which low-altitude science orbits might fly. See Table 4.2 for exact measurement point totals (N_{meas}) and other parameters relevant to model performance evaluation.

The MultiMESH software implementation is written in Fortran 90 and compiled with the Intel®Fortran Compiler 17.0. All model builds and performance evaluations are performed on a desktop computer running Windows 10 OS with an Intel®Xeon®E5-1650 v3 CPU at 3.50GHz using standard "Release" settings. Reported execution time is measured in CPU seconds elapsed and averaged over all field measurement points. No parallelization techniques are implemented during the measurement of execution time. Model fidelity is measured at each point using both the absolute and relative acceleration error magnitude and reported in aggregate for each evaluation surface as a root-mean-square (RMS) relative acceleration error magnitude. Results for selected evaluation surfaces are highlighted in the following sections. Average execution times ($\overline{\tau}_{\text{truth}}$) are reported in Table 4.2 for the polyhedral truth models used for each body. Table 4.2 also provides the total number of MultiMESH models generated for each body ($N_{\text{models,tot}}$).

Exploration of the vast number of MultiMESH model design possibilites is conducted via an automated global grid search of the packing parameter space for each body, defined by the parameters in Table 4.1. The dimensionality of the search space is driven primarily by the number of layers, N_L, and the number of core elements in each layer, $\mathbf{N}_C$. The number of searchable dimensions also varies depending on a model's general configuration. With many searchable grid points along each dimension of the space, the procedure can quickly become intractable if no bounds are placed on the value of certain key parameters and the search is conducted at too fine a resolution. Each of these challenges requires mitigation measures to ensure a feasible and efficient grid search; these measures are detailed in Appendix B.

Once the grid search is complete, the best-performing models are identified using a Pareto sort[48]. The models identified are called "Pareto-optimal" because their performance meets or exceeds that of all other models generated along at least one dimension of the performance metric space. Rather than identifying a single optimal model, Pareto sorting produces a subset of high-performance models to suit a variety of user requirements.

For the models generated for this work, the performance metric space has up to twenty-two dimensions; it consists of memory footprint, execution time, and the twenty RMS acceleration error values corresponding to the set of evaluation surfaces. In order to limit the number of Pareto-optimal models, the Pareto sort takes place only over execution time, memory footprint, and RMS relative acceleration error at the surface and on the circumscribing sphere. Users interested in specific orbit regimes or rendezvous and landing may sort the models using only those acceleration errors obtained at surfaces relevant to their needs.

4.3 Hybrid Model Solutions

A global grid search of the packing parameter space is conducted for each body, resulting in hundreds of distinct models for each. A nomenclature for shorthand labels of individual MultiMESH models (known as model "ID codes") is defined in Appendix C, based on the layering, quantity, gravity signature, and spacing of consituent elements. For the large model sets presented in this work, it is useful to define a shorthand label for classes of similar models.

The number of layers (N_L) and the packing methods ($\mathbf{M}_p$) for each layer control the general structure (i. e. which types of elements get placed in which regions) of a model. Since these two parameters can take only a limited set of values, it is simple to construct a short alphanumeric code to represent a model class. A class code begins with the total number of layers in a model (e. g. 2). Then, a series of letters follows, whose length matches the number of layers. The letters correspond to the packing method used in each layer (as defined in Table 4.1), proceeding from the innermost to the outermost layer. For example, a model with an inner layer of infill mascons and an outer layer of shell mascons would belong to the 2AD model class.

A discussion of the characteristics and performance of models generated in the grid search for 216 Kleopatra, Comet 67P/C-G, and 25143 Itokawa now follows. Original shape models[65, 73, 20] for each of the bodies were obtained from the Jet Propulsion Laboratory's Asteroid Radar Research site, the European Space Agency's Image Archives, and NASA's Planetary Data System, respectively. Resolution reduction, where necessary for packing efficiency and the generation of benchmark polyhedral models, was performed using the free software Autodesk Meshmixer. In the discussion below, relative errors and normalized length units (LU) are employed for quantities relating to the performance test to facilitate comparisons across bodies and with other gravity field modeling approaches. One LU is equivalent to the circumscribing radius (R_{ref}) of the body in question. For each body, the performance of the generated MultiMESH model set is plotted against that of two or more polyhedral models at the body surface and on the reference sphere. Several recommended models from the subset of Pareto-optimal choices are examined in detail.

4.3.1 216 Kleopatra

Table 4.3: Recommended Pareto-Optimal Models for 216 Kleopatra

#	ID Code	Model Class	Memory Footprint (equiv. fpq)	Avg. Execution Time (ms)	$\epsilon_{\text{RMS,surf}}$ (%)	$\epsilon_{\text{RMS},R_{\text{ref}}}$ (%)
61	SM1146_55	1D	4585	2.41E-02	9.62E-01	2.18E-02
122	IM960_00-55r9_SM1146_65	2AD	8426	4.58E-02	6.42E-01	1.82E-02
156	IM1144_00-65r9_SM4584_75	2AD	22914	1.25E-01	2.70E-01	5.80E-03
173	IM316_00-55r13_SM4584_75	2AD	19602	1.08E-01	2.88E-01	5.36E-03
421	SH2_IM385_00-55r11_SM4584_75	2CD	20012	1.12E-01	2.80E-01	5.28E-03
500	P1146	poly	32683	8.12E-02	7.62E-01	1.12E-01
501	P1718	poly	49042	1.22E-01	2.40E-01	1.66E-02
502	P2000	poly	57022	1.39E-01	6.96E-02	2.46E-03

The latest shape model for 216 Kleopatra published by Shepard, et al.[65] indicates the body is about 276 km along its long axis and about 78 km along its shortest axis, making it both a relatively large asteroid and quite an elongated one. Hence, there is a large region near the body in which con-

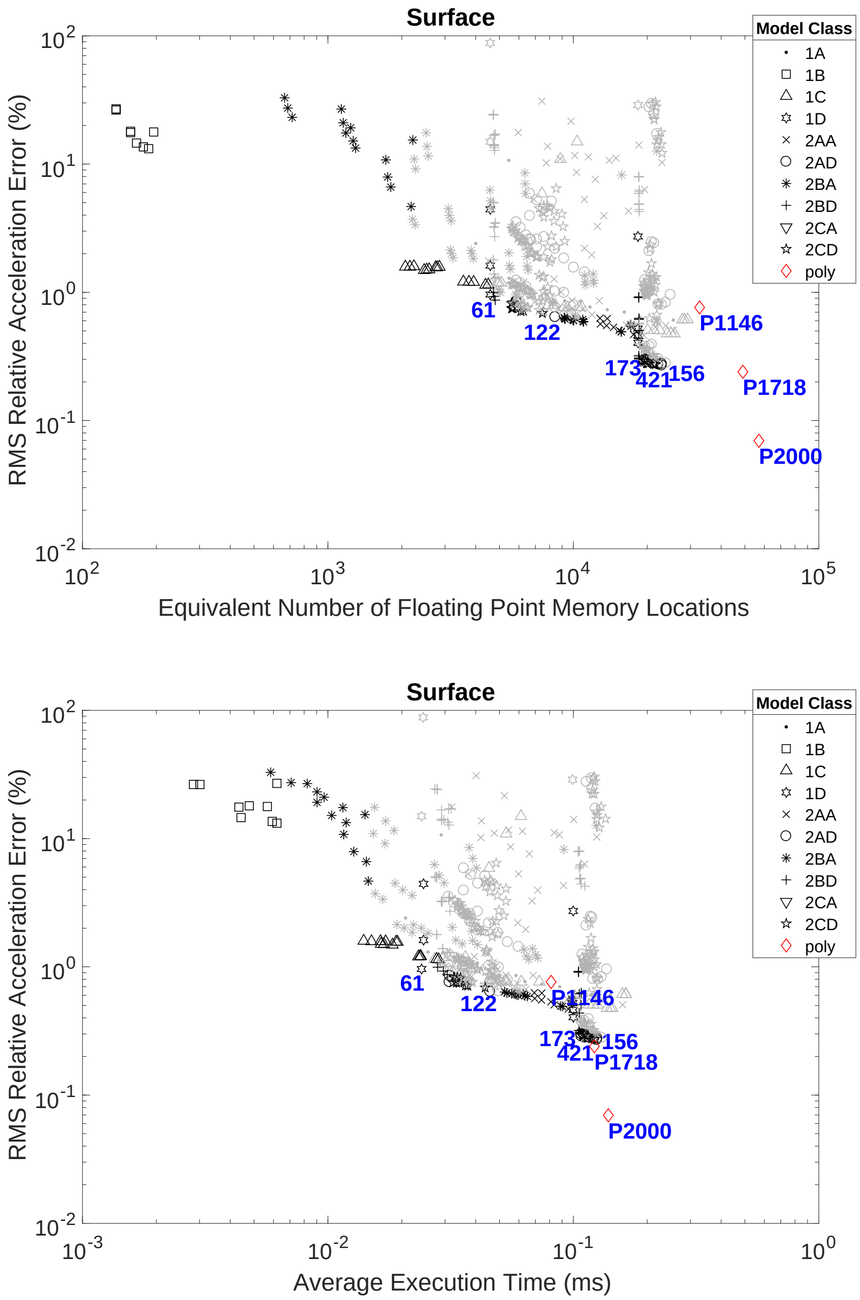

Figure 4.3: 2D Surface performance space projections for all generated 216 Kleopatra models; 4-D Pareto-optimal models are shaded black. Recommended models are labeled with their model numbers.

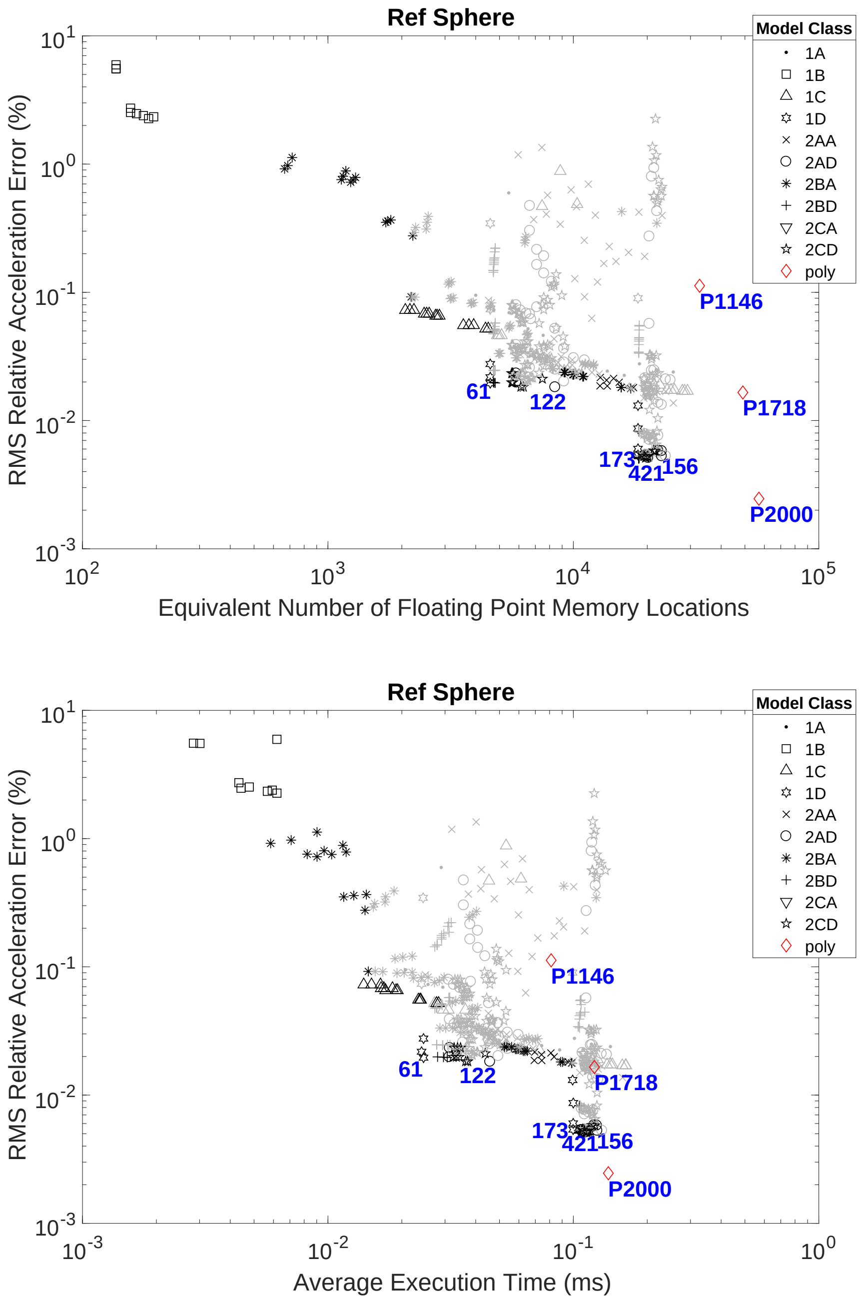

Figure 4.4: 2D Reference sphere performance space projections for all generated 216 Kleopatra models; 4-D Pareto-optimal models are shaded black. Recommended models are labeled with their model numbers.

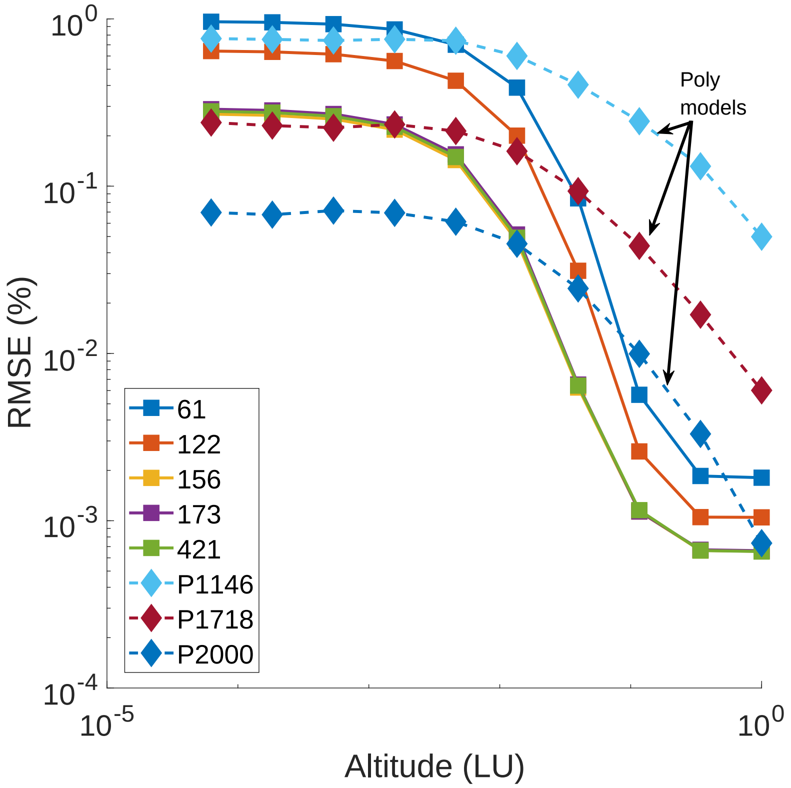

Figure 4.5: RMS acceleration error magnitude over the ten projected shape model test surfaces for five recommended Pareto-optimal MultiMESH models and two reduced-resolution polyhedral models for 216 Kleopatra (Table 4.3)

ventional spherical harmonics gravity representations diverge, yet the gravity field remains both highly irregular and dynamically significant relative to other forces (SRP, third-body effects, etc.). Additionally, the only shape models available for Kleopatra are derived from ground-based observations since no spacecraft has yet orbited the body. Current knowledge of Kleopatra's physical properties therefore approximates that typically available at the early stages of science mission planning.

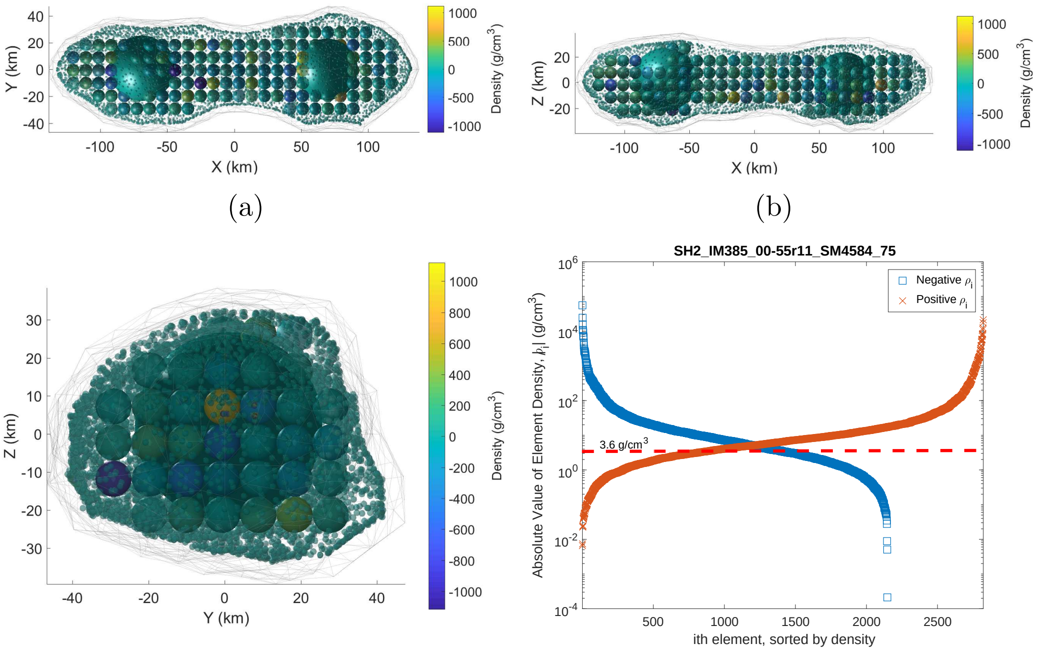

(a) (b)

(c) (d)

Figure 4.6: Element density distribution (a)-(c) and sorted mass element densities (d) for 216 Kleopatra Model 421 (class: 2CD; ID: SH2_IM385_00-55r11_SM4584_75). A dotted line indicates the magnitude of the body's bulk density for reference.

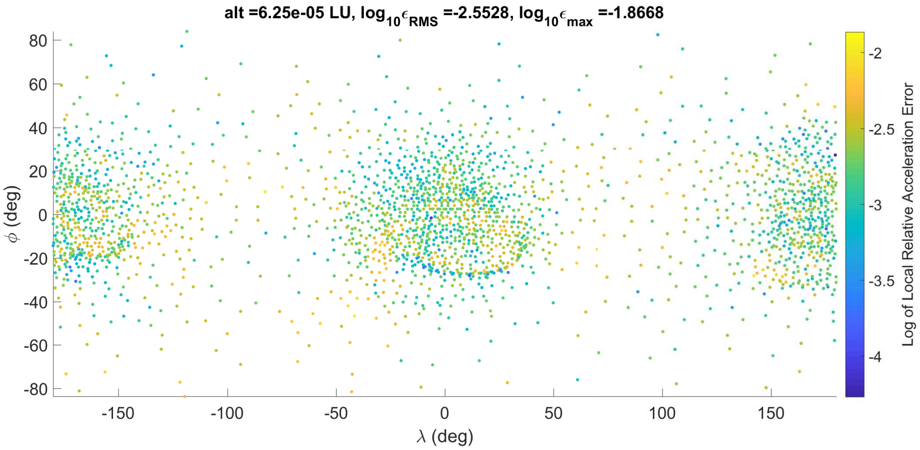

Figure 4.7: Log of local relative acceleration errors at the body surface for Kleopatra model 421 (class: 2CD; ID: SH2_IM385_00-55r11_SM4584_75)

Note that the reference gravity field for Kleopatra is based on a lower-resolution polyhedral model than for either Itokawa or Comet 67P (2292 facets vs. 49152 facets). The reduced memory size of the truth model means that any proxy MultiMESH models must be carefully limited in size to still achieve a performance benefit. While higher memory limits must be observed for 67P and Itokawa as well, the MultiMESH model build algorithm is restricted to generating smaller MultiMESH models at a finer resolution in the design space for the case of Kleopatra, achieving a similar total number of models for each body.

Figures 4.3 and 4.4 show the speed, memory, and error performance of the 499 MultiMESH models generated during the grid search and three comparative reduced-resolution polyhedral models (denoted “PXXXX”, where

“XXXX” is the number of facets in the model). The three polyhedral models form a clear performance “front” falling close to the high-resolution side of the MultiMESH models. The 2000-facet polyhedral model #502 in particular exceeds the accuracy of any MultiMESH model with a similar execution time. Note however, that model #502 has a resolution approaching that of the reference model (with 2292 facets), and that as the facet count of a polyhedral model approaches that of the reference, acceleration errors near the surface will quickly approach zero. For any mascon-based model to achieve the same convergence, the total number of mass elements must increase toward infinity, wiping out any benefit to speed or memory footprint.

Select MultiMESH models do perform well enough to serve as efficient proxies for lower-resolution polyhedral models. Five high-performing models are identified in Table 4.3; their acceleration error performance in the low-altitude domain is compared with that of polyhedral models #500, #501 and #502 in Fig. 4.5. Note that MultiMESH models #156, #171, and #421 exhibit similar errors near the body surface to polyhedral model #501 while offering improvements in execution time and memory footprint. The MultiMESH models’ advantage only grows as their acceleration error falls relative to #501 with increasing altitude. Model #61 could also serve as an efficient proxy for polyhedral model #500; their surface acceleration errors are comparable, while #61 is roughly three times as fast.

The density distribution and surface error performance of the most accurate of the recommended Kleopatra models (#421) are shown in Fig. 4.6

and Fig. 4.7, respectively. Note the effect of FLPD scaling on the consistent burial depth of the shell mascon layer in Figures 4.6a, 4.6b, and 4.6c. Element densities are mostly concentrated within two orders of magnitude of the body bulk density, with a relatively small fraction of mass elements having densities of very small or very large magnitude (Fig. 4.6d). Due to Kleopatra's extremely elongated shape, the error evaluation points appear distorted when mapped into latitude-longitude space in Fig. 4.7. However, the error profile highlights the fact that surface relative acceleration errors fall below 1% in all but a few select regions on the body surface.

4.3.2 Comet 67P/Churyumov-Gerasimenko

Table 4.4: Recommended Pareto-Optimal Models for Comet 67P/C-G

#	ID Code	Model Class	Memory Footprint (equiv. fpq)	Avg. Execution Time (ms)	$\epsilon_{\mathrm{RMS,surf}}$ (%)	$\epsilon_{\mathrm{RMS},R_{\mathrm{ref}}}$ (%)
54	SM2500_55	1D	10001	4.40E-02	1.10	4.37E-02
136	IM1057_00-55r13_SM2500_75	2AD	14230	6.28E-02	8.00E-01	3.62E-02
167	IM1057_00-55r13_SM10000_85	2AD	44230	2.03E-01	3.39E-01	9.86E-03
235	SH4_00-55_IM1447_55-82r9	2BA	6034	2.95E-02	1.78	8.10E-02
389	SH4_IM3209_00-75r9_SM2500_85	2CD	23034	1.06E-01	6.55E-01	2.36E-02
437	P2500	poly	71272	1.74E-01	1.70	2.56E-01
438	P12288	poly	350230	8.58E-01	5.10E-01	4.64E-02

Comet 67P was recently visited by the European Space Agency's Rosetta probe and Philae lander. Hence there exists a wealth of scientific data about the body, and the associated shape models are quite detailed. Interest in 67P as a mission target was recently demonstrated in the form of a New Frontiers mission concept called Comet Astrobiology Exploration SAmple Return

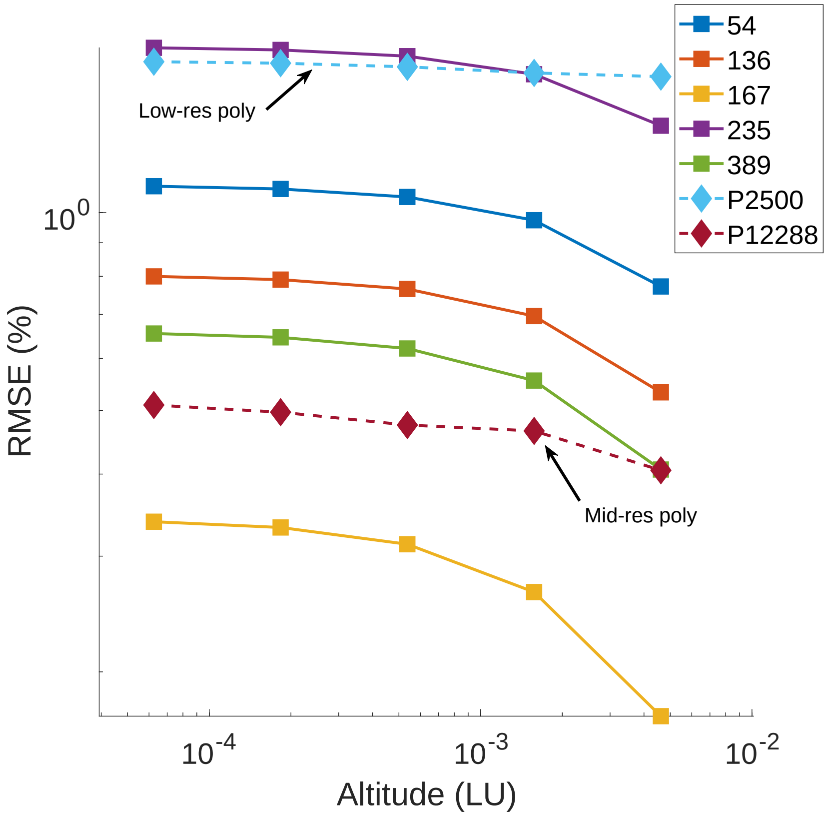

Figure 4.8: RMS acceleration error performance over the first five projected shape model test surfaces for six recommended Pareto-optimal MultiMESH models and two reduced-resolution polyhedral models for Comet 67P (Table 4.4)

(CAESAR)[44]. Sample return missions like CAESAR have a special interest in fast and accurate models of small body gravity fields due to the need to design and optimize landing trajectories near the body surface.

The extreme bilobal shape of 67P presents a particular challenge to efficient and accurate modeling of the low-altitude gravity field. Due to the body's large regions of extreme concavity, conventional spherical or elliptical harmon-

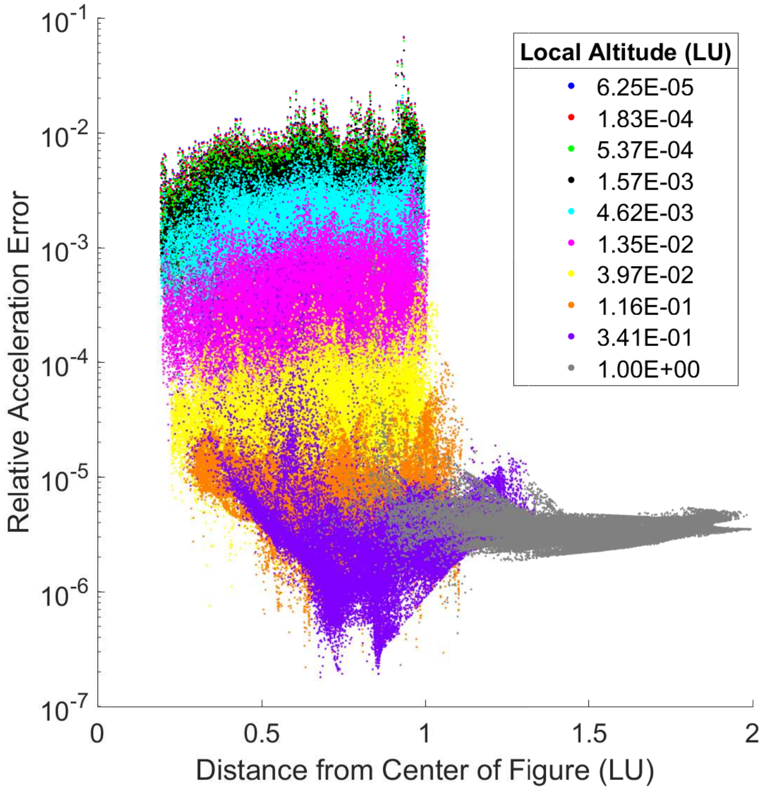

Figure 4.9: Local relative acceleration errors at all exterior test points for Comet 67P/C-G model 167 (class: 2AD; ID: IM1057_00-55r13_SM10000_85). Test points are grouped by the altitude to which they were projected.

ics suffer from divergence issues, while polyhedral models with reduced surface resolutions suffer from degraded relative field errors due to shape distortion. The comet's shape also seems to affect the accuracy of MultiMESH models relative to other, more convex bodies. A comparison with Itokawa is useful here: the two bodies are represented by reference truth polyhedral models of equivalent resolution (49152 facets), the packing parameter set was evaluated

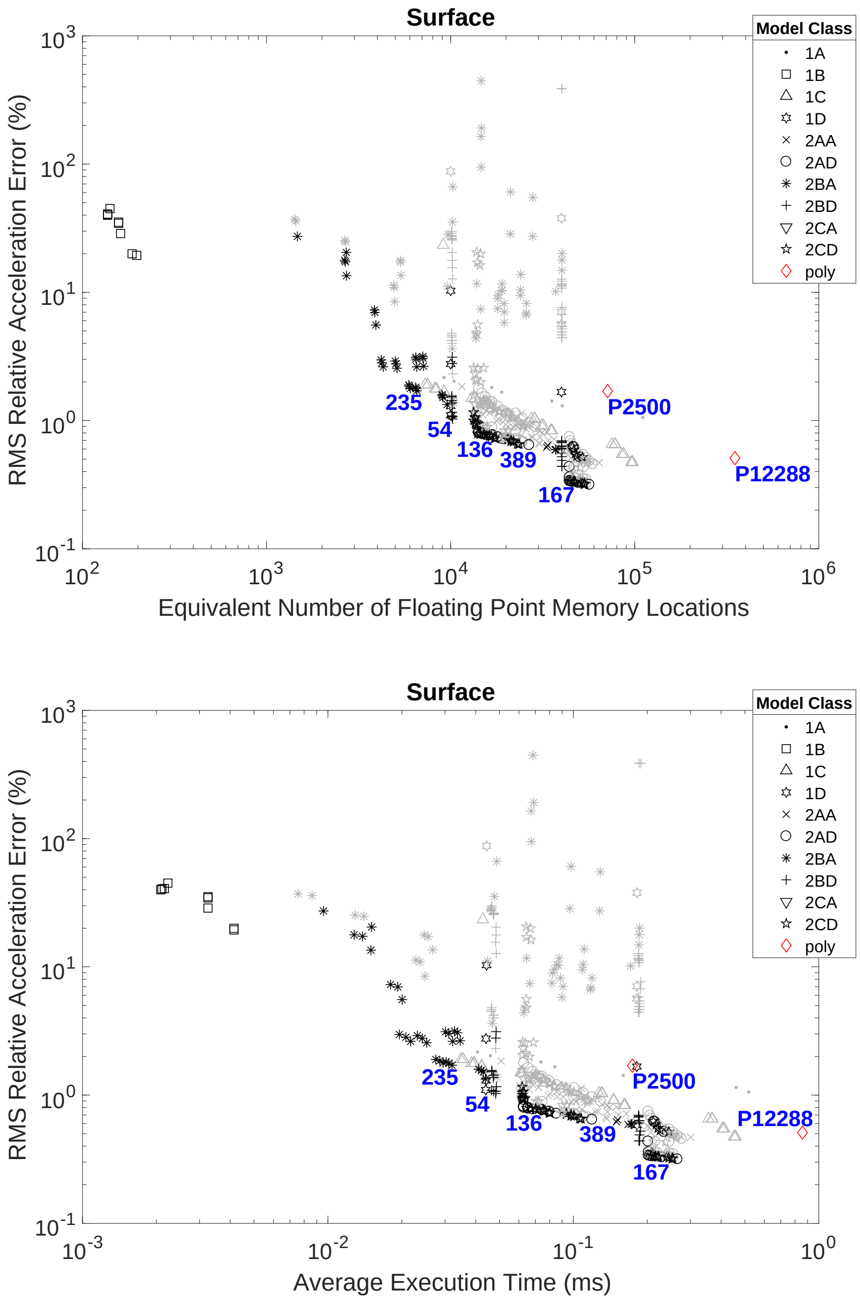

Figure 4.10: 2D Surface performance space projections for all generated Comet 67P models; 4-D Pareto-optimal models are shaded black. Recommended models are labeled with their model numbers.

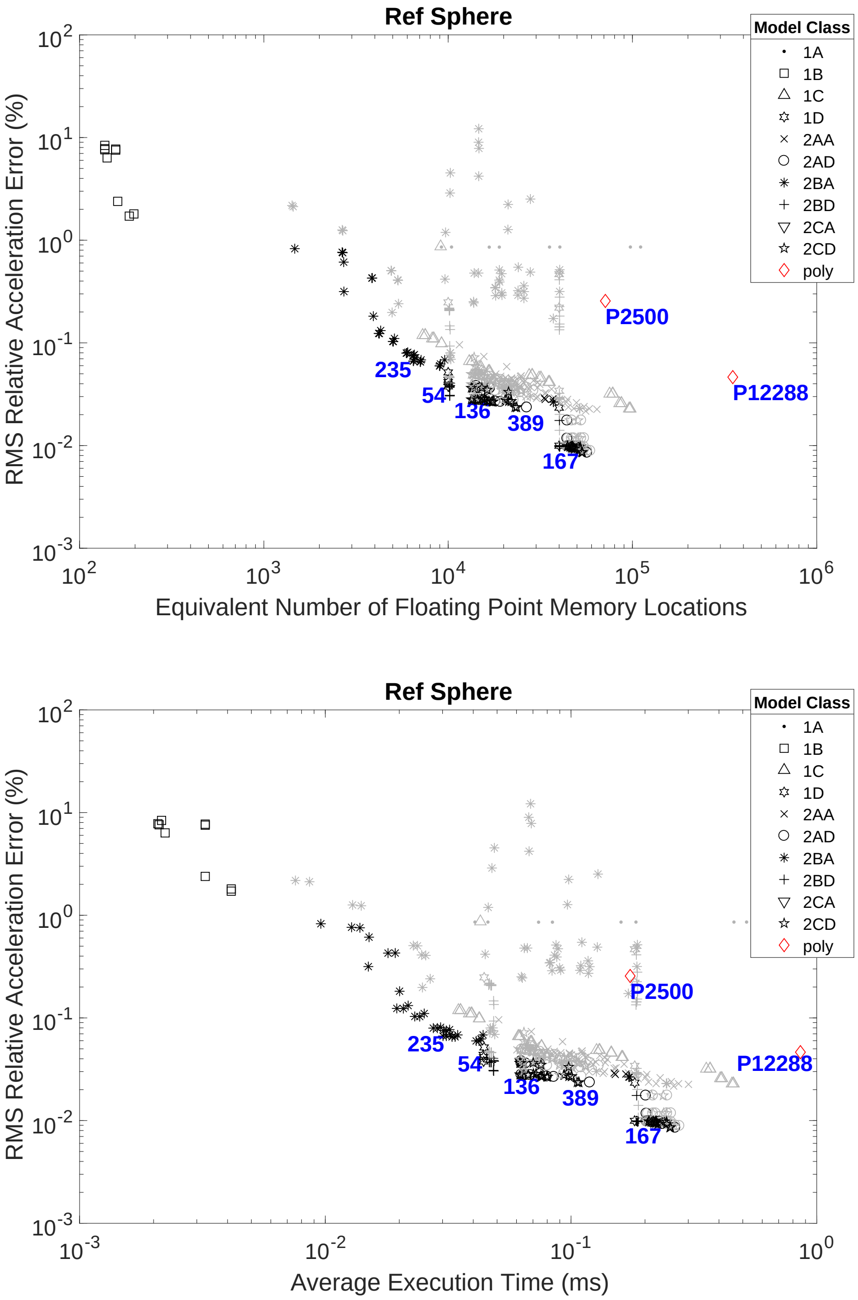

Figure 4.11: 2D Reference sphere performance space projections for all generated Comet 67P models; 4-D Pareto-optimal models are shaded black. Recommended models are labeled with their model numbers.

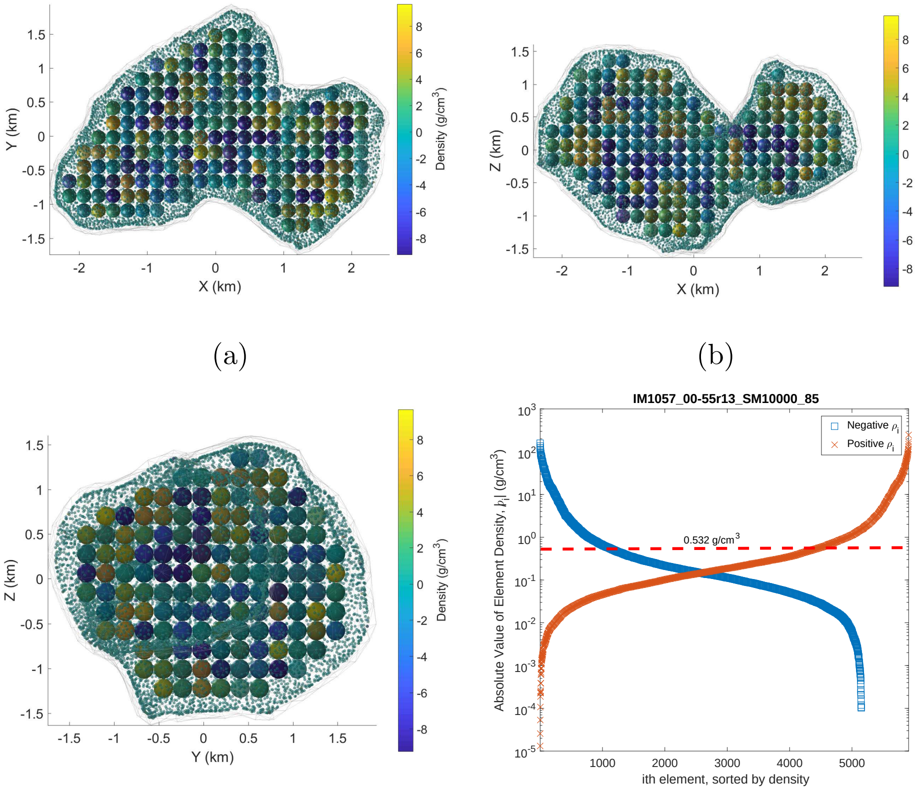

(a) (b)

(c) (d)

Figure 4.12: Element density distribution (a)-(c) and sorted mass element densities (d) for Comet 67P model 167 (class: 2AD; ID: IM1057_00-55r13_SM10000_85). A dotted line indicates the magnitude of the body's bulk density for reference.

at similar values within similar bounds during each grid search, and a common unit normalization scheme was applied to each body during the packing and filtering processes. With the remaining major difference being their shapes, note that about 75% of Itokawa MultiMESH models had surface RMS acceleration errors of less than 1%, while only about 45% of Comet 67P MultiMESH

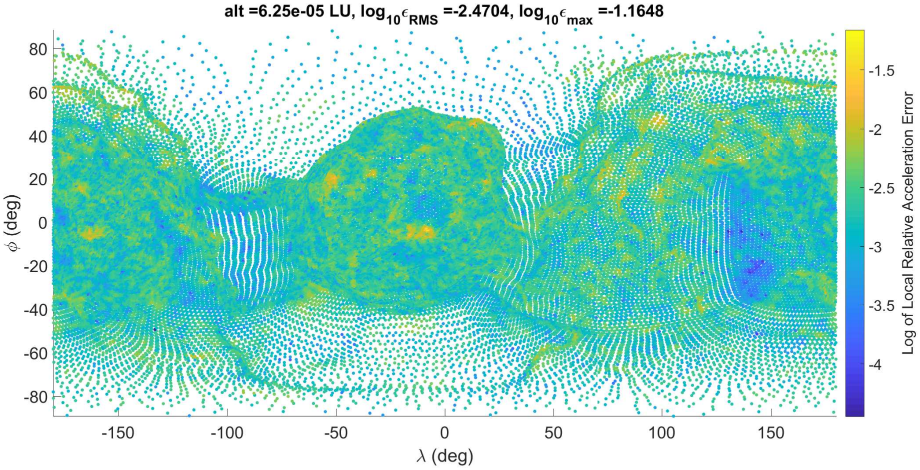

Figure 4.13: Log of local relative acceleration errors at the body surface for Comet 67P/C-G model 167 (class: 2AD; ID: IM1057_00-55r13_SM10000_85)

models fell below the same threshold (Fig. 4.10). Five MultiMESH models that nonetheless offer significant performance advantages are compared with polyhedral alternatives in Table 4.4 and Fig. 4.8. Of particular note are models #235 and #389, which are roughly as accurate as reduced-resolution polyhedral alternatives #437 and #438, respectively, but offer approximately order-of-magnitude computational speedups in comparison.

The comet's extreme concavity also presents a challenge for the selection of performance test points in the context of this work. Whereas for the other two bodies examined here, each evaluation surface exists at a consecutively higher altitude than the last, outwardly-projected shape models using FLPD scaling begin to approach the original shape model surface above a certain value, particularly in the neck region for 67P. The actual inflection point lies at the sixth altitude (0.0135 LU), which is reflected in the presentation of results from only the first five evaluation surfaces in Fig. 4.8.

To present a fuller picture of the near-surface error performance of recommended 67P MultiMESH model #167, local relative acceleration errors are plotted against distance from the origin for each individual test point lying external to the comet (see Fig. 4.9). The points on each evaluation surface are shown with a marks of different colors. Note that local acceleration error rises above 1% only at a small subset of points near the surface, and that mean error levels drop as altitude increases. The internal density distribution and surface acceleration errors for model #167 are shown in Fig. 4.12 and Fig. 4.13. As with Kleopatra, Comet 67P's irregular shape introduces significant distortion to the latitude-longitude plot. The largest acceleration errors are concentrated at the far ends of the body's lobes (located around $\lambda = 0°$ and $\lambda = 180°$), with error values falling below 1% over the bulk of the surface.

4.3.3 25143 Itokawa

Table 4.5: Recommended Pareto-Optimal Models for 25143 Itokawa

#	ID Code	Model Class	Memory Footprint (equiv. fpq)	Avg. Execution Time (ms)	$\epsilon_{\mathrm{RMS,surf}}$ (%)	$\epsilon_{\mathrm{RMS},R_{\mathrm{ref}}}$ (%)
28	IM668_00-75r13_SM2500_85	2AD	12674	5.69E-02	3.88E-01	9.25E-03
217	SH3_00-55_IM1283_55-71r7	2BA	5308	2.55E-02	7.47E-01	2.49E-02
363	SH3_IM2663_00-75r7_SM2500_85	2CD	20830	9.65E-02	3.36E-01	6.60E-03
419	SH2_00-65_SM2500_75	2BD	10110	4.62E-02	4.40E-01	1.20E-02
452	SH3_00-75_SM10000_85	2BD	40178	1.86E-01	1.89E-01	2.63E-03
455	P2500	poly	71272	1.73E-01	8.01E-01	2.63E-01
456	P12288	poly	350230	8.54E-01	3.69E-01	9.37E-02

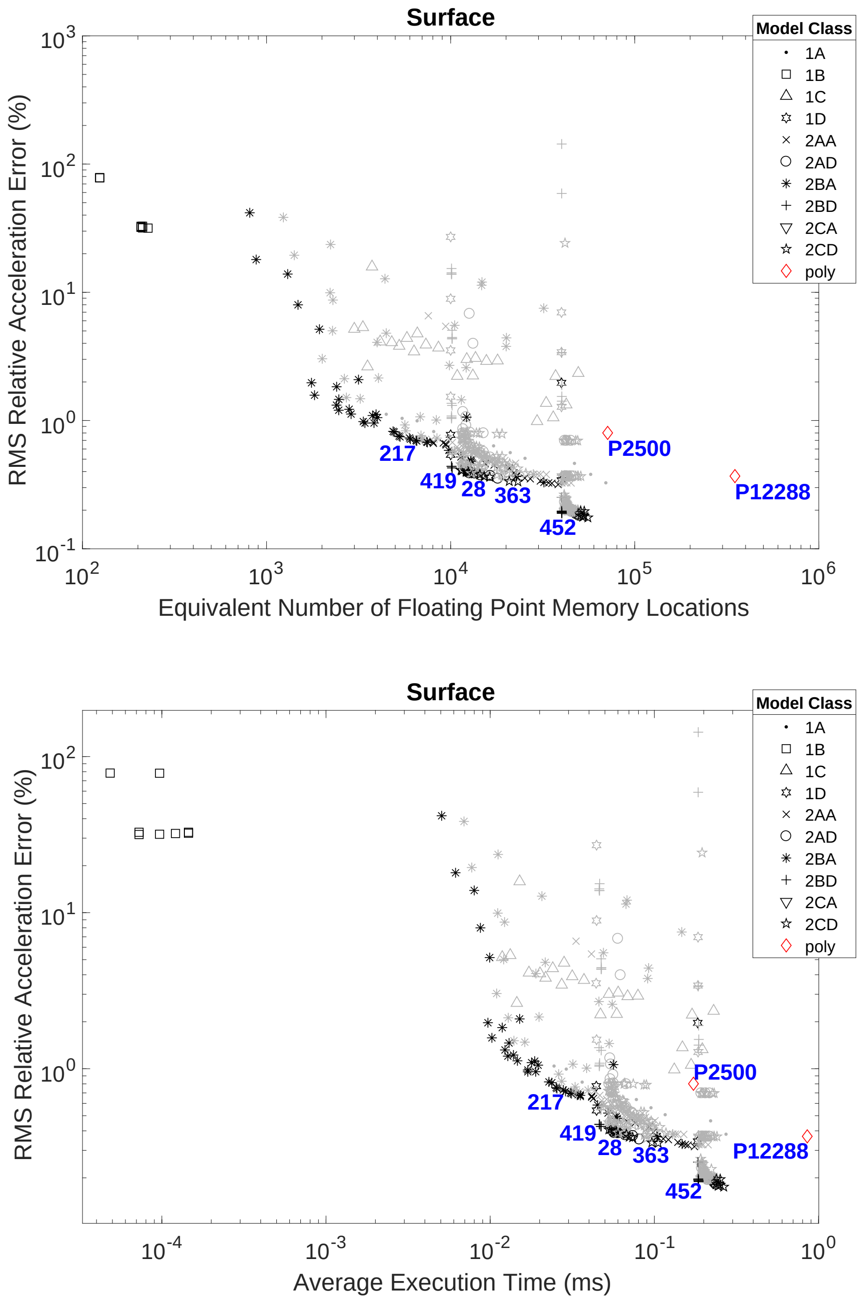

Figure 4.14: 2D Surface performance space projections for all generated 25143 Itokawa; 4-D Pareto-optimal models are shaded black. Recommended models are labeled with their model numbers.

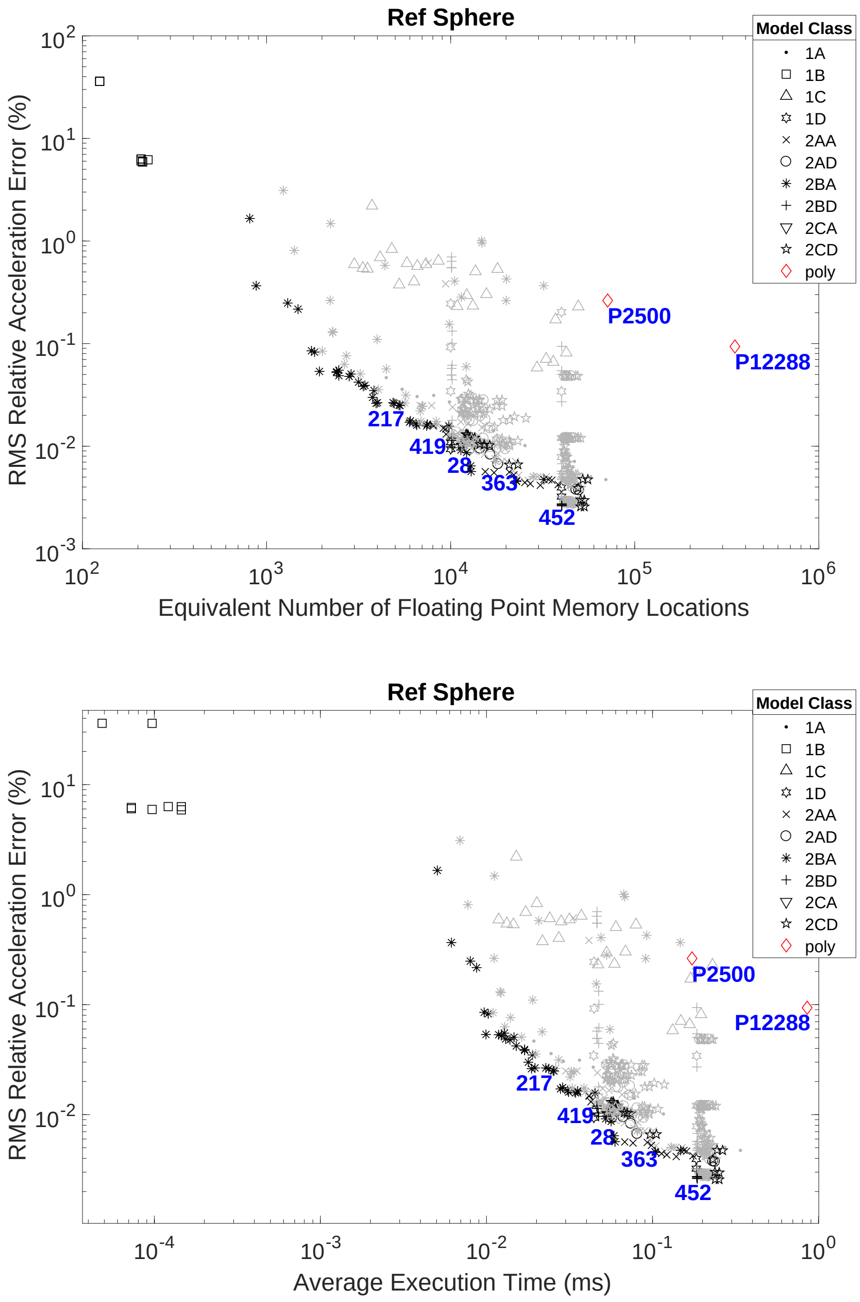

Figure 4.15: 2D Reference sphere performance space projections for all generated 25143 Itokawa; 4-D Pareto-optimal models are shaded black. Recommended models are labeled with their model numbers.

Like Comet 67P, a wealth of data is available for 25143 Itokawa from the Hayabusa mission in the mid-2000s. Unlike Kleopatra, which orbits in the main asteroid belt and is quite massive, Itokawa has a relatively small mass and orbits near the Earth, resulting in the body's gravitational acceleration quickly becoming nondominant relative to solar radiation pressure and third-body effects above the body's surface[1].

Performance results for all Itokawa MultiMESH models are shown in Figs. 4.14 and 4.15. As with the other two bodies, five recommended models are identified and listed with their performance characteristics in Table 4.5. They are compared with two reduced-resolution polyhedral models in the table and in Fig. 4.16. Of particular note are models #217 and #363, which are roughly as accurate as polyhedral alternatives #455 and #456, respectively, but provide roughly order-of-magnitude speedups. As with the other two bodies, the performance benefits of the high-performance MultiMESH models only grow as altitude increases in the near-surface region.

A closer look at the most accurate recommended Itokawa MultiMESH model (#452) is provided in the density distribution plots in Fig. 4.17 and the surface acceleration error map in Fig. 4.18. With a core-shell structure, model #452 has a distinct configuration relative to the other two models pictured in this work. Element densities generally fall within about an order of magnitude of the body's bulk density, but there are more negative than positive masses present in the model. Surface-level acceleration errors are remarkably consistent for this model, with spikes located in a few small regions and errors below 1% otherwise.

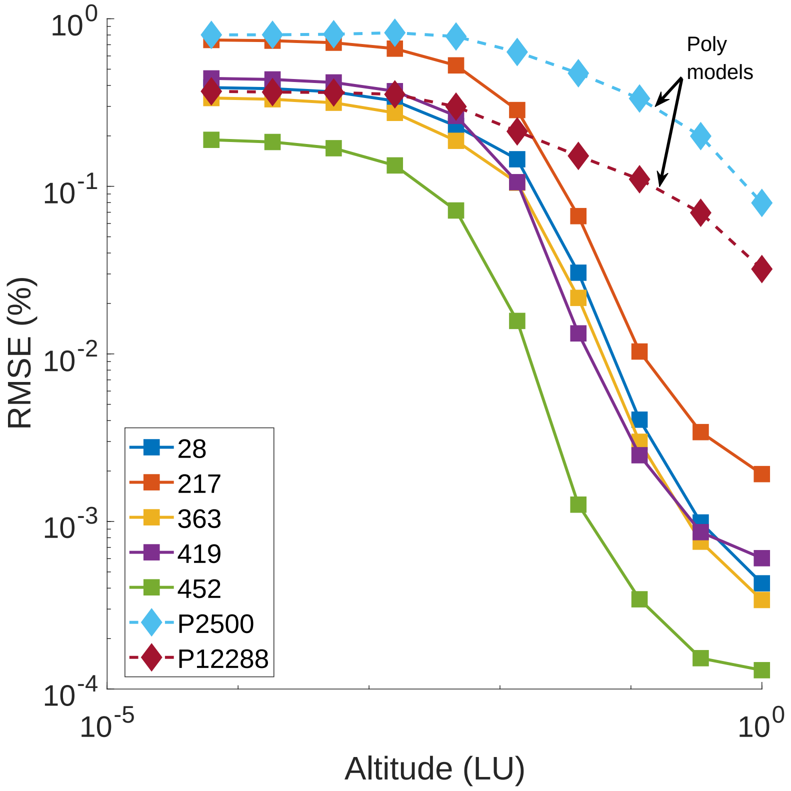

Figure 4.16: RMS acceleration error performance over the ten projected shape model test surfaces for five recommended Pareto-optimal MultiMESH models and two reduced-resolution polyhedral models for 25143 Itokawa (Table 4.5)

4.4 Discussion

First, we note once again that no code parallelization techniques were applied to the performance test; applying one or more techniques (OpenMP, GPU, etc.) would likely result in even greater computational speedups. Efficiency gains obtained from parallelization would be in absolute rather than

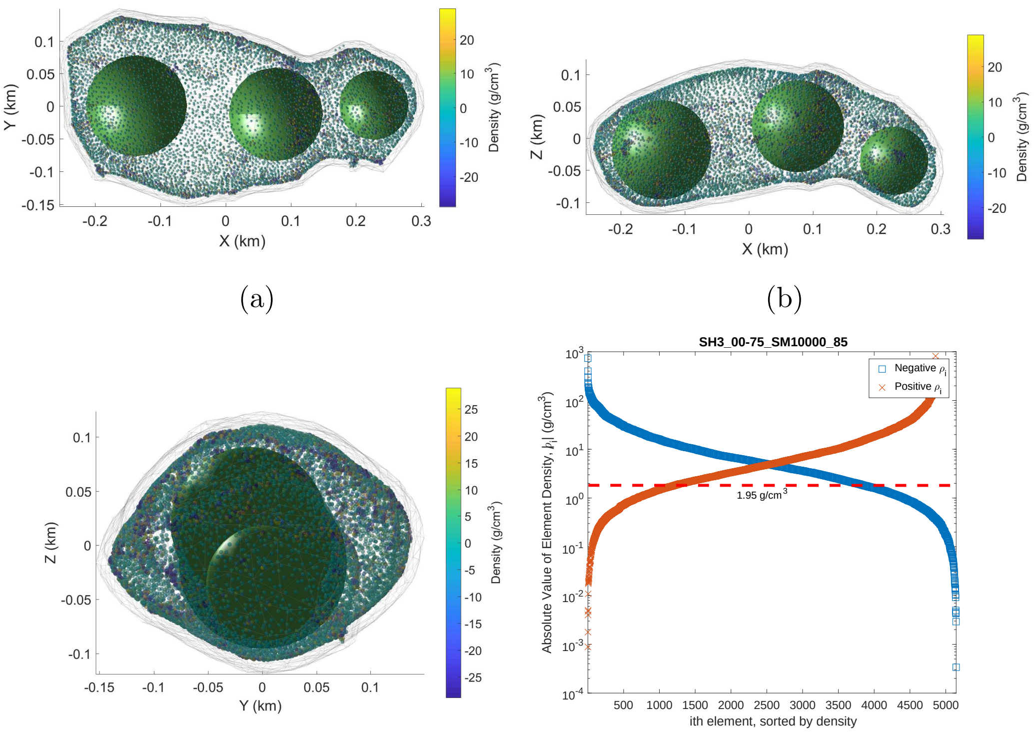

(a) (b)

(c) (d)

Figure 4.17: Element density distribution (a)-(c) and sorted mass element densities (d) for Itokawa model 452 (class: 2CD; ID: SH3_00-75_SM10000_85). A dotted line indicates the magnitude of the body's bulk density for reference.

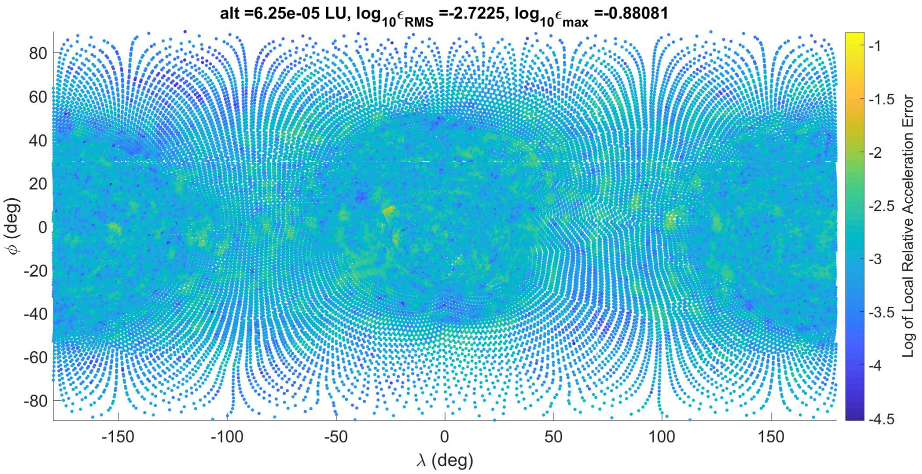

Figure 4.18: Local relative acceleration errors at the body surface for Itokawa model 452 (class: 2CD; ID: SH3_00-75_SM10000_85)

relative terms, however, as polyhedral models can also be accelerated with parallel implementation. Also, many of the best-performing MultiMESH models (including 13/15 recommended models) contain an outer shell layer of mascons. In combination with FLPD scaling techniques and advantageous lateral mascon spacing based on shape model facet geometry, shell mascon layers exhibit relatively consistent errors across the body surface. Sharp troughs or peaks in the surface acceleration error profile that may distort RMS values are thereby avoided. Consistent, low error levels across the body surface also suggest that such models may be ideal for designing landing trajectories. Trade studies for a set of candidate landing sites could be conducted using a single efficient and accurate force model instead of a global, high-fidelity polyhedral model or any number of multi-fidelity models designed for use at a particular landing site.

Additionally, performance results from models in the 1D, 2AD, 2BD, and 2CD classes (i. e. models with shell layers) support the existence of optimal mascon shell layer burial depths that depend on shell element spacing, inner layer characteristics, and the body in question. Models in these classes result in the vertical striations in Figs. 4.3, 4.4, 4.11, 4.10, 4.14 and 4.15 since a single family of these models contains the exact same number of elements and differs only in the burial depth of the mascon shell. Each such family has a member with a shell layer burial depth that minimizes the gravitational acceleration error at a given altitude (and often over multiple altitudes) with respect to the rest of the family. Some of these are Pareto-optimal, and their optimal shell depths vary depending on their internal structure (e. g. models 54, 136, and 389 for Comet 67P). It is expected that fine grid searches for models in these classes could serve to minimize field errors beyond what is given in this work by tuning the shell layer burial depth for any given model structure. Work on a similar concept for the Earth has been performed previously by Russell and Arora[58].

All of the recommended models listed in Tables 4.3, 4.4, and 4.5 offer memory and speed advantages relative to the polyhedral truth models to which they were fitted. When compared to reduced-resolution polyhedral models of near-peer surface fidelity, recommended MultiMESH models tend to be both significantly faster to evaluate and equally or more accurate at higher altitudes. Some of the hybrid models' execution times are about an order of magnitude less than those of the polyhedral peers.

The implications of such efficiency gains in the context of trajectory computation (for orbit determination, mission design, or GNC applications) are significant. For an application that requires 10^6 field evaluations, the total computation time spent evaluating the gravitational force using a polyhedral truth model for a single orbit could be as much as an hour on a single CPU.

4.5 Conclusion

In this chapter, several high-performance hybrid mascon and spherical harmonics-based models are identified for the small celestial bodies 216 Kleopatra, Comet 67P/Churyumov-Geraskimenko, and 25143 Itokawa via grid search explorations of the shape model packing parameter design space and a Pareto-sorting of the resulting model sets using speed, memory, and accuracy performance metrics. A new shape model scaling method is also introduced to regulate and optimize the burial depth of packed mascons. Resulting Pareto-optimal models benefit from the memory-efficiency of spherical harmonics and the speed of point mascon evaluations, while retaining much of the accuracy and global domain validity of polyhedral gravity fields. Recommended subsets of Pareto-optimal hybrid models offer up to order of magnitude computational speed-ups over polyhedral models of equivalent accuracy. Such advances benefit mission design and GNC efforts within the scope of small body mission engineering. The hybrid gravity models built and identified in this chapter have been archived and made publicly available, alongside driver routines for their evaluation.

Chapter 5

Mascon Models for Estimating Heterogeneous Small Body Density Distributions

5.1 Introduction

Before a spacecraft rendezvous with a primitive body, the state-of-the-art representation of the body density distribution and near-surface gravity field is the homogeneous polyhedron [79]. Chapters 3 and 4 of the current work developed efficient hybrid proxy models for the homogeneous polyhedral gravity field using discrete elements, but such models are not representative of the true field if any heterogeneities exist in the body density distribution. Information about density heterogeneities can, however, be captured in spacecraft radiometric data. Radiometric data can be used to estimate gravity field models, including mascon models[49] and spherical harmonics [30, 71] models. Since spacecraft typically orbit and collect data at high altitudes during small body missions, spherical harmonic models are commonly estimated to provide relatively fast gravity field representations[22, 33]. Spacecraft data collected in low-altitude regions where spherical harmonics are invalid would be valuable input for the estimation of higher-fidelity mascon models (or other proxy models valid at low altitudes). In the absence of such data, proxy models for the primitive body density distribution and gravity field should ideally leverage the information present in the mission-derived gravity field. Although the series representation only converges outside the circumscribing sphere, the estimated coefficients do not rely on assumptions about the density distribution and express the gravity field resulting from the true primitive body mass distribution, albeit with significant uncertainty in the small body case.

Several previous works have leveraged the information present in the OD-derived spherical harmonics field to estimate internal density heterogeneities within a polyhedral shape model. Hesar, et al. [24] used both exterior and interior spherical harmonics expansions to estimate the mass and location of a spherical density anomaly within a homogeneous polyhedron. Scheeres, et al. [62] discretized the polyhedral shape model into tetrahedra emanating from the center-of-figure and estimated their densities by fitting to a set of reference spherical harmonic coefficients. Takahashi and Scheeres [69] modified that approach by applying a constraint on the total mass and adopting a morphology-driven approach to the polyhedral subdivision. Both of the latter approaches apply a modified version of the polyhedral gravity field and assume convexity in the body shape to facilitate the tetrahedral subdivision. They also take advantage of the direct relationship between a polyhedron of known density and its set of spherical harmonic coefficients, presented by Werner [78]. Another relevant result of the above works is that an accurate estimation of the internal density distribution is reliant upon the selection of an accurate density map; that is, how the continuous mass of the polyhedron is divided into regions of internally homogeneous density.

In this chapter the methods of Takahashi and Scheeres [69] are extended to estimate small body density distributions in a mascon framework using the coefficients of a reference spherical harmonics field as measurements. The current approach permits modification of the mascon configuration using flexible, layered packing techniques for polydisperse finite spherical masconsas introduced in Chapter 3. The mascons are divided into regions of internally common density based on typical small body morphologies, and a constrained least-squares problem minimizing the difference between the reference and total mascon coefficients is solved for the vector of regional mascon densities. A homogeneous *a priori* density distribution is shown to enable solutions with entirely positive-valued mascon densities. The resulting model solutions provide both estimates of internal density distributions and fast, near-surface gravity field representations that are statistcally consistent with the reference spherical harmonics field.

This chapter is organized as follows: The next section discusses the expression of a mascon gravitational potential in a spherical harmonics framework. The following section develops the cost function, constraints, and solution for the regional mascon density estimation problem. Then, the method is validated by recovering a heterogeneous mascon model using various mascon configurations. Finally, the method is applied to Comet 67P/Churyumov-Gerasimenko using as measurements the OD-derived spherical harmonic coefficients for the body from the Rosetta mission. The mascon model configuration is optimized via a grid search of the configuration design space, and the model solutions are evaluated for the quality of their coefficient fit and the statistical consistency of their gravity field representations.

5.2 Spherical Harmonic Potential of a Point-Mass Distribution

Point-mass concentrations (mascons) and constant density finite spheres have simple external gravity signatures ($U = \mu/r$) when considered individually. When these mass elements exist in the context of a proxy for a realistic, continuously varying mass distribution, it is useful to express their potential in a spherical harmonics framework for a variety of geodetic and field modeling applications. The classical Legendre form of the spherical harmonic potential[30] for a body with mass M is

$$U = \frac{GM}{r} \sum_{n=0}^{\infty} \sum_{m=0}^{n} \left(\frac{R_{\text{ref}}}{r} \right)^n \bar{P}_{nm}(\sin\phi)[\bar{C}_{nm} \cos m\lambda + \bar{S}_{nm} \sin m\lambda] \tag{5.1}$$

where $\bar{P}_{nm}$ are the fully normalized associated Legendre polynomials and the coefficients $\bar{C}_{nm}$ and $\bar{S}_{nm}$ are the normalized Stokes' coefficients. Equation 5.1 is expressed in spherical coordinates (r, ϕ, λ), representing the radial distance, latitude, and longitude of the field point, respectively. The reference radius R_{ref} may be chosen arbitrarily, but is typically chosen to equal the radius of the sphere that bounds the mass distribution. A useful alternative form of the spherical harmonics potential separates the zeroth degree term from the summation:

$$U = \frac{GM}{r} + \frac{GM}{R_{\text{ref}}} \sum_{n=1}^{\infty} \sum_{m=0}^{n} \left(\frac{R_{\text{ref}}}{r}\right)^{n+1} \bar{P}_{nm}(\sin\phi)[\bar{C}_{nm}\cos m\lambda + \bar{S}_{nm}\sin m\lambda] \quad (5.2)$$

For a known mass distribution, the Stokes coefficients can be computed explicitly via the integrals[61]:

$$\begin{bmatrix} \bar{C}_{nm} \\ \bar{S}_{nm} \end{bmatrix} = \frac{1}{2n+1}\left(\frac{1}{M}\right) \int_{\mathcal{B}} \left(\frac{r}{R_{\text{ref}}}\right)^{n} \bar{P}_{nm}(\sin\phi) \begin{bmatrix} \cos m\lambda \\ \sin m\lambda \end{bmatrix} \rho(r,\phi,\lambda)\, dV \quad (5.3)$$

where n and m denote the degree and order of the coefficients, respectively, M is the total mass of the body, R_{ref} is an arbitrary reference radius, and $\rho(r,\phi,\lambda)$ is the density of the differential mass element located at radius r, latitude ϕ, and longitude λ. Note that the fully normalized coefficients are defined here, and are exclusively used in their normalized forms throughout the current work.

Pollack[56] and Sutton, et al.[67] derive expressions for the spherical harmonic coefficients of point masses (and several distributed mass elements) located on the surface or within a bounding sphere, respectively. Of relevance to the small celestial body mascon modeling approach is the subsurface case, in which there exist L discrete mass elements. Assuming each discrete mass element is a finite sphere of known density ρ_k and volume V_k, and no evaluations of the potential are performed within such sphere, a modified version of Sutton, et al.'s expression for the normalized spherical harmonic coefficients of a buried point mass gives the coefficients for the kth mass element:

$$\begin{bmatrix}\bar{C}^k_{nm}\\ \bar{S}^k_{nm}\end{bmatrix} = \frac{1}{2n+1}\left(\frac{r_k}{R_{\text{ref}}}\right)^n \left(\frac{\rho_k V_k}{M}\right)\bar{P}_{nm}(\sin\phi_k)\begin{bmatrix}\cos m\lambda_k\\ \sin m\lambda_k\end{bmatrix} \tag{5.4}$$

where M is the total mass of the L mascons, and the kth mascon is located at distance r_k, latitude ϕ_k, and longitude λ_k relative to the origin. No approximation is made to obtain this expression: Eq. 5.4 is exactly equivalent to the integral in Eq. 5.3 for the case of a single point-mass or constant-density sphere located within the reference sphere with radius R_{ref}.The total spherical harmonic coefficients $\bar{C}_{nm}$ and $\bar{S}_{nm}$ of the mascon distribution are then given by the summation

$$\begin{bmatrix}\bar{C}_{nm}\\ \bar{S}_{nm}\end{bmatrix} = \sum_{k=1}^{L}\begin{bmatrix}\bar{C}^k_{nm}\\ \bar{S}^k_{nm}\end{bmatrix}. \tag{5.5}$$

The coefficients in Eq. 5.5 are substituted into Eq. 5.1 or 5.2 to find the gravitational potential of a mascon distribution external to the sphere at the origin with radius R_{ref}.

Now suppose that the mascon distribution contains N_R groups (or regions) of mascons, each having a collective mass M_i such that $M = \sum_{i=1}^{N_R} M_i$ and internally homogeneous density such that $M_i = \rho_i V_i$, and V_i is the total volume enclosed by the mascons in each region. The system total potential is expressed via a superposition of potentials in the form of Eq. 5.1:

$$U_{MC} = \sum_{i=1}^{N_R}\frac{G\rho_i V_i}{r}\sum_{n=0}^{\infty}\sum_{m=0}^{n}\left(\frac{R_{\text{ref}}}{r}\right)^n \bar{P}_{nm}(\sin\phi)[\bar{C}^i_{nm}\cos m\lambda + \bar{S}^i_{nm}\sin m\lambda] \tag{5.6}$$

The regional coefficients $\bar{C}^i_{nm}$ and $\bar{S}^i_{nm}$ encode information about the distribution of mass for the ith mascon region and are calculated using Eq. 5.5 for each ith region containing L_i mascons. By changing the order of summation in Eq. 5.6 and scaling by M/M, the total mascon potential can be expressed as

$$U_{MC} = \frac{GM}{r}\Big\{\frac{1}{M}\sum_{i=1}^{N_R}\rho_i V_i\Big\} + \frac{GM}{R_{\text{ref}}}\sum_{n=1}^{\infty}\sum_{m=0}^{n}\Bigg\{\Big(\frac{R_{\text{ref}}}{r}\Big)^{n+1}\bar{P}_{nm}(\sin\phi)\begin{bmatrix}\cos m\lambda_k\\ \sin m\lambda_k\end{bmatrix} \cdot\Big\{\frac{1}{M}\sum_{i=1}^{N_R}\rho_i V_i\begin{bmatrix}\bar{C}^i_{nm}\\ \bar{S}^i_{nm}\end{bmatrix}\Big\}\Bigg\}. \tag{5.7}$$

5.3 Estimation of Regional Mascon Densities

The following derivation proceeds similarly to that of Takahashi and Scheeres[69], with the exception of the addition of a prior density distribution estimate. Note also that, although the following algorithm seeks a solution for the density given a particular gravity field, the relationship between them is not one-to-one. A given external gravity field could result from a theoretically infinite number of mass distibutions. Hence, the solutions developed are unique for a given mascon configuration, not for the body in general.

5.3.1 Estimation Algorithm

For the total mascon potential in Eq. 5.7 to equal a reference potential in the form of Eq. 5.2, the following necessary conditions must be satisfied:

$$1 = \frac{1}{M} \sum_{i=1}^{N_R} \rho_i V_i \tag{5.8}$$

$$\begin{bmatrix} \bar{C}_{nm} \\ \bar{S}_{nm} \end{bmatrix} = \frac{1}{M} \sum_{i=1}^{N_R} \rho_i V_i \begin{bmatrix} \bar{C}^i_{nm} \\ \bar{S}^i_{nm} \end{bmatrix} \tag{5.9}$$

Equation 5.8 is a constraint on the total mass, and Eq. 5.9 constrains the values of all harmonic coefficients above zeroth order. Both constraints are linear functions of the regional density vector, and the summations can be rewritten as vector inner products. Rearranging and normalizing the total mass constraint yields

$$0 = \frac{M - [V_i][\rho_i]}{M} \tag{5.10}$$

Both $[V_i]$ and $[\rho_i]$ are vectors of length N_R. We can also scale by G to express the constraint in terms of the primitive body gravitational parameter $\mu = GM$:

$$0 = \frac{\mu - [V_i][\sigma_i]}{\mu} \tag{5.11}$$

where $[\sigma_i] = G[\rho_i]$. For the coefficient constraint, it is useful to express the vector of reference coefficients as $[\bar{T}_{lnm}]$ such that $[\bar{T}_{0nm}] = [\bar{C}_{nm}]$ and $[\bar{T}_{1nm}] = [\bar{S}_{nm}]$. Then, by converting Eq. 5.9 to inner product form and once again scaling by G, the coefficient constraint becomes

$$[\bar{T}_{lnm}] = \left[\frac{V_i}{\mu}\bar{\tau}^i_{lnm}\right]^T [\sigma_i] \tag{5.12}$$

where $[\bar{\tau}^i_{lnm}]$ are the coefficients for the ith region. The reference coefficients are denoted $[\bar{T}^{OD}_{lnm}]$ from this point forward to reflect that they would typically be estimated during orbit determination in a realistic use-case.

Since the problem objective is to match the mascon potential with the reference potential, the coefficient matching condition and mass constraint can be assembled in a least-squares cost function J_0:

$$J_0 = \frac{1}{2}\Big(\Big[\frac{V_i}{\mu}\bar{\tau}^i_{lnm}\Big]^T [\sigma_i] - [\bar{T}^{OD}_{lnm}]\Big)^T \mathbf{P}_c^{-1}\Big(\Big[\frac{V_i}{\mu}\bar{\tau}^i_{lnm}\Big]^T [\sigma_i] - [\bar{T}^{OD}_{lnm}]\Big) + \lambda\Big(\frac{\mu - [V_i]^T[\sigma_i]}{\mu}\Big) \tag{5.13}$$

where $\mathbf{P}_c^{-1}$ is a weighting matrix that could contain the inverse covariance matrix for the reference coefficients obtained from orbit determination. Cost function J_0 minimizes the difference between the total mascon coefficients and the reference coefficients, and places a hard constraint on the total mascon model mass to equal the primitive body mass. This formulation for the cost function does not exclude density solution vectors with negative values for some regions. While an accurate mathematical gravity field model does not require an all-positive density distribution, physical density models do. Identification of such solutions can be facilitated through the addition and tuned weighting of an *a priori* density distribution term to J_0. Given an *a priori* regional density vector $[\bar{\sigma}_i]$ and associated weighting matrix $\mathbf{P}_{\sigma\sigma}^{-1}$, the total cost is

$$J = J_0 + \frac{1}{2}\Big([\sigma_i] - [\bar{\sigma}_i]\Big)^T \mathbf{P}_{\sigma\sigma}^{-1}\Big([\sigma_i] - [\bar{\sigma}_i]\Big) \tag{5.14}$$

To find the first order necessary conditions for a minimum, take the first partial derivative of J with respect to $[\sigma_i]$ and set to zero:

$$\frac{\partial J}{\partial[\sigma_i]} = \Big(\Big[\frac{V_i}{\mu}\bar{\tau}^i_{lnm}\Big]^T[\sigma_i] - [\bar{T}^{OD}_{lnm}]\Big)^T \mathbf{P}_c^{-1}\Big[\frac{V_i}{\mu}\bar{\tau}^i_{lnm}\Big] + \Big([\sigma_i] - [\bar{\sigma}_i]\Big)^T \mathbf{P}_{\sigma\sigma}^{-1} - \frac{\lambda}{\mu}[V_i]^T = 0 \tag{5.15}$$

After rearranging and distributing, Eq. 5.15 reduces to:

$$\mathbf{\Lambda}[\sigma_i] = [N] + [C] \tag{5.16}$$

where the information matrix $\mathbf{\Lambda}$, normal vector $[N]$, and constraint vector $[C]$ are

$$\mathbf{\Lambda} = \Big[\frac{V_i}{\mu}\bar{\tau}^i_{lnm}\Big]^T \mathbf{P}_c^{-1}\Big[\frac{V_i}{\mu}\bar{\tau}^i_{lnm}\Big] + \mathbf{P}_{\sigma\sigma}^{-1}$$

$$[N] = \Big[\frac{V_i}{\mu}\bar{\tau}^i_{lnm}\Big]^T \mathbf{P}_c^{-1}[\bar{T}^{OD}_{lnm}] + \mathbf{P}_{\sigma\sigma}^{-1}[\bar{\sigma}_i]$$

$$[C] = \frac{\lambda}{\mu}[V_i]$$

Calculating the final estimate requires a value for λ, which can be found by substituting the solution for $[\sigma_i]$ in Eq. 5.16 into the constraint equation (Eq. 5.11). After rearranging and an explicit solution for λ is obtained:

$$\lambda = \frac{\mu}{[V_i]^T \mathbf{\Lambda}^{-1} [V_i]} (\mu - [V_i]^T \mathbf{\Lambda}^{-1} [N]) \tag{5.17}$$

Finally, the unconstrained solution $[\tilde{\sigma}_i]$ and the constrained solution $[\sigma_i]$ can be assembled:

$$[\tilde{\sigma}_i] = \mathbf{\Lambda}^{-1} [N] \tag{5.18}$$

$$[\sigma_i] = [\tilde{\sigma}_i] + \mathbf{\Lambda}^{-1} \Big(\frac{\lambda}{\mu} [V_i] \Big) \tag{5.19}$$

5.3.2 Quantifying Model Performance

The preceding algorithm obtains a unique solution for a particular mascon configuration given a reference spherical harmonics gravity field. To judge the accuracy of the estimate relative to the reference, several tools are available. The first is examination of the postfit coefficient residuals:

$$\begin{bmatrix} \Delta \bar{C}_{nm} \\ \Delta \bar{S}_{nm} \end{bmatrix} = \begin{bmatrix} |\bar{C}_{nm}^{OD} - \bar{C}_{nm}^{MC}| \\ |\bar{S}_{nm}^{OD} - \bar{S}_{nm}^{MC}| \end{bmatrix} \tag{5.20}$$

The residuals can be condensed to examine the fit relative to the reference model with the degree error variance:

$$\Delta\sigma_n = \sum_{m=1}^{n} \left[(\Delta\bar{C}_{nm})^2 + (\Delta\bar{S}_{nm})^2\right] \Big/ \sum_{m=1}^{n} \left[(\bar{C}_{nm}^{OD})^2 + (\bar{S}_{nm}^{OD})^2\right] \tag{5.21}$$

The degree error variance expresses an aggregate of the coefficient errors across the same degree relative to the magnitude of the reference coefficients of the same degree. The denominator of Eq. 5.21 can be calculated for any spherical harmonics series, and is known as the degree variance. The degree error variance and the degree variance are defined equivalently in Takahashi and Scheeres[69].

Also of interest is how the errors in the estimated coefficients manifest in errors in the modeled gravity field. Root-mean-square (RMS) relative acceleration errors are measured on the surface of a sphere that circumscribes the mass distribution. Given N_{meas} evaluations, the total RMS relative acceleration error is:

$$\text{RMS}\Big(\frac{\Delta\ddot{\mathbf{r}}}{|\ddot{\mathbf{r}}_{OD}|}\Big) = \sqrt{\frac{1}{N_{\text{meas}}} \sum_{i=1}^{N_{\text{meas}}} \left(\frac{\ddot{\mathbf{r}}_{OD} - \ddot{\mathbf{r}}_{MC}}{|\ddot{\mathbf{r}}_{OD}|}\right)^2} \tag{5.22}$$

5.4 Regional Mascon Models

The methods used in this chapter to divide mascon models into regions of internally constant density are now detailed. Their impact, as well as the impact of other model inputs, on the quality of the least-squares fit is also explored in order to inform the case study conducted in later sections for

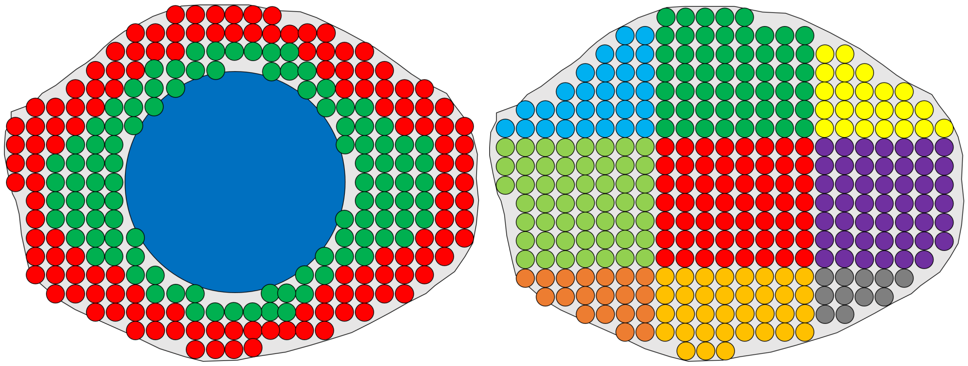

(a) Division by Layer w/ Separate Cores

(b) Division by Cartesian Grid

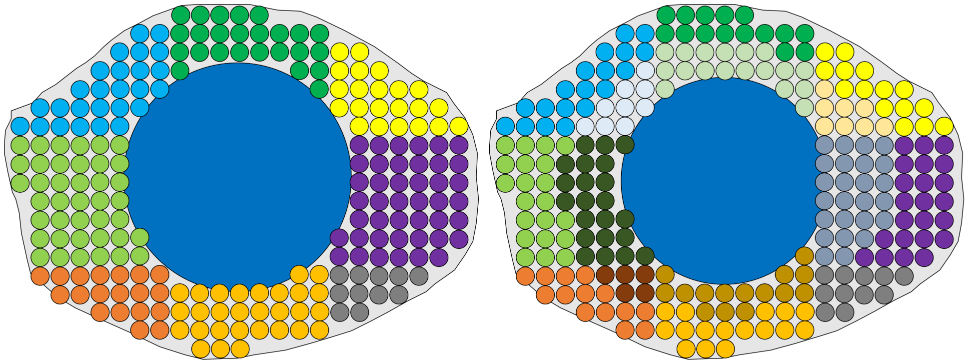

(c) Division by Cartesian Grid w/ Separate Cores

(d) Division by Cartesian Grid and Layers w/ Separate Cores

Figure 5.1: 2D Illustration of Mascon Region Division Methods

Comet 67P/Churyumov-Gerasimenko.

5.4.1 Observability of Regional Densities

The number of mascon density regions is limited by the size of the reference spherical harmonics field. To avoid the underdetermined case and ensure a unique solution for each mascon region configuration, the number of regions is limited to be less than the number of coefficients in $\bar{T}_{lnm}^{OD}$ (i.e.

$N_R < n_{\max}(n_{\max} + 2)$). The zeroth-degree and -order coefficient is excluded from $\bar{T}^{OD}_{lnm}$ since it is already constrained by Eq. 5.11. The small size of existing small body gravity fields derived from mission data implies an upper limit of tens to hundreds of mascon regions. Since mascon models typically contain hundreds to thousands of mascons, most models require the grouping of mascons into a sufficiently small number of regions of internally constant density.

Although the limit on the region count avoids an underdetermined problem, it does not avoid the well-known ill-conditioning of the gravity inversion. As will be shown in the next section, the condition number of the estimation problem increases with additional degrees of freedom in the choice of configuration. Hence there is an unavoidable conundrum in the design of the regional configuration: high resolution configurations with nearly as many regions as reference coefficients have poor observability for the regional densities, while models with few regions have highly observable density vectors with insufficient degrees of freedom to fit the measurements.

5.4.2 Regional Division Methods

The division of mascon models into regions is theoretically arbitrary. Any geometric discretization of the internal volume of the primitive body that results in fewer regions than coefficients will support a unique density solution, but the density vector observability decreases as the number of regions approaches the number of coefficients. This work makes use of four division methods, the first two of which are combined to produce the latter two. The four methods are: (1) division by packing layer with separate cores; (2) division by Cartesian grid; (3) division by Cartesian grid with separate cores, and; (4) division by Cartesian grid and layers with separate cores. Figure 5.1 depicts conceptual illustrations of the regional division methods, with regions shaded uniquely.

The first regional division method, division by packing layer with separate cores, results intuitively from the mascon packing procedure itself. The previously introduced layered packing approach places mascons within scaled polyhedral shape models, allowing for the construction of polydisperse discrete element models that are informed and shaped by the primitive body morphology. Certain mass elements, referred to here as "cores", have radii greater than 12.5% of the body's circumscribing radius, and are generally placed within the largest available spaces inside a scaled shape model. The first regional division method simply considers mascons placed in separate layers, and all cores, as separate regions (see Fig. 5.1a).

The second division method simply separates the mascons into regions based on their location within a user-defined Cartesian grid (Fig. 5.1b). The number of grid blocks is prespecified in each coordinate direction, allowing for variable grid resolutions depending on the degree and order of the reference gravity field. The third method is identical to the second, with the exception that any cores are considered separate regions (Fig. 5.1c). The fourth method is a superposition of the first and second methods, using both layer and grid boundaries to separate the mascons into regions, while also separating core elements into their own regions (Fig. 5.1d).

Finally, note that mascon regions divided on a Cartesian grid will take different shapes depending on the relative orientation of the body shape model to the underlying coordinate system. For a bilobal body like Comet 67P/C-G, it is desirable that a Cartesian division scheme would divide the body along the contact boundary to explore solutions consistent with a contact binary[27]. The coordinate system for the shape model and gravity solution in this work is rotated approximately -35 degrees about the z-axis from the plane of contact between the two lobes of Comet 67P/C-G. Hence, for all gridded region divisions from this point forward in this work, the mascon model is rotated 35 degrees about the z-axis before the division and returned to its original orientation following the division. In order for the plane at $x = 0$ to coincide with the boundary plane, the model must be shifted -0.6 km in the rotated x direction during the division as well.

Alternative, morphology-based regional division schemes are also possible (though not considered in detail here), and may lead to useful representations of the body density distribution. It is worth noting that the use of constant-density spheres as mascons inherently distorts the mass distribution representation due to void space in the model. Other extended mascon structures for which the Stokes' coefficients can be calculated in closed form and as a linear function of the density would also provide a valid basis for the methods presented here, and may provide a more continuous representation of the mass distribution. In fact, for sufficiently convex shape models, the simplex-based polyhedral subdivision of Takahashi and Scheeres could be considered a member of this group of “mascons”. The effects and advantages of more complex division schemes and mascon geometries are topics left to future work.

5.5 Validation: Recovery of a Heterogeneous Mascon Model

To validate the regional mascon density estimation algorithm, a simulated “truth” spherical harmonic gravity field is calculated from a simple heterogeneous mascon density distribution. Then, the regional densities of several mascon models with identical mascon geometry but varying regional geometry are estimated using the coefficients of the simulated reference gravity field as measurements. Only the lower-degree and -order coefficients of the true field are used as measurements to evaluate the performance of the regional density estimation algorithm in the presence of incomplete knowledge of the true field.

The simulated truth mascon model selected is a two layer infill mascon model with uniform mascon sizes throughout (see Fig. 5.2). Details on the simulated truth model construction and coefficient uncertainty assignment are found in Appendix D. A 10x10 spherical harmonics representation of the mascon gravity field is generated by calculating the Stokes’ coefficients using Eq. 5.4 at a reference radius equal to the circumscribing radius of the body ($R_{\text{ref}} \approx 2.637$ km). For consistency with the realistic case considered later, the

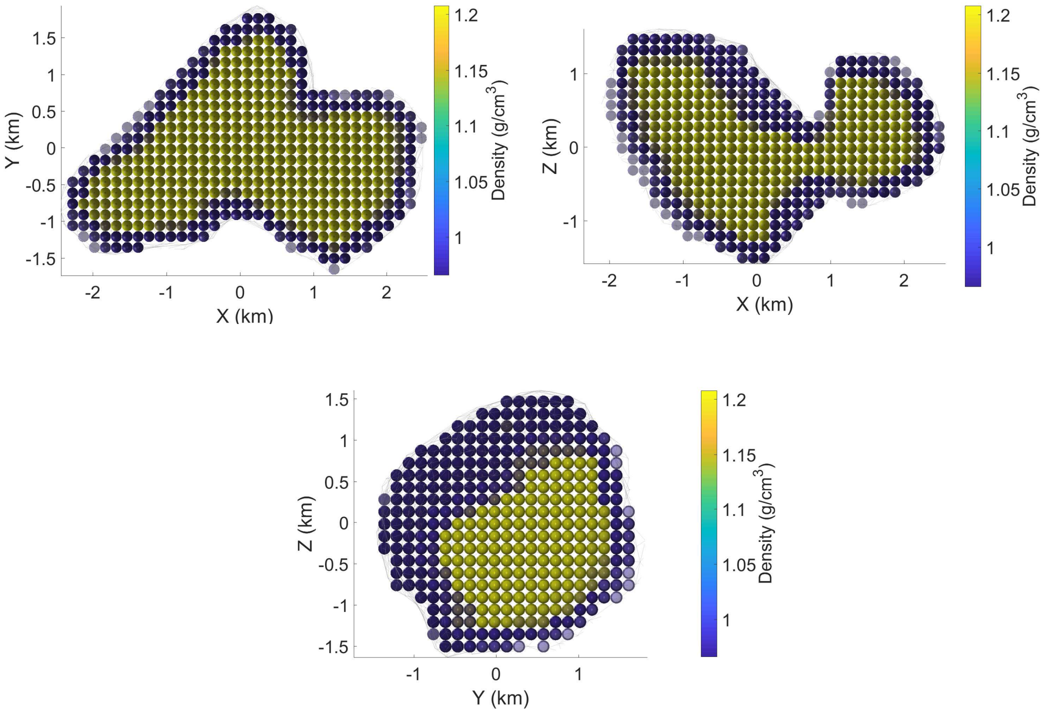

Figure 5.2: Two-layer heterogeneous reference mascon model, with sections shown at (a) z = 0 km; (b) y = 0 km, and; (c) x = 0 km. (IM2705_00-44r28_IM2662_44-95r28)

10x10 field is considered the “true” field, while the coefficients of a truncated 5x5 representation of the true field are used as measurements. No *a priori* densities are used (i.e. all terms in Eq. 5.14 and 5.16 including $[\bar{\sigma}_i]$ and $\mathbf{P}_{\sigma\sigma}^{-1}$ are simply dropped).

Six regional mascon configurations are built and fit to the reference spherical harmonics model. All possess identical numbers and positions of individual mascons, but the region configuration is varied to test its effect on the coefficient fit and accuracy of the density estimation. Details for each

Table 5.1: Mascon Region Test Models for Heterogeneous Density Recovery

Config #	Regional Configuration	N_{reg}	cond($\mathbf{\Lambda}$)	$\epsilon_{\rho,\text{RMS}}$ (%)
1	Identical to Reference	2	13.953	1.15E-13
2	Two-Layer w/ 2x1x1 Cartesian Grid	4	282720	5.90E-13
3	Two-Layer w/ 2x2x2 Cartesian Grid	16	8.1923E+16	0.682
4	One-Layer w/ 2x2x2 Cartesian Grid	8	1.0909E+13	12.1
5	One-Layer w/ 3x2x2 Cartesian Grid	12	1.7314E+14	15.0
6	One-Layer w/ 3x3x3 Cartesian Grid	24	2.1613E+18	23.6

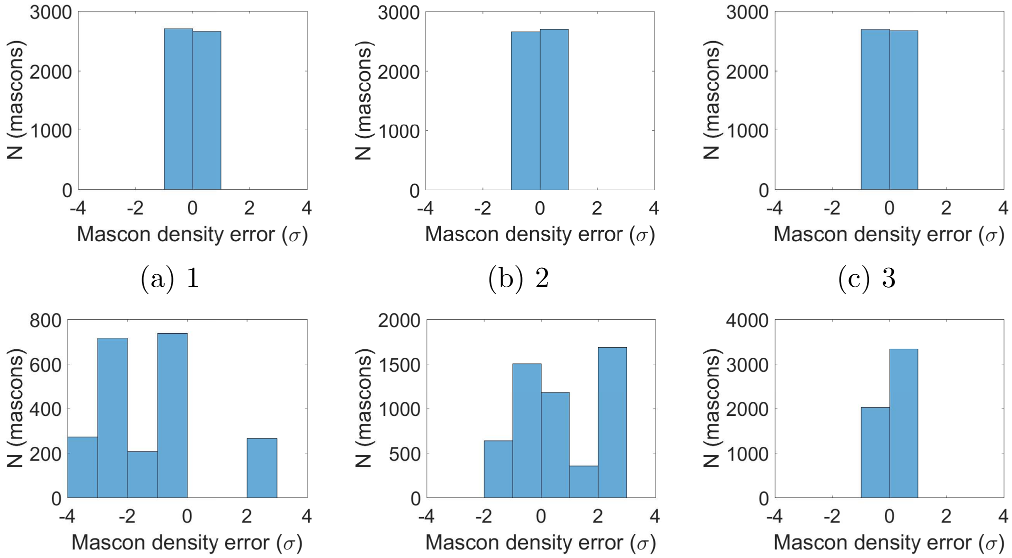

(a) 1 (b) 2 (c) 3

(d) 4 (e) 5 (f) 6

Figure 5.3: Relative mascon density estimate errors measured in estimated density standard deviations for each mascon model in Table 5.1. Plots are labed by their configuration number as listed in the same table.

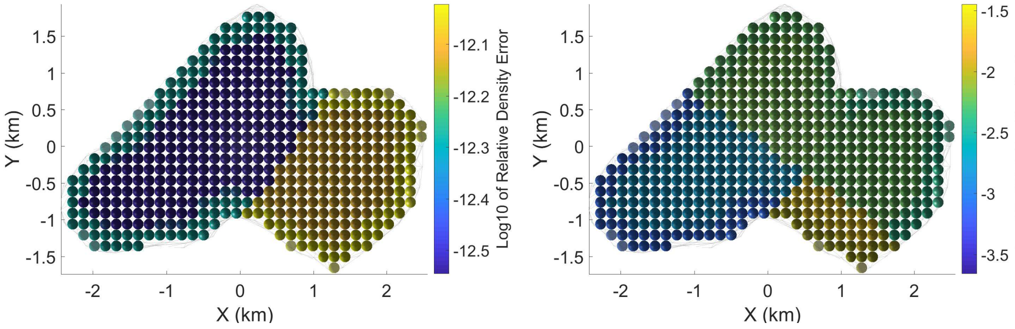

(a) Configuration #2

(b) Configuration #3

Figure 5.4: Mascon relative density errors for recovery configurations #2 and #3.

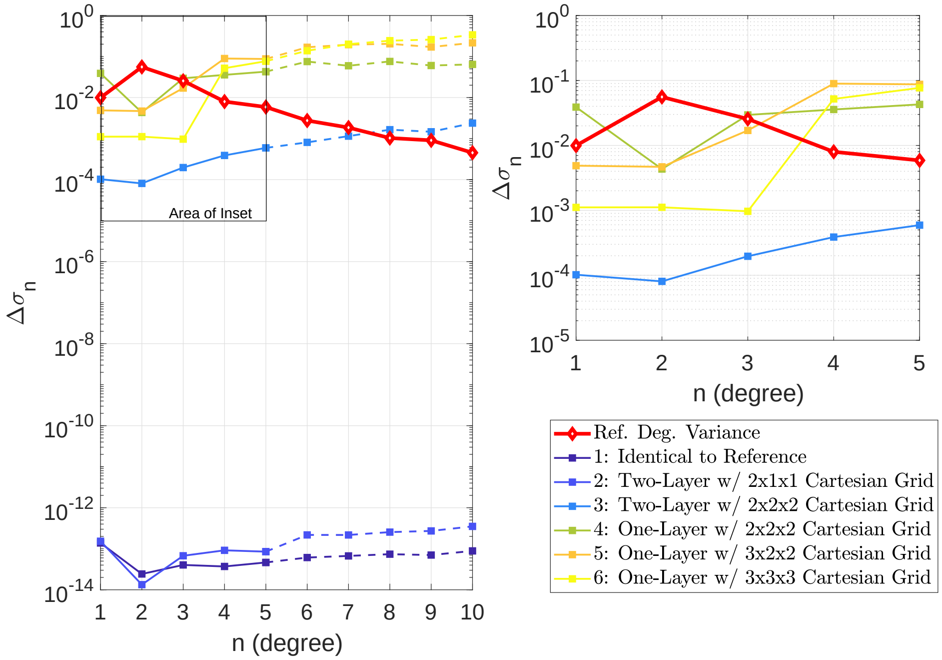

Figure 5.5: Degree error variances for recovery of a two-layer mascon model using several mascon region configurations. Error variances for coefficient degrees not included in the measurements are plotted with dashed lines.

configuration are listed in Table 5.1, along with information matrix condition numbers and RMS density errors. Histograms of mascon density errors measured in units of estimated density uncertainty are shown in Fig. 5.3. Estimated regional density uncertainties are equal to the square root of the diagonal entries in $\mathbf{\Lambda}^{-1}$. The degree error variance for degrees 1 through 10 is shown in Fig. 5.5 for the six regional configurations and is compared against the reference model degree variance.

As expected, the algorithm recovers the reference density distribution almost exactly when presented with an identical region configuration (configuration #1 in Table 5.1). Density values are recovered to around 13 digits of precision, while the coefficient fit is also nearly exact. Although configuration #1 has the lowest region count (and fewest degrees of freedom), the density estimation algorithm is able to recover the reference model because the mascon and region configuration are identical to the true configuration.

Density value recovery and coefficient errors are also good for configurations #2 and #3. These configurations also draw benefits from the use of identical layer bounds to the reference model, but do not fit the reference model as well as configuration #1, due to the ill-conditioning of the problem introduced by the increased degrees of freedom. This ill-conditioning is especially noticable between configurations #2 and #3, where the region count quadruples and the condition number increases by a factor of 10^{11}. Effects of the well-known ill-conditioning are also noticable in local mascon density errors, shown in Fig. 5.4. While errors are much higher for configuration #3, they remain below 1% for most mascons. Density errors are also lower for both configurations in the larger lobe of the body, indicating greater observability of the corresponding regional densities.

The final three tested configurations are all variants of a pure Cartesian-gridded regional division approach. As Fig. 5.5 shows, these models exhibit higher errors in their spherical harmonics coefficients than the first two configurations. Still, the impact of increasing regional grid resolution is clear in generally improved degree error variances across most coefficient degrees. However, improvements in the coefficient fit trade off with accuracy in the estimated density distribution for the gridded models (Table 5.1). Although the density errors increase with the region count, they also become more consistent with the (large) estimated density uncertainty, which increases as the conditioning of the problem worsens (see Fig. 5.3). Such effects of the region geometry on the coefficient fit demonstrate the importance of the specified geometry on the ability of the density estimation algorithm to accurately recover density values and fit the harmonic coefficients.

Finally, consider the degree error variance of the estimated models for $n = 6$ to 10. The higher degree coefficients are not used as measurements for this simulation, yet the coefficient errors do not significantly worsen above degree 5 for any estimated model relative to its error at degree 5. While the inclusion of the higher degree terms as measurements may help reduce the error in those terms, it is clear that the most significant factors for the accuracy of the coefficient fit for all degrees are 1) the accuracy of the mascon and region configuration, and 2) the uncertainty used on the coefficient measurements. Put simply, an estimated mascon model that accurately fits the measured coefficients should be expected to also fit higher degree coefficients with similar, albeit somewhat reduced, accuracy, even when those coefficients are not available as measurements.

5.6 Case Study at Comet 67P/C-G

The European Space Agency's Rosetta spacecraft orbited Comet 67P/C-G, a Jupiter-family comet with an irregular, nonconvex shape, from August 2014 to September 2016. The orbit determination subsystem estimated the gravitational spherical harmonic coefficients of the body using multiple high-altitude radiometric data arcs to the fifth degree and order[22]. Due to the body's complex shape, a much larger spherical harmonics field is required to model the true gravity field to high accuracy; however, the OD solution represents the best gravity field knowledge currently available.

Interest in near-surface science operations at the comet has been demonstrated in both Rosetta's Philae lander and the proposed Comet Astrobiology Exploration Sample Return (CAESAR) mission, a NASA mission concept to return regolith samples from the comet surface. Those and future efforts would benefit from density distribution and near-surface gravity field modeling that take advantage of the gravity field representation of the Rosetta OD solution. To test the mascon regional density estimation algorithm presented in this work for such purposes, many mascon element and region configurations are built, and their regional densities are estimated using the Rosetta OD coefficients as measurements.

5.6.1 Effect of Mascon Resolution and Regional Geometry

Previous work[62, 69] investigated methods to estimate asteroid density distributions using polyhedral basis functions, which can be computationally expensive to evaluate depending on the resolution of the underlying shape model. Conventional mascon models are well-known to require an excessive number of elements to accurately model a homogeneous polyhedral gravity field, thereby eliminating any computational advantage. In order to narrow the search for accurate mascon proxy models for the Rosetta OD gravity solution, some investigation of the effect of increasing mascon resolution on the coefficient fit is warranted.

In this experiment uniformly spaced mascon models are built at seven different resolutions, spanning element counts from 572 to 11389. Two Cartesian regional division schemes are applied, one 4x3x3 and the other 6x2x2, ensuring an equivalent total region count not exceeding the total number of coefficients in the OD solution. A constant-density *a priori* state is applied for all models, with weights held constant across all models and tuned such that only positive density values would be returned by the filter. Figure 5.6 shows the degree error variances for degrees one through five plotted as a function of mascon model resolution for each regional division scheme.

The degree error variances show no apparent advantage for high-resolution models for either regional division scheme and for all available harmonic degrees. In fact, degree error variance minima can be identified near the low-resolution end of the curves, indicating that mascon models with half-spacing distances of around $R_{\max}/20$ may offer improved coefficient errors over higher or lower resolution models. This finding eliminates the necessity of building high-resolution mascon configurations for the general proxy model search in the next subsection. Also, lower-resolution proxy models that exhibit low coefficient errors may also offer computational advantages over all but the lowest-resolution polyhedral alternatives while remaining globally valid outside the body surface. The result is intuitive: the function being fit is of low resolution (on the order of ten coefficients) - therefore, it is not surprising that a point of diminishing returns occurs quickly when increasing the resolution of a proxy model.

5.6.2 Pareto-Optimal Model Search

A total of 100 regionally-divided mascon model solutions are built for Comet 67P/C-G using the Rosetta OD gravity solution as the reference field. The mascon and region configurations are varied using a similar design space grid search approach as is applied in Chapter 4. Shape model scaling is performed using the Fixed Local Perpendicular Depth (FLPD) approach, also presented in Chapter 4. Single- and double-layered models are investigated, with infill mascon half-spacing distances varying from $0.028R_{\max}$ to $0.053R_{\max}$. Single-layer models with core mascon counts from zero to five are built, and

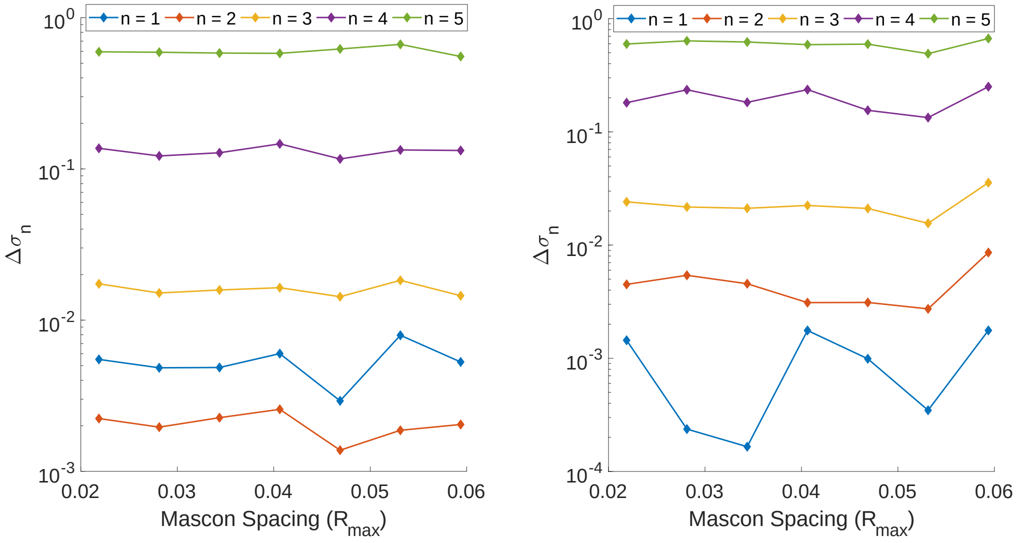

(a) 4x3x3 Cartesian Spacing (b) 6x2x2 Cartesian Spacing

Figure 5.6: Degree error variances as a function of mascon resolution for two regional geometries.

outer-bound scaled shape models (expressed via scale factor α_{OB}) vary from 0.75 to 0.95. The numbers of X, Y, and Z regional grid intervals are varied in the ranges $N_x = [3, 6]$, $N_y = [2, 3]$, and $N_z = [2, 3]$ respectively. The fourth regional division method detailed in the fourth section of this work is applied for the whole model set; that is, the mascon configurations are divided such that all cores constituted individual density regions, and the remaining mascons are sorted into regions by both layer membership and Cartesian grid division, if any.

A constant-density *a priori* state is applied for all models, with mascon masses assigned such that the total prior model mass equals the primitive body mass. Weights in $\mathbf{P}_{\sigma\sigma}^{-1}$ are held constant across all models and tuned such that only positive density values are returned by the filter. Coefficient uncertainties reported for the OD solution are normalized and positioned along the diagonal in $\mathbf{P}_c$. The coefficients C_{11}, S_{11}, C_{21}, and S_{21}, which were fixed at zero with no uncertainty in the OD solution, are assigned a nominal normalized uncertainty of $\sigma = 10^{-8}$. Assigning a small, nominal uncertainty to these coefficients permits small deviations in the center-of-mass location and principal axis orientation of the mascon proxy models relative to the OD solution. Hard constraints on either inertial quantity could be applied in the general case; however, given the limited number of degrees of freedom in this particular problem, constraining these quantities in a least-squares sense is deemed a reasonable trade-off for achieving better fits for the higher-degree and -order coefficients.

All mascon models are subjected to a five-dimensional Pareto sort [48] based on their degree error variances for harmonic degrees one through five. Models deemed "Pareto-optimal" exhibit performance such that no other model in the set possesses error variances less than those of a Pareto-optimal model in all five degrees. Figure 5.7 shows the degree error variances for all 100 mascon models compared with the reference model degree variance. The degree error variance data for Pareto-optimal models are highlighted, while non-optimal model performance is shown in gray. An abbreviated code represents each mascon model in the key: the code contains the number of cores ("C"), if any, the number of infill mascons ("IM"), the scale factors of the shape models bounding the mascon distribution ("00-XX"), the mascon reso-

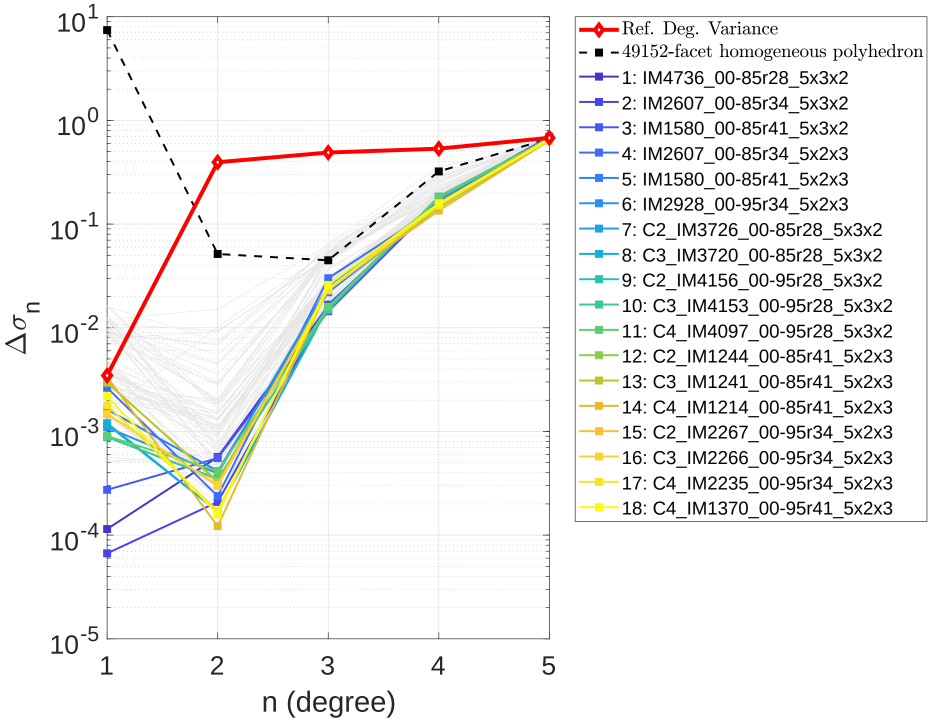

Figure 5.7: Degree Error Variances of Mascon Proxy Models for Comet 67P OD Solution

lution expressed as the half-spacing distance in thousandths of $R_{\max}$ (“rXX”), and the regional division grid spacing (N_xxN_yxN_z). The error variances of the estimated models are compared with the error variances for a high-resolution, homogeneous polyhedral model for context.

Generally, the degree error variances for the mascon solutions increase in magnitude with degree. Some Pareto-optimal models have error variances below 20% out to the fourth degree, but all mascon error variances begin to approach the reference degree variance at degree five. These trends correlate

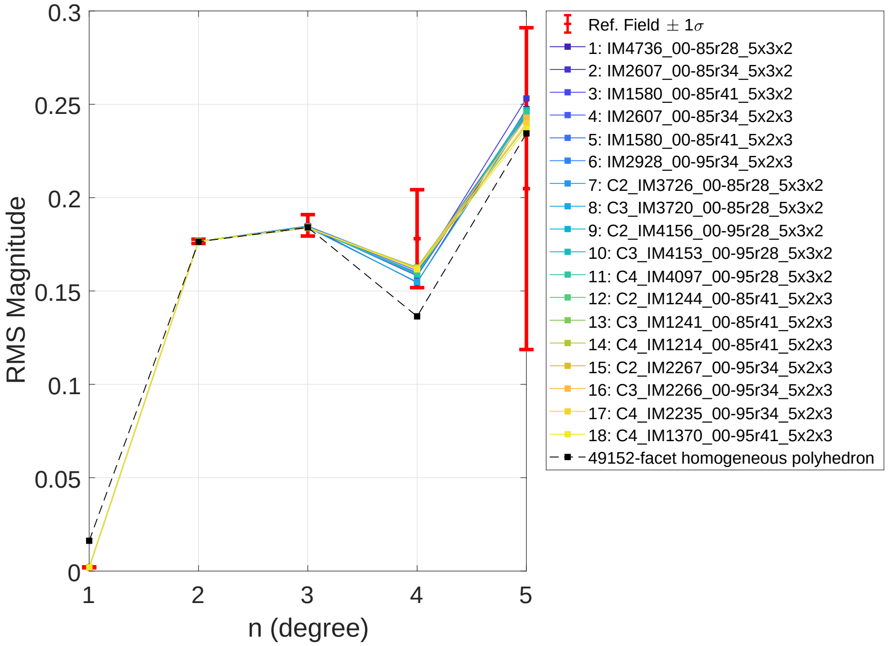

Figure 5.8: RMS Stokes' Coefficients of Mascon Proxy Models Compared to Comet 67P OD Solution

with the coefficient uncertainties of the OD gravity field, which increase with degree and approach the magnitude of the coefficients themselves at degree five. Error variances higher than 10% may facially appear to indicate that the mascon proxy models do not provide an accurate fit. However, in Fig. 5.8, it is apparent that all Pareto-optimal mascon models are statistically consistent with the OD solution, as their RMS coefficient magnitudes by degree fall within 1σ uncertainty intervals for the reference field. The Pareto-optimal models show improved error variances relative to the homogeneous polyhedral model for all five degrees (see Fig. 5.7). The homogeneous model also falls outside of the 1σ uncertainty intervals for coefficient degrees one and four (see

Table 5.2: Pareto-Optimal Comet 67P Mascon Proxy Model Characteristics

#	Cores	Infill MC	α_{OB}	N_x	N_y	N_z	N_R	$\epsilon_{\ddot{\mathbf{r}},\mathrm{RMS}}$ @ 7 km (%) (Relative to OD)	$\epsilon_{\ddot{\mathbf{r}},\mathrm{RMS}}$ @ Surface (%) (Relative to CD poly)	RMS $\Delta\ddot{\mathbf{r}}/\ddot{\mathbf{r}}_{\mathrm{mean}}$ @ Surface (%)
1	0	4736	0.85	5	3	2	25	0.55	11.6	3.84
2	0	2607	0.85	5	3	2	24	0.55	11.2	4.50
3	0	1580	0.85	5	3	2	24	0.55	12.4	3.24
4	0	2607	0.85	5	2	3	26	0.55	12.2	3.20
5	0	1580	0.85	5	2	3	27	0.55	13.9	3.31
6	0	2928	0.95	5	2	3	26	0.55	17.6	4.03
7	2	3726	0.85	5	3	2	27	0.55	11.8	4.11
8	3	3720	0.85	5	3	2	28	0.55	11.8	4.12
9	2	4156	0.95	5	3	2	27	0.55	16.3	5.19
10	3	4153	0.95	5	3	2	28	0.55	16.3	5.19
11	4	4097	0.95	5	3	2	29	0.55	16.3	4.97
12	2	1244	0.85	5	2	3	29	0.55	13.4	3.75
13	3	1241	0.85	5	2	3	30	0.55	13.4	3.75
14	4	1214	0.85	5	2	3	31	0.55	13.5	4.50
15	2	2267	0.95	5	2	3	28	0.55	18.2	2.57
16	3	2266	0.95	5	2	3	29	0.55	18.2	2.57
17	4	2235	0.95	5	2	3	30	0.55	18.1	2.84
18	4	1370	0.95	5	2	3	31	0.55	21.0	5.02

Fig. 5.8).

Further characterization of the Pareto-optimal models is provided in Table 5.2. The ninth column shows the RMS relative acceleration error between the OD gravity solution and the 15 Pareto-optimal mascon proxy models. The comparison is performed at 15130 points on a 7 km radius sphere, which was the lowest altitude at which radiometric data was used to develop the multi-arc Rosetta OD gravity solution[22]. The points are spaced evenly to avoid oversampling at the poles using a solution to the Thomson problem[74]. Each of the Pareto-optimal mascon models has RMS errors of around 0.55%, while the constant density polyhedral model has a slightly higher RMS error

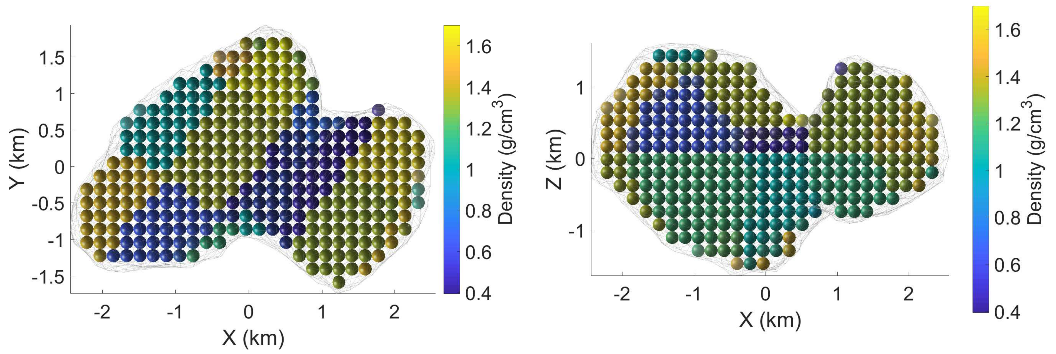

(a) From +Z axis (b) From -Y axis

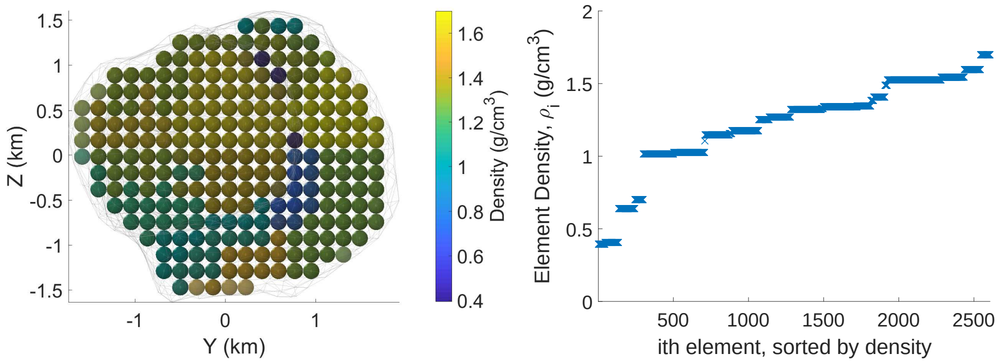

(c) From +X axis

Figure 5.9: Pareto-Optimal Mascon Model #2 (IM2607_00-85r34_5x3x2) Density Distribution

of 0.68%.

While a comparison with the reference spherical harmonics field is possible at the 7 km sphere, no such comparison can be made in the near-surface region. However, the consistency of the estimated mascon models with other low-altitude gravity field proxies may be evaluated. One alternative, commonly-used low-altitude proxy is the homogeneous polyhedron; the optimal mascon models are compared to a 49152-facet homogeneous polyhedral model for 67P at the model surface. Root-mean-square errors between the models taken at the shape model facets are reported in the tenth column of Table 5.2. Mascon model #2, which exhibits both low coefficient errors and relatively low error with the homogeneous polyhedral model, is shown in Fig. 5.9.

For additional consistency analysis, samples of the gravititational acceleration for each of the 18 Pareto-optimal mascon models are taken at 10 points each along the coordinate directions and in each octant, spaced at intervals of $0.1R_{\max}$ radially away from the surface. At each evaluation point, a mean and standard deviation are calculated among the model set. Figure 5.10 shows the standard deviation components at each evaluation point, and the eleventh column of Table 5.2 gives the RMS difference between each model's surface acceleration and the mean surface acceleration. The differences are generally small ($< 6\%$) but not insignificant. The variance in the acceleration fields generally grows the surface is approached; however, the standard deviation values generally fall within 10% of the local mean acceleration, except at a few points. The small but significant differences among the models' gravity fields suggest that these solutions could be considered as a set of feasible field representations. Upon spacecraft arrival, carefully designed orbits could be used to collect measurements of the gravity field to help narrow the set of feasible solutions. Note that the mascon models developed in this work are fit with coefficients estimated from high-altitude data; improved mascon models are achievable given more spacecraft data collected within the circumscribing

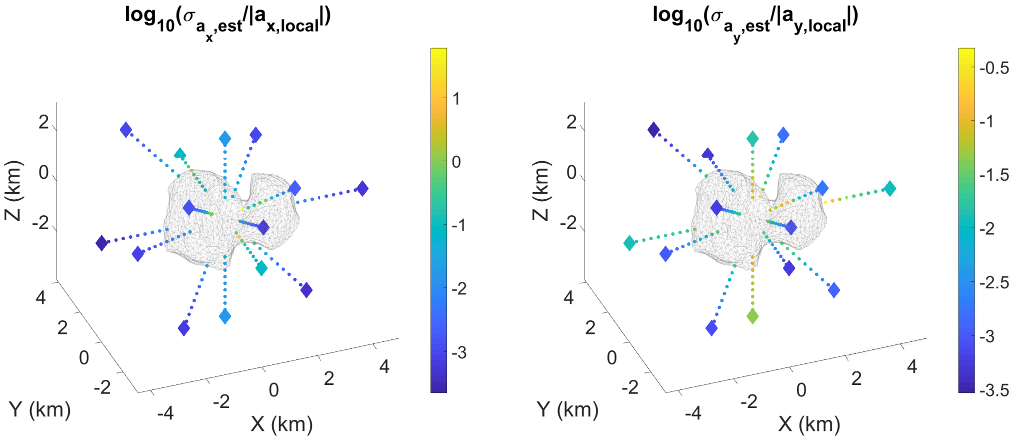

(a) X Std. Dev. (b) Y Std. Dev.

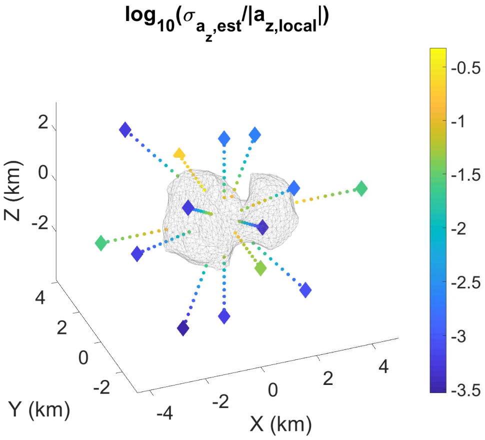

(c) Z Std. Dev.

Figure 5.10: Gravitational acceleration standard deviations measured relative to the mean acceleration components for Pareto-optimal mascon proxies in Table 5.2.

sphere.

5.7 Conclusion

A mascon-based approach to generating low-altitude gravity field proxy models and small body density distribution estimates using a spherical harmonics reference field is introduced, validated, and demonstrated in a realistic use-case. By dividing mascon models into regions of common density, the length of the unknown density vector that describes the mass distribution is reduced, and the unobservability of the gravity inversion problem is mitigated. Since the Stokes' coefficients for such a regional mascon model are a linear function of the shortened density vector, a batch linear least-squares filter is derived that fits the global mascon coefficients to a reference spherical harmonic field and estimates the regional density vector. Such a filter is shown to permit the recovery of heterogeneous mascon models with high accuracy, provided a similar mascon and region configuration. Using a published spherical harmonic gravity solution for Comet 67P as the reference field, the regional mascon density estimation algorithm generates mascon model solutions that are statistically consistent with the reference in terms of their Stokes' coefficients and acceleration errors. The inclusion of a weighted homogeneous prior enables the estimation of positive-valued density distributions for such statistically consistent models.

Regional mascon models such as those generated here may serve as statistically-consistent proxies for spherical harmonics representations, and they provide continuous, smooth, and exact gravity field representations in the low-altitude regions where spherical harmonics models diverge. Note that no conditions need be placed on the convexity of the body shape for the development, solution, or execution of the mascon models in the current work. Relatively low-resolution mascon models are shown here to be sufficient when fitting to a low-degree and -order reference field. The low resolution of the models offers additional benefits in the form of relatively fast field evaluations. A comparison with heterogeneous polyhedral density distribution models is useful here. Polyhedral gravity field runtimes increase with the number of facets in the global model[79]. Each regional subdivision of a polyhedron delineates new internal boundaries within the original polyhedron and increases the total number of facets in the model, thereby increasing the evaluation time. Dividing mascon models, on the other hand, does not increase computation time because no terms are added to the force model for a given mascon arrangement.

Chapter 6

Conclusions

The current and future manifest of science missions exploring small celestial bodies demands computationally efficient tools to accurately represent the primitive body gravity field for various guidance, navigation, and control and geoscience applications. In this work discrete-element gravity models are reexamined in the small body context with the objective of accelerating accurate field computations by modifying conventional mascon model geometries and force models and solving carefully designed gravity inversion problems. The resulting methods build proxy gravity models that are grounded in the body mass distribution and provide valid gravity field representations across the spacecraft operations domain in space and time. A summary of the contributions to the field made by the work presented in this dissertation was given in Chapter 1, and a list of accepted and submitted publications and conference presentations is given in Appendix D. In this final chapter we will summarize the conclusions, place the work in context, and suggest paths for future research.

The conventional small body gravity modeling approaches applied in this work were introduced in Chapter 2. Focus was placed on gravity representations for which the potential forms a solution to Laplace's Equation. The relevant gravity modeling approaches yield field representations that are tied to the primitive body mass distribution via various approximations of the integral form of the potential over a continous body. Discrete-mass models combine accurate shape representation with a simple, parallelizable force model, yet are known to suffer from near-field degradation in accuracy and high memory burdens in the conventional form. Spherical harmonics are broadly used for primitive body gravity representations and may be truncated to arbitrary degree and order to suit the observability, accuracy, or runtime constraints of a particular application. However, spherical harmonics series diverge within the body's circumscribing sphere, making them ill-suited for near-surface gravity evaluations. The polyhedral model offers a robust solution for the gravitational potential, attraction, gradient and laplacian given a density distribution and a polyhedral shape model, but the conventional implementation can suffer from computational inefficiency. These basic gravity models are leveraged for their various advantages in the gravity models presented in this work.

The theoretical and algorithmic framework for a novel hybrid small body gravity modeling approach was laid out in Chapter 3. The approach, called Multi-layer Mascon and Exterior Spherical Harmonics (MultiMESH), mitigates near-surface field degradation and large memory burdens typical of conventional mascon models by modifying the packing geometry through the layered placement of polydisperse spherical discrete elements. Applying spherical harmonics gravity signatures to large elements adds fidelity at a lower cost to memory and execution time when compared with the substitution of additional smaller mascons. A two-step gravity inversion procedure using a sequence of linear batch least-squares filters fits the MultiMESH potential to the polyhedral surface potential by solving for the discrete-element mass distribution. Several filtering techniques were explored, and the two-step filtering algorithm was shown to best minimize the potential residuals for typical model configurations. In an application for 433 Eros, the most efficient MultiMESH model configurations were shown to offer computational speedups of up to an order of magnitude relative to reduced-resolution polyhedral models of equivalent accuracy. MultiMESH mass distributions are permitted to stray into the nonphysical in this problem, with the existence of mass discontinuities and negative mass values considered secondary to an accurate mathematical field model.

Given a bulk density estimate and polyhedral shape model, the model generation algorithm presented in Chapter 3 is applicable to any small celestial body. The method is extended for asteroids 216 Kleopatra and 25143 Itokawa and Comet 67P/Churyumov-Gerasimenko in Chapter 4. A modification is made to the shape model scaling method used for discrete-element packing to adapt it for bodies with significantly nonconvex regions. To optimize MultiMESH models for each body according to their accuracy, memory footprint, and execution time, the design parameter space is explictly defined and subjected to a global search. Pareto-optimal MultiMESH models are identified for each of the three bodies that provide significant computational efficiency advantages over reduced-resolution polyhedral models of equivalent accuracy. The existence of model "families" is posited, wherein MultiMESH model members consist of equivalent numbers of elements but possess shell layers at varying depths. Optimal shell burial depths may be identified that depend on the shell element spacing, inner layer characteristics, and the body being modeled. The implications of MultiMESH model efficiency gains in the context of trajectory computation (for orbit determination, mission design, or GNC applications) are significant. Such applications commonly require millions of gravity evaluations, implying potential time savings of hours to days when substituting efficient MultiMESH proxies.

A mascon-based approach to generating low-altitude gravity field proxy models and small body density distribution estimates using a spherical harmonics reference field is introduced, validated, and demonstrated in a realistic use-case in Chapter 5. By dividing mascon models into regions of common density, the length of the unknown density vector that describes the mass distribution is reduced, and the unobservability of the gravity inversion problem is mitigated. Since the Stokes' coefficients for such a regional mascon model are a linear function of the shortened density vector, a batch linear least-squares filter is derived that fits the global mascon coefficients to a reference spherical harmonic field and estimates the regional density vector. Such a filter is shown to permit the recovery of heterogeneous mascon models with high accuracy, provided a similar mascon and region configuration. Using a published spherical harmonic gravity solution for Comet 67P as the reference field, the regional mascon density estimation algorithm generates mascon model solutions that are statistically consistent with the reference in terms of their Stokes' coefficients and acceleration errors. The inclusion of a weighted homogeneous prior enables the estimation of positive-valued density distributions for such statistically consistent models.

6.1 Future Work

The development of fast and accurate gravity model proxies in this work is foundational; that is, by accelerating field computations and providing accurate low-altitude gravity representations, the models may enable a variety of future studies in the fields of geophysical analysis, trajectory design, guidance, navigation, and control, and small body gravity modeling. We begin by listing several efforts that may improve the gravity modeling methods presented in this work:

- This work discusses three shape model scaling methods suitable for small bodies of various shapes. Of these, Fixed Local Perpendicular Depth (FLPD) scaling best regulates the mascon burial depth for convex and nonconvex shapes, enabling the identification of optimal burial depths for surface acceleration accuracy. Additional efforts to improve element layering techniques, including by shape erosion, may result in more robust techniques for restricting mascons to a certain constant local depth throughout the body.

- Reformulation of the filter cost function in Chapters 3 and 4 to include constraints on mass values and density distribution smoothness may result in more realistic models for the body mass distribution. Such constraints would be of interest in geophysical applications in particular.

- No parallelization was used in measuring the computational efficiency of any models generated in this work. Experiments with parallel force evaluations for MultiMESH models are expected to result in significant runtime savings in absolute terms. Although mascon parallelization is simpler to implement due to lack of shared memory and the simplicity of the force function, relative runtime improvement over polyhedral methods would likely be minimal given that polyhedral fields are also amenable to parallel implementation. Several mechanisms for parallel implementation are available, among them Message Passing Interface (MPI), OpenMP, and Graphics Processing Units (GPUs).In a range of multi-disciplinary problems, GPUs have shown one to three order of magnitude speedups, and their relatively low cost compared with computing clusters makes them even more attractive for possible future onboard applications in autonomous space systems.

- For regional mascon modeling, alternative morphology-based regional division schemes are possible, and may lead to useful representations of the body density distribution. In particular, schemes that divide the body along suspected geological boundaries (in the case of contact binaries, for instance) may benefit the analysis and result in more accurate models of the density distribution.

- The use of constant-density spheres as mascons inherently distorts the mass distribution representation due to void space in the model. Other extended mascon structures for which the Stokes' coefficients can be calculated in closed form and as a linear function of the density would also provide a valid basis for regional discrete-element density estimation, and may provide a more continuous representation of the mass distribution.
- Previous work in the literature[49] has explored the estimation of mascon models using spacecraft radiometric data as filter measurements. Future efforts could consider the discrete-element models built using MultiMESH and regional density estimation techniques as useful *a priori* density models in such an estimation scheme.

Finally, we consider a few potential applications of these models:

- The flexible packing algorithm developed for this work could be utilized to generate a variety of feasible density maps for small body mission targets. Given some uncertainty in the density distribution of the body derived from geophysical analysis, Monte Carlo analysis could sample the space of feasible mass configurations and evaluate the expected uncertainty in the gravity field in the form of Stokes coefficients.

- The computational efficiency gains achieved by MultiMESH models may enable exhaustive searches for stable orbits and trajectories around a wide set of candidate small bodies. Such an effort could archive useful orbit families (i.e. frozen, periodic, or quasi-periodic). The archive's objective would be to ease the rapid trajectory design and optimization processes for ground-in-the-loop and onboard applications by providing a set of good initial guesses at the targeted bodies.

- Because MultiMESH and regional mascon models are valid anywhere outside the body surface, they provide a fast and accurate alternative to the polyhedron for the design of landing trajectories. Studies comparing descent trajectories in the polyhedral and modified mascon frameworks would validate the use of models developed using the techniques in this work for such purposes. Accelerated computations in this context may enable the consideration of low delta-v descent options or autonomous onboard navigation during the descent itself.

Appendices

Appendix A

Performance Data for 433 Eros MultiMESH Models

Table A.1: Performance Metrics for the 433 Eros Tested Model Set (Pareto Optimal Model #s in bold)

#	MultiMESH ID	η	$\overline{\tau}_{\text{eval}}$ (ms)	$\epsilon_{\text{RMS,low}}$ (m/s^2)	$\epsilon_{\text{RMS,hi}}$ (m/s^2)	$\epsilon_{\text{RMS,low}}$ (%)	$\epsilon_{\text{RMS,hi}}$ (%)
1	IM91_00-60r0.059_IM9596_60-90r0.016	38750	2.2E-01	5.0E-07	1.0E-08	1.0E-02	4.1E-04
2	IM125_00-60r0.053_IM2346_60-90r0.025	9886	5.6E-02	1.6E-06	1.9E-08	3.4E-02	7.7E-04
3	IM174_00-60r0.047_IM1190_60-90r0.031	5458	3.1E-02	3.7E-06	5.4E-08	8.1E-02	2.2E-03
4	IM274_00-60r0.041_IM688_60-90r0.038	3850	2.1E-02	5.8E-06	1.1E-07	1.3E-01	4.8E-03
5	IM874_00-85r0.038	3497	1.9E-02	8.6E-06	2.1E-07	1.9E-01	8.5E-03
6	IM1151_00-85r0.034	4605	2.6E-02	7.8E-06	1.9E-07	1.8E-01	8.1E-03
7	IM1362_00-90r0.034	5449	3.0E-02	5.9E-06	1.2E-07	1.3E-01	4.9E-03
8	IM680_00-70r0.034	2721	1.6E-02	1.9E-05	8.5E-07	4.6E-01	4.1E-02
9	IM2112_00-85r0.028	8449	4.8E-02	3.5E-06	5.2E-08	7.7E-02	2.2E-03
10	IM4457_00-85r0.022	17829	1.0E-01	1.4E-06	1.6E-08	2.9E-02	6.4E-04
11	IM12296_00-85r0.016	49185	2.9E-01	6.0E-07	3.2E-09	1.3E-02	1.3E-04
12	SH2_00-60_6.7_IM689_60-85r0.034	2887	2.2E-02	8.3E-06	2.0E-07	1.9E-01	8.8E-03
13	SH2_00-70_6.7	130	4.0E-03	7.7E-04	1.4E-04	18	5.5
14	SH2_00-75_7.7_IM339_75-85r0.034	1502	1.4E-02	1.9E-05	5.4E-07	4.2E-01	2.1E-02
15	SH2_6.7_IM571_00-70r0.031	2406	1.8E-02	1.7E-05	6.7E-07	4.0E-01	3.3E-02
16	SH2_7.7_IM826_00-80r0.031	3441	2.4E-02	7.8E-06	1.7E-07	1.7E-01	7.8E-03
17	SH2_6.7_IM393_00-60r0.031	1694	1.4E-02	2.9E-05	1.5E-06	6.9E-01	7.0E-02
18	SH2_6.7_IM3136_00-60r0.016	12666	7.8E-02	8.3E-06	2.3E-07	1.9E-01	1.1E-02
19	SH2_6.7_IM4592_00-70r0.016	18490	1.1E-01	3.4E-06	5.2E-08	7.4E-02	2.3E-03
20	SH2_7.7_IM6586_00-80r0.016	26481	1.6E-01	1.1E-06	1.3E-08	2.3E-02	5.7E-04
21	SH3_00-60_7.6.7_IM1190_60-90r0.031	4963	3.6E-02	3.7E-06	5.4E-08	7.9E-02	2.2E-03
22	SH3_00-60_7.6.7_IM9596_60-90r0.016	38587	2.4E-01	5.0E-07	1.0E-08	1.0E-02	4.1E-04
23	SH3_00-70_6.7.6_IM913_70-90r0.031	3840	2.7E-02	4.3E-06	6.6E-08	9.2E-02	2.6E-03
24	SH3_00-70_6.7.6_IM7331_70-90r0.016	29512	1.9E-01	5.0E-07	1.0E-08	1.0E-02	4.1E-04
25	SH3_00-80_6.7.6_IM511_80-90r0.031	2232	1.9E-02	1.0E-05	2.4E-07	2.1E-01	8.1E-03
26	SH3_00-80_6.7.6_IM4159_80-90r0.016	16824	1.0E-01	6.5E-07	1.0E-08	1.3E-02	4.1E-04
27	SH3_00-85_7.7.4	178	6.6E-03	2.2E-04	3.1E-05	4.8	1.2
28	SH3_7.6.7_IM428_00-60r0.031	1902	1.7E-02	3.1E-05	1.9E-06	7.5E-01	9.2E-02
29	SH3_6.7.6_IM477_00-70r0.031	2083	1.8E-02	1.9E-05	8.2E-07	4.5E-01	4.1E-02
30	SH3_7.6.7_IM3376_00-60r0.016	13694	8.4E-02	8.9E-06	2.5E-07	2.1E-01	1.2E-02
31	SH3_6.7.6_IM3847_00-70r0.016	15563	9.5E-02	3.4E-06	5.2E-08	7.5E-02	2.3E-03
32	SH4_00-85_7.7.5.3	213	5.6E-03	2.0E-04	5.9E-05	4.7	2.2
33	SH3_00-70_6.7.6_SM1708_85	7020	4.5E-02	1.2E-06	1.3E-08	2.4E-02	5.0E-04
34	SH3_00-70_6.7.6_SM1708_95	7020	4.6E-02	6.2E-06	2.4E-08	1.3E-01	9.1E-04
35	SH3_00-70_6.7.6_SM6832_85	27516	1.6E-01	4.4E-07	9.6E-09	9.1E-03	4.0E-04
36	SH3_00-70_6.7.6_SM6832_95	27516	1.7E-01	6.2E-07	1.0E-08	1.2E-02	4.1E-04
37	SH3_00-70_6.7.6_SM27328_85	109500	6.6E-01	3.3E-07	1.8E-09	6.7E-03	7.5E-05
38	SH3_00-70_6.7.6_SM27328_95	109500	6.9E-01	7.6E-08	1.3E-09	1.5E-03	5.4E-05
39	SH3_6.7.6_IM477_00-70r0.031_SM1708_95	8916	5.8E-02	1.7E-06	1.4E-08	3.4E-02	5.3E-04
40	SH3_6.7.6_IM3847_00-70r0.016_SM1708_95	22396	1.4E-01	9.8E-07	1.1E-08	2.0E-02	4.5E-04
41	SH3_6.7.6_IM477_00-70r0.031_SM6832_95	29412	1.8E-01	4.6E-07	9.8E-09	9.2E-03	4.0E-04
42	SH3_6.7.6_IM3847_00-70r0.016_SM6832_95	42892	2.7E-01	2.6E-07	1.6E-09	5.2E-03	6.4E-05
43	SH3_6.7.6_IM477_00-70r0.031_SM27328_95	111396	7.0E-01	7.7E-08	1.3E-09	1.5E-03	5.5E-05
44	SH3_6.7.6_IM3847_00-70r0.016_SM27328_95	124876	8.0E-01	7.7E-08	1.3E-09	1.5E-03	5.5E-05
45	7790-facet, 3897-vertex polyhedral	222037	4.7E-01	2.9E-06	7.9E-07	6.8E-02	2.9E-02
46	1708-facet, 856-vertex polyhedral	48700	1.1E-01	3.5E-05	1.2E-05	8.5E-01	4.6E-01

Appendix B

MultiMESH Model Design Space Grid Search

Due to the large and variable dimensionality of the model design grid search space, several bounds and limitations must be placed on the search procedure to maintain its tractability. The length of many of the parameter vectors ($\mathbf{M}_p$, $\mathbf{N}_C$, α, $\mathbf{d}_I$) is dependent on the number of layers in a model, and the sizes of the arrays containing the initial position ($\mathbf{r}_{0,C}$) and maximum degree and order ($n_{\max}$) of any core elements is dependent on both N_L and $\mathbf{N}_C$. As a result, the number of searchable parameters increases as the number of layers in a model increases. For example, a model with $N_L = 1$ has up to $5 + 4N_C$ searchable parameters. When N_L is increased to 2, the maximum number of searchable parameters increases to $9 + 8N_{C,max}$. Within such a large search domain, selecting only a few search steps in each dimension can easily result in tens of thousands of generated models. Since a single model typically takes a couple of minutes (on a single processor) to pack, solve, and subject to a performance evaluation, total search time can easily stretch into weeks if no modifications are made to the search space.

The first and most effective modification is limiting the number of layers in any given model to 2. Though models with three or more layers are possible, the search space grows unreasonably large (> 12 dimensions). Tardivel[72] found that placing large-radius mass elements close to the center of a mascon distribution reduces surface field errors relative to models where large elements are located nearer the surface. To encourage this effect for MultiMESH models, all core elements are restricted to the innermost packing layer. Additionally, the total number of core elements for a single model is restricted to a maximum of 5 in order to minimize the number of function calls to the more computationally expensive spherical harmonics evaluation routine. Via visual examination of shape models, initial positions for up to 5 core elements can be pre-set for each body, thereby eliminating $\mathbf{r}_{0,C}$ from the search space. In addition, the effective length of $\mathbf{N}_C$ becomes one, and the dimension of the search space is reduced further.

Finally, we fix the value of $n_{\max}$ for all models and core elements and automate the selection of maximum values of element harmonic series degree and order based on the expected observability of the harmonic coefficients. Note that the observability of any particular high-degree harmonic coefficient varies with element size, proximity to the body surface, measurement geometry, and the degree and order of the coefficient itself. With thousands of unique combinations of these characteristics among the hundreds of gravity models generated in the grid search, determining $n_{\max}$ for each element based on the specific observability of that element's harmonic coefficients is an intractable problem. Previous trials have suggested that $n_{\max} > 7$ offers little marginal performance benefit to most MultiMESH models. The maximum degree and

Table B.1: Searchable Packing Parameter Bounds for the ith Layer

Parameter	Type	Lower Bound	Upper Bound
N_L	Discrete	1	2
$M_{p,i}$	Discrete	1 (A)	5 (E)
N_C	Discrete	0	5
α_i	Continuous	0.00	1.00
d_i (grid units)	Discrete	1	40
d_i (shell spacing)	Discrete	0.125	40

order for the largest core element in a MultiMESH model is therefore set to a value of 7, with additional smaller core elements receiving lower-degree and -order signatures in proportion to the ratio of the radius of the smaller core element to that of the largest core element. By automatically fixing n_{max} for all models, the parameter search space is again reduced.

With these constraints on the search space, its dimension is reduced to a maximum of $3N_L + 2$. With this more manageable size, it is possible to set reasonable bounds on each parameter type to define the global search (listed in Table B.1). Four of the parameters explicitly take only discrete values (N_L, $M_{p,i}$, N_C, d_i). The fifth (α_i) is theoretically continuous, but is evaluated at discrete values in the grid search. Note that the shape model scaling process is robust to the bounds on α_i due to the condition in Eq. 4.2. Values from 1 to 5 of the layer packing method parameter $M_{p,i}$ correspond to the packing method descriptions (A) through (E) in Table 4.1. The element center spacing distance d_i is expressed in in/out grid units to facilitate the simple grid placement packing process for infill elements. The upper bound on d_i is set at 40 grid units; elements packed at this upper bound have a half-spacing distance (equivalent to element radius for an array of constant density spheres) of 12.5% of the circumscribing radius of the body. Elements above that size are assigned spherical harmonics gravity signatures and treated as core elements. The spacing distance d_i is alternatively used to control the spacing of shell elements when $M_{p,i} = 4$. When $d_i > 1$, the parameter specifies the placement of a shell element at every d_ith projected shape model facet centroid. When $d_i < 1$, the parameter is required to take discrete values of $1/2^n$, where n is an integer used to generate 4^n points per facet via facet splitting. Each of those generated points is assigned an element, and the resulting shell layer is placed according to α_i.

Lastly, note that the grid search must be carefully designed to avoid generating duplicate models. The use of certain values of $M_{p,i}$, for instance, will void the searchability of d_i (particularly if $M_{p,i} = 2$ or 5, where no infill or shell elements are packed in the i^{th} layer). Varying d_i when $M_{p,i}$ takes either of those values imparts no change on the final model configuration, since d_i affects a model structure that simply does not exist within the model being built. The grid search algorithm automatically avoids such gaps in the search space, trimming significant runtime off the overall search procedure.

Appendix C

MultiMESH Model Nomenclature

Due to the wide variety of packing schemes and gravity signature assignments for the MultiMESH and mascon models developed in this work, it is important to develop a shorthand naming scheme which permits the unique identification of a particular model. The nomenclature presented here takes the form of a modular, alphanumeric identification code, and it encapsulates information about the number, type, distribution, and physical extent of the discrete elements in a particular model.

Since each layer of elements tends to be relatively homogeneous, the model ID code is constructed from a concatenation of layer identification codes. Using rough pseudocode for character string assignment, a model ID code begins with the innermost layer and ends with the outermost one:

```
<modelID>= <innerlayerID>_<layer2ID>_..._<outerlayerID>
```

Each layer code contains relevant information about the elements present in that layer. Generally, each layer code is structured such that:

```
<layerID>= <elementType><#_of_this_type>_ ...
                              ...<layerBounds><elementSize>
```

The term "elementType" refers to either infilled mascons ("IM"), shell mascons (“SM”) or spherical harmonics (“SH”), while ”elementSize” is either the artificial uniform radius (resulting from point spacing) of the mascons in this layer expressed as a fraction of the body reference radius or the degree and order of any spherical harmonics elements in this layer. For mascon models containing core elements with no spherical harmonics gravity signatures, “SH” is replaced by “C”. Layer bounds are expressed as a pair of two digit integers representing the reference scale factors (α_{ref}) of the shape model bounds (e.g. 40-70 for a layer extending from a 40% scaled shape model to one scaled to 70% of full size). For a shell layer, only the scale of the shape model surface upon which the shell rests is given. Shell element size is not given in the ID code since the spacing of shell mascons is defined entirely by their location on a scaled shape model. So, for instance, an inner layer containing 3 spherical harmonics core elements within a 60% shape model, where the spherical harmonics field sizes are 10x10, 12x12, and 15x15, can be represented with the code:

<layer1_ID>= SH3_00-60_10.12.15

Suppose additionally there were a layer of 1028 infilled mascons between 60% and 90% scale shape models, each having a normalized radius of 0.02. The code for this layer would then be:

<layer2_ID>= IM1028_60-90r0.02

If a model were to consist of these two layers, placed on top of one another, their layer ID codes could be concatenated to form a single code for the entire model.

<modelID>= SH3_00-60_10.12.15_IM1028_60-90r0.02

Alternatively, if the outer layer were instead an outer shell mascon layer with an equivalent number of elements affixed to a 70% scaled shape model, the model ID code would be:

<modelID>= SH3_00-60_10.12.15_SM1028_70

Now suppose that the same three spherical harmonics elements are placed within a 70% scale shape model, with 1028 mascons of normalized radius 0.02 filling all remaining available space within that scaled shape model. The model ID code is modified slightly in this case, with the common layer bounds for both element types placed after the mascon quantity:

<modelID>= SH3_10.12.15_IM1028_00-70r0.02

This scheme can be used to describe any packing arrangement built using the three structures in Table 3.1. With few exceptions, each identifier uniquely specifies a particular gravity model, and vice versa. This one-to-one relationship is violated when two similar models differ only in the positions of any constituent spherical harmonics elements. However, in this work all automatically placed spherical harmonics elements are initialized in the same positions when their layers of residence have the same upper and lower bounds. Hence, such models must differ in other ways to be considered distinct, and the exception to the unique identifier-model relationship is avoided.

Appendix D

Simulated Heterogeneous Truth Mascon Model

This appendix contains a brief description of the simulated truth mascon model used in the fifth section of Chapter 5. The model is divided into two layers, bounded by 45% and 95% FLPD-scaled [81] shape models. Each layer is assigned a regional density with an inner-to-outer layer ratio of 1 to 0.8. The total model mass is equal to the body mass as reported by Godard, et al.[22]; that work also provides the Rosetta OD gravity solution used in the current work. To simulate a reasonable uncertainty profile for the measurements, coefficient standard deviations are drawn from a scaled best fit exponential function of harmonic degree. The fit was performed on the root-mean-square degree uncertainties of the Rosetta OD gravity field, and have the following form:

$$\begin{aligned} \sigma_n &= ae^{bn} \\ a &= 0.0001209 \\ b &= 1.392 \end{aligned} \tag{D.1}$$

and n is the harmonic degree and σ_n is the standard deviation for the nth degree coefficients.

An additional degree-dependent scaling is performed to obtain the final uncertainties. Generally, the Stokes coefficients for a particular mass distribution diminish as the reference radius increases (see Eq. 5.4). The Rosetta OD coefficients were estimated at a reference radius of 1 km; they and their corresponding uncertainties would therefore be expected to have larger magnitudes than the reference coefficients used in this demonstration. To maintain the magnitude of uncertainty relative to the coefficient magnitude for the current application, σ_n is scaled as follows:

$$\sigma_n' = \sigma_n \sqrt{\sum_{m=1}^{n} \big(\frac{C_{nm,\mathrm{MC}}}{C_{nm,\mathrm{OD}}}\big)^2 + \big(\frac{S_{nm,\mathrm{MC}}}{S_{nm,\mathrm{OD}}}\big)^2}, \tag{D.2}$$

where $C_{nm,\mathrm{MC}}$ and $S_{nm,\mathrm{MC}}$ are the Stokes coefficients of the reference mascon model, and $C_{nm,\mathrm{OD}}$ and $S_{nm,\mathrm{OD}}$ are the coefficients of the Rosetta OD field. Each coefficient of degree n is assigned a standard deviation of σ_n', and the corresponding variances are placed in the diagonal of $\mathbf{P}_c$.

Appendix E

List of Publications and Proceedings

E.1 Refereed Journal Publication

Patrick. T. Wittick and Ryan. P. Russell, "Mixed-Model Gravity Representations for Small Celestial Bodies Using Mascons and Spherical Harmonics," *Celestial Mechanics and Dynamical Astronomy*, 131 (7):1-29, 2019.	Chapter 3

E.2 Conference Proceedings

Patrick. T. Wittick and Ryan P. Russell, "Mascon Models for Small Body Gravity Fields," *AAS/AIAA Astrodynamics Specialist Conference*, Stevenson, WA, 2017.	Chapter 3
Patrick. T. Wittick and Ryan P. Russell, "Hybrid Gravity Models for Kleopatra, Itokawa, and Comet 67P/C-G," *AAS/AIAA Astrodynamics Specialist Conference*, Snowbird, UT, 2018.	Chapter 4
Patrick. T. Wittick, Ryan P. Russell, Kenneth Getzandanner, and Erwan Mazarico, "Mascon Models for Estimating Heterogeneous Small Body Density Distributions," *AAS/AIAA Astrodynamics Specialist Conference*, South Lake Tahoe, CA, 2020.	Chapter 5

References

[1] S. Abe, T. Mukai, N. Hirata, O. S. Barnouin-Jha, A. F. Cheng, H. Demura, R. W. Gaskell, T. Hashimoto, K. Hiraoka, T. Honda, T. Kubota, M. Matsuoka, T. Mizuno, R. Nakamura, D. J. Scheeres, and M. Yoshikawa. Mass and local topography measurements of itokawa by hayabusa. *Science*, 312(5778):1344–1347, 2006.

[2] N. Arora and R. P. Russell. Efficient interpolation of high-fidelity geopotentials. *Journal of Guidance, Control, and Dynamics*, 39(1):128–143, 2016.

[3] G. Balmino. Gravitational potential harmonics from the shape of an homogeneous body. *Celestial Mechanics and Dynamical Astronomy*, 60(3):331–364, 1994.

[4] Buddhadeb Banerjee and S. P Das Gupta. Gravitational attraction of a rectangular parallelepiped. *Geophysics*, 42(5):1053–1055, 1977.

[5] C. T Barnett. Theoretical modeling of the magnetic and gravitational fields of an arbitrarily shaped threedimensional body. *Geophysics*, 41(6):1353–1364, 1976.

[6] O. Baur. Tailored least-squares solvers implementation for high-

performance gravity field research. *Computers & Geosciences*, 35(3):548–556, 2009.

[7] Benjamin Bercovici and Jay W McMahon. Inertia parameter statistics of an uncertain small body shape. *Icarus*, 328:32–44, 2019.

[8] Benjamin Bercovici, Paolo Panicucci, and Jay McMahon. Analytical shape uncertainties in the polyhedron gravity model. *Celestial mechanics and dynamical astronomy*, 132(5), 2020.

[9] R. Bijani, C. F. Ponte-Neto, D. U. Carlos, and F. J. S. Silva Dias. Three-dimensional gravity inversion using graph theory to delineate the skeleton of homogeneous sources. *Geophysics*, 80(2):G53–G66, 2015.

[10] A. G. Camacho, F. G. Montesinos, and R. Vieira. A 3-d gravity inversion tool based on exploration of model possibilities. *Computers & Geosciences*, 28(2):191–204, 2002.

[11] B. Carcich. Msi optical shape models of 433 eros, 2002.

[12] S. Casotto and R. Casotto. Cartesian development of the gravitational potential within the hotine sphere. In *Advances in the Astronautical Sciences*. AAS, 2016.

[13] D. A. Cicci. Improving gravity field determination in ill-conditioned inverse problems. *Computers & Geosciences*, 18(5):509–516, 1992.

[14] A. Colombi, A. N. Hirani, and B. F. Villac. Adaptive gravitational force representation for fast trajectory propagation near small bodies. *Journal of Guidance, Control, and Dynamics*, 31(4):1041–1051, 2008.

[15] P. Descamps, F. Marchis, J. Berthier, J.P. Emery, G. Duchne, I. de Pater, M.H. Wong, L. Lim, H.B. Hammel, F. Vachier, P. Wiggins, J.-P. Teng-Chuen-Yu, A. Peyrot, J. Pollock, R. Assafin, M.and Vieira-Martins, J.I.B. Camargo, F. Braga-Ribas, and B. Macomber. Triplicity and physical characteristics of asteroid (216) kleopatra. *Icarus*, 211(2):1022–1033, 2011.

[16] Remi C Engels and John L Junkins. Local representation of the geopotential by weighted orthonormal polynomials. *Journal of guidance and control*, 3(1):55–61, 1980.

[17] A. Fujiwara, J. Kawaguchi, D. K. Yeomans, M. Abe, T. Mukai, T. Okada, J. Saito, H. Yano, M. Yoshikawa, D. J. Scheeres, O. Barnouin-Jha, A. F. Cheng, H. Demura, R. W. Gaskell, N. Hirata, H. Ikeda, T. Kominato, H. Miyamoto, A. M. Nakamura, R. Nakamura, S. Sasaki, and K. Uesugi. The rubble-pile asteroid itokawa as observed by hayabusa. *Science*, 312(5778):1330–1334, 2006.

[18] J. Gal-Edd and A. Cheuvrant. The osiris-rex asteroid sample return: Mission operations design. In *SpaceOps 2014 Conference*, Washington, DC, 2014. AIAA.

[19] L. A. Gallardo, M. A. Pérez-Flores, and E. Gómez-Treviño. Refinement of three-dimensional multilayer models of basins and crustal environments by inversion of gravity and magnetic data. *Tectonophysics*, 397(1):37–54, 2005.

[20] R. Gaskell, J. Saito, M. Ishiguro, T. Kubota, T. Hashimoto, M Hirata, S. Abe, O. Barnouin-Jha, and D. Scheeres. Gaskell itokawa shape model v1.0. hay-a-amica-5-itokawashape-v1.0., 2008.

[21] P. J. S. Gil and J. Schwartz. Simulations of quasi-satellite orbits around phobos. *Journal of Guidance, Control, and Dynamics*, 33(3), 2010.

[22] B. Godard, F. Budnik, G. Bellei, P. Muñoz, and T. Morley. Multi-arc orbit determination to determine rosetta trajectory and 67p physical parameters. In *26th International Symposium on Space Flight Dynamics*. ISSFD, 2017.

[23] E. Herrera-Sucarrat, P. L. Palmer, and R. M. Roberts. Modeling the gravitational potential of a nonspherical asteroid. *Journal of Guidance, Control, and Dynamics*, 37(3):790–798, 2013.

[24] S. Hesar, D. Scheeres, Y. Takahashi, J. McMahon, and A. French. An improved method for characterizing small body density distribution. In *27th AIAA/AAS Spaceflight Mechanics Meeting*. AAS, 2017.

[25] Brandon A Jones, Gregory Beylkin, George H Born, and Robert S

Provence. A multiresolution model for small-body gravity estimation. *Celestial Mechanics and Dynamical Astronomy*, 111(3):309–335, 2011.

[26] Brandon A Jones, George H Born, and Gregory Beylkin. Comparisons of the cubed-sphere gravity model with the spherical harmonics. *Journal of Guidance, Control, and Dynamics*, 33(2):415–425, 2010.

[27] L. Jorda, R. Gaskell, C. Capanna, S. Hviid, P. Lamy, J. urech, G. Faury, O. Groussin, P. Gutirrez, C. Jackman, S.J. Keihm, H.U. Keller, J. Knollenberg, E. Khrt, S. Marchi, S. Mottola, E. Palmer, F.P. Schloerb, H. Sierks, J.-B. Vincent, M.F. AHearn, C. Barbieri, R. Rodrigo, D. Koschny, H. Rickman, M.A. Barucci, J.L. Bertaux, I. Bertini, G. Cremonese, V. Da Deppo, B. Davidsson, S. Debei, M. De Cecco, S. Fornasier, M. Fulle, C. Gttler, W.-H. Ip, J.R. Kramm, M. Kppers, L.M. Lara, M. Lazzarin, J.J. Lopez Moreno, F. Marzari, G. Naletto, N. Oklay, N. Thomas, C. Tubiana, and K.-P. Wenzel. The global shape, density and rotation of comet 67p/churyumov-gerasimenko from preperihelion rosetta/osiris observations. *Icarus*, 277(2):257–278, 2016.

[28] J. L. Junkins. Investigation of finite-element models of the geopotential. *AIAA Journal*, 14(6):803–808, 1976.

[29] E. Jurado, T. Martin, E. Canalias, A. Blazquez, R. Garmier, T. Ceolin, P. Gaudon, C. Delmas, J. Biele, S. Ulamec, E. Remetean, A. Torres, J. Laurent-Varin, B. Dolives, A. Herique, Y. Rogez, W. Kofman, L. Jorda, V. Zakharov, J-F. Crifo, A. Rodionov, P. Heinish, and J-B. Vincent.

Rosetta lander philae: Flight dynamics analyses for landing site selection and post-landing operations. *Acta Astronautica*, 125:65–79, 2016.

[30] W. Kaula. *Theory of Satellite Geodesy: Applications of Satellites to Geodesy.* Blaisdell Publishing Company, Waltham, Massachusetts, 1966.

[31] K. R. Koch and F. Morrison. A simple layer model of the geopotential from a combination of satellite and gravity data. *Journal of Geophysical Research*, 75(8):1483–1492, 1970.

[32] K. R. Koch and B. U. Witte. Earth's gravity field represented by a simple layer potential from doppler tracking of satellites. *Journal of Geophysical Research*, 76(35):8471–8479, 1971.

[33] Alexander S. Konopliv, James K. Miller, William M. Owen, Donald K. Yeomans, Jon D. Giorgini, Romain Garmier, and Jean-Pierre Barriot. A global solution for the gravity field, rotation, landmarks, and ephemeris of eros. *Icarus*, 160(2):289 – 299, 2002.

[34] Wong. L, G. Buechler, W. Downs, W. Sjogren, P. Muller, and P. Gottlieb. A surface-layer representation of the lunar gravitational field. *Journal of Geophysical Research*, 76(26):6220–6236, 1971.

[35] D. Lantukh, R. P. Russell, and S. Broschart. Heliotropic orbits at oblate asteroids: balancing solar radiation pressure and j_2 perturbations. *Celestial Mechanics and Dynamical Astronomy*, 121:171–190, 2015.

[36] P. J. Llanos, J. D. Jordán, G. R. Hintz, and M. Sanjurjo-Rivo. Trajectory analysis between quasi-periodic orbits and the lagrangian points around phobos. In *AAS/AIAA Astrodynamics Specialist Conference*. AAS, 2014.

[37] J. B. Lundberg and B. E. Schutz. Recursion formulas of legendre functions for use with nonsingular geopotential models. *Journal of Guidance, Control and Dynamics*, 11(1):31–37, 1988.

[38] J. W. McMahon. Improved gravity model performance by using mixed fidelity shape models for irregularly shaped small bodies. In *AAS/AIAA Astrodynamics Specialist Conference*. AAS, 2017.

[39] H. J. Melosh. Mascons and the moon's orientation. *Earth and Planetary Science Letters*, 25(3):322–326, 1975.

[40] J. K. Miller, A. S. Konopliv, P. G. Antreasian, J. J. Bordi, S. Chesley, C. E. Helfrich, W. M. Owen, T. C. Wang, B. G. Williams, and D. K. Yeomans. Determination of shape, gravity, and rotational state of asteroid 433 eros. *Icarus*, 155:3–17, 2002.

[41] F. Morrison. Algorithms for computing the geopotential using a simple density layer. *Journal of Geophysical Research*, 81(26):4933–4936, 1976.

[42] T S Moura, O C Winter, A Amarante, R Sfair, G Borderes-Motta, and G Valvano. Dynamical environment and surface characteristics of asteroid (16) Psyche. *Monthly Notices of the Royal Astronomical Society*, 491(3):3120–3136, 11 2019.

[43] Dezs Nagy. The gravitational attraction of a right rectangular prism. *Geophysics*, 31(2):362–371, 1966.

[44] K. Nakamura-Messenger, S. W. Squyres, L. F. Pace, S. Messenger, D. F. Mitchell, D. S. Lauretta, D. P. Glavin, M. Houghton, A. G. Hayes, T. Nakamura, and et al. The caesar new frontiers comet sample return mission. *Microscopy and Microanalysis*, 24(S1):21042105, 2018.

[45] M Okabe. Analytical expressions for gravity anomalies due to homogeneous polyhedral bodies and translations into magnetic anomalies. *Geophysics*, 44(4):730–741, 1979.

[46] J. Palguta, J. D. Anderson, G. Schubert, and W. B. Moore. Mass anomalies on ganymede. *Icarus*, 180(2):428–441, 2006.

[47] Paolo Panicucci, Benjamin Bercovici, Emmanuel Zenou, Jay McMahon, Michel Delpech, Jrmy Lebreton, and Keyvan Kanani. Uncertainties in the gravity spherical harmonics coefficients arising from a stochastic polyhedral shape. *Celestial mechanics and dynamical astronomy*, 132(4), 2020.

[48] V. Pareto. *Manual of Political Economy.* A. M. Kelley, 1971. English translation of original 1906 Italian text.

[49] R. S. Park, R. A. Werner, and S. Bhaskaran. Estimating small-body gravity field from shape model and navigation data. *Journal of Guidance, Control, and Dynamics*, 33(1):212–221, 2010.

[50] J. M. Pearl and D. L. Hitt. Asteroid gravitational models using mascons derived from polyhedral sources. In *AIAA/AAS Astrodynamics Specialist Conference*, Washington, DC, 2016. AIAA.

[51] J. M. Pearl and D. L. Hitt. Asteroid gravitational models using surface concentrations. In *27th AIAA/AAS Spaceflight Mechanics Meeting*. AAS, 2017.

[52] J. M. Pearl and D. L. Hitt. Comparing the computational efficiency of polyhedral and mascon gravity models. In *27th AIAA/AAS Spaceflight Mechanics Meeting*. AAS, 2017.

[53] Jason M Pearl and Darren L Hitt. A fast quadrature-based gravity model for the homogeneous polyhedron. *Monthly notices of the Royal Astronomical Society*, 492(1):420–430, 2020.

[54] S. Pines. Uniform representation of the gravitational potential and its derivatives. *AIAA Journal*, 11(11):1508–1511, 1973.

[55] V POHNKA. Optimum expression for computation of the gravity field of a homogeneous polyhedral body1. *Geophysical Prospecting*, 36(7):733–751, 1988.

[56] H. N. Pollack. Spherical harmonic representation of the gravitational potential of a point mass, a spherical cap, and a spherical rectangle. *Journal of Geophysical Research*, 78(11):1760–1768, 1973.

[57] G. Romain and B. Jean-Pierre. Ellipsoidal harmonic expansions of the gravitational potential: Theory and application. *Celestial Mechanics and Dynamical Astronomy*, 79(4):235–275, 2001.

[58] R. P. Russell and N. Arora. Global point mascon models for simple, accurate, and parallel geopotential computation. *Journal of Guidance, Control, and Dynamics*, 35(5):1568–1581, 2012.

[59] D. F. Santos, J. B. C. Silva, C. M. Martins, R. dC. S. dos Santos, L. C. Ramos, and A. C. M. de Araújo. Efficient gravity inversion of discontinuous basement relief. *Geophysics*, 80(4):G95–G106, 2015.

[60] H. Save, S. Bettadpur, and B. D. Tapley. High-resolution csr grace rl05 mascons. *Journal of Geophysical Research: Solid Earth*, 121(10):7547–7569, 2016.

[61] D. J. Scheeres. *Orbital Motion in Strongly Perturbed Environments*. Springer-Verlag, 2012.

[62] D. J. Scheeres, B. Khushalani, and R. A. Werner. Estimating asteroid density distributions from shape and gravity information. *Planetary and Space Science*, 48(10):965–971, 2000.

[63] D. J. Scheeres, S. J. Ostro, R. S. Hudson, E. M. DeJong, and S. Suzuki. Dynamics of orbits close to asteroid 4179 toutatis. *Icarus*, 132:53–79, 1998.

[64] D. J. Scheeres, S. J. Ostro, R. S. Hudson, and R. A. Werner. Orbits close to asteroid 4769 castalia. *Icarus*, 121:67–87, 1998.

[65] M. K. Shepard, B. Timerson, D. J. Scheeres, L. A. M. Benner, J. D. Giorgini, E. S. Howell, C. Magri, M. C. Nolan, A. Springmann, P. A. Taylor, and A. Virkki. A revised shape model of asteroid (216) kleopatra. *Icarus*, 311:197–209, 2018.

[66] D. A Smith. The gravitational attraction of any polygonally shaped vertical prism with inclined top and bottom faces. *Journal of Geodesy*, 74(5):414–420, 2000.

[67] S. T. Sutton, H. N. Pollack, and M. J. Jackson. Spherical harmonic representation of the gravitational potential of discrete spherical mass elements. *Geophysical Journal International*, 107:77–82, 1991.

[68] Y. Takahashi and D. J. Scheeres. Surface gravity fields for asteroids and comets. *Journal of Guidance, Control, and Dynamics*, 36(2):362–374, 2013.

[69] Y. Takahashi and D. J. Scheeres. Morphology driven density distribution estimation for small bodies. *Icarus*, 233:179–193, 2014.

[70] Y. Takahashi and D. J. Scheeres. Small body surface gravity fields via spherical harmonic expansions. *Celestial Mechanics and Dynamical Astronomy*, 119(2):169–206, 2014.

[71] B. J. Tapley, B. E. Schutz, and G. H. Born. *Statistical Orbit Determination*. Elsevier Academic Press, 2004.

[72] S. Tardivel. The limits of the mascons approximation of the homogeneous polyhedron. In *AIAA/AAS Astrodynamics Specialist Conference*, Washington, DC, 2016. AIAA.

[73] Rosetta Flight Dynamics Team. Comet 67p/c-g shape models, esa image archives. online, 2015.

[74] J. J. Thomson. On the structure of the atom: an investigation of the stability and periods of oscillation of a number of corpuscles arranged at equal intervals around the circumference of a circle; with application of the results to the theory of atomic structure. *The London, Edinburgh, and Dublin Philosophical Magazine and Journal of Science*, 7(39):237–265, 1904.

[75] D. A. Vallado and W. D. McClain. *Fundamentals of Astrodynamics and Applications*. Microcosm Press, 2013.

[76] Jrg Waldvogel. The newtonian potential of homogeneous polyhedra. *Zeitschrift fr angewandte Mathematik und Physik*, 30(2):388–398, 1979.

[77] D. N. Weise, F. W. Landerer, and M. M. Watkins. Quantifying and reducing leakage errors in the jpl rl05m grace mascon solution. *Water Resources Research*, 52(9):7490–7502, 2016.

[78] R. A. Werner. Spherical harmonic coefficients for the potential of a constant-density polyhedron. *Computers & Geosciences*, 23(10):1071–1077, 1997.

[79] R. A. Werner and D. J. Scheeres. Exterior gravitation of a polyhedron derived and compared with harmonic and mascon gravitation representations of asteroid 4769 castalia. *Celestial Mechanics and Dynamical Astronomy*, 65(3):313–344, 1997.

[80] Robert A Werner. The gravitational potential of a homogeneous polyhedron or don't cut corners. *Celestial mechanics and dynamical astronomy*, 59(3):253–278, 1994.

[81] P. T. Wittick and R. P. Russell. Hybrid gravity models for kleopatra, itokawa, and comet 67p/c-g. In *AAS/AIAA Astrodynamics Specialist Conference*. AAS, 2018.

[82] D. K. Yeomans, P. G. Antreasian, J.-P. Barriot, S. R. Chesley, D. W. Dunham, R. W. Farquhar, J. D. Giorgini, C. E. Helfrich, A. S. Konopliv, J. V. McAdams, J. K. Miller, W. M. Owen Jr., D. J. Scheeres, P. C. Thomas, J. Veverka, and B. G. Williams. Radio science results during the near-shoemaker spacecraft rendezvous with eros. *Science*, 289:2085–2088, 2000.

[83] M. T. Zuber, D. E. Smith, A. F. Cheng, J. B. Garvin, O. Aharonson, T. D. Cole, P. J. Dunn, Y. Guo, F. G. Lemoine, G. A. Neumann, D. D.

Rowlands, and M. H. Torrence. The shape of 433 eros from the near-shoemaker laser rangefinder. *Science*, 289:2097–2101, 2000.

Index

Vita

Patrick Thomas Wittick was born in Hackettstown, New Jersey in 1993. After moving from New Jersey to Atlanta, Georgia to near Philadelphia, Pennsylvania, he attended Pennsylvania State University from 2011 to 2015 and received a Bachelor of Science degree with honors in Aerospace Engineering. After applying to various graduate programs and potential employers, he chose to pursue his PhD in Aerospace Engineering at the University of Texas at Austin beginning in the fall of 2015.

Permanent address: patrickwittick2@gmail.com

This dissertation was typeset with LaTeX[†] by the author.

[†] LaTeX is a document preparation system developed by Leslie Lamport as a special version of Donald Knuth's TeX Program.